REPORT DOCUMENTATION PAGE

Form Approved OMB NO. 0704-0188

1. REPORT DATE (DD-MM-YYYY)	2. REPORT TYPE	3. DATES COVERED (From - To)
22-07-2013	Final Report	1-Oct-2008 - 30-Sep-2012

4. TITLE AND SUBTITLE
A Technique for Evaluating the Uncertainties in Path Loss Predictions Caused by Sparsely Sampled Terrain Data

5a. CONTRACT NUMBER
W911NF-08-1-0485

5b. GRANT NUMBER

5c. PROGRAM ELEMENT NUMBER
611102

6. AUTHORS
Daniel E. Davis & Gary S. Brown

5d. PROJECT NUMBER

5e. TASK NUMBER

5f. WORK UNIT NUMBER

7. PERFORMING ORGANIZATION NAMES AND ADDRESSES
Virginia Polytechnic Institute & State University
Office of Sponsored Programs
1880 Pratt Drive, Suite 2006
Blacksburg, VA   24060   -3580

8. PERFORMING ORGANIZATION REPORT NUMBER

9. SPONSORING/MONITORING AGENCY NAME(S) AND ADDRESS(ES)
U.S. Army Research Office
P.O. Box 12211
Research Triangle Park, NC 27709-2211

10. SPONSOR/MONITOR'S ACRONYM(S)
ARO

11. SPONSOR/MONITOR'S REPORT NUMBER(S)
54624-EL.1

12. DISTRIBUTION AVAILIBILITY STATEMENT
Approved for Public Release; Distribution Unlimited

13. SUPPLEMENTARY NOTES
The views, opinions and/or findings contained in this report are those of the author(s) and should not contrued as an official Department of the Army position, policy or decision, unless so designated by other documentation.

14. ABSTRACT
Radio propagation models provide an estimate of the power loss in a communication link caused by the surface of the ground, atmospheric refraction, foliage, and other environmental factors. Many of the models rely on digital topographic databases to provide information about the terrain, and generally the databases are sparsely sampled relative to the electromagnetic wavelengths used for communication systems. This work primarily develops a

15. SUBJECT TERMS
Radio Propagation, Terrain Effects, Numerical Methods, Foliage Blockage, Propagation Data

16. SECURITY CLASSIFICATION OF:			17. LIMITATION OF ABSTRACT	15. NUMBER OF PAGES	19a. NAME OF RESPONSIBLE PERSON
a. REPORT	b. ABSTRACT	c. THIS PAGE			Gary Brown
UU	UU	UU	UU		19b. TELEPHONE NUMBER
					540-231-4467

Report Title

A Technique for Evaluating the Uncertainties in Path Loss
Predictions Caused by Sparsely Sampled Terrain Data

ABSTRACT

Radio propagation models provide an estimate of the power loss in a communication link caused by the surface of the ground, atmospheric refraction, foliage, and other environmental factors. Many of the models rely on digital topographic databases to provide information about the terrain, and generally the databases are sparsely sampled relative to the electromagnetic
wavelengths used for communication systems. This work primarily develops a
technique to evaluate the effects of that sparsity on the uncertainty of propagation models. That is accomplished by accurately solving the electromagnetic fields over many randomly rough surfaces which pass through the sparse topographic data points, many possible communication links, all of which fit the underlying data, are represented. The power variation caused by the different surface realizations is that due to the sparse sampling. Additionally,
to verify that this solution technique is a good model, experimental propagation measurements were taken, and compared to the computations.

Enter List of papers submitted or published that acknowledge ARO support from the start of the project to the date of this printing. List the papers, including journal references, in the following categories:

(a) Papers published in peer-reviewed journals (N/A for none)

<u>Received</u>   <u>Paper</u>

TOTAL:

Number of Papers published in peer-reviewed journals:

(b) Papers published in non-peer-reviewed journals (N/A for none)

<u>Received</u>   <u>Paper</u>

TOTAL:

Number of Papers published in non peer-reviewed journals:

(c) Presentations

Davis, D. E. & Brown, G. S. "Variation in propagation loss predictions due to terrain data uncertainty" USNC--URSI National Radio Science Meeting, University of Colorado at Boulder, 2008

Davis, D. E.; Westin, B. A. & Brown, G. S. "An accurate and
computationally fast approximation for combined field integral equation Green's functions" USNC--URSI National Radio Science Meeting, University of Colorado at Boulder, 2010

Davis, D. E.; Westin, B. A. & Brown, G. S. "Effects of accurate Green's function approximations on integral equation convergence for randomly rough dielectric surfaces" IEEE International Symposium on Antennas and Propagation and USNC--URSI National Radio Science Meeting, Toronto, 2010

Davis, D. E.; Westin, B. A. & Brown, G. S. "Simplification of the
combined field integral equations for propagation prediction" USNC--URSI National Radio Science Meeting, University of Colorado at Boulder, 2011

Davis, D. E.; Westin, B. A. & Brown, G. S. "Considerations with numeric stability when optimizing MOMI for long range propagation computations" USNC--URSI National Radio Science Meeting, University of Colorado at Boulder, 2012

Davis, D. E. & Brown, G. S. "UTD analysis of foliage penetration for use in propagation modeling" USNC--URSI National Radio Science Meeting, University of Colorado at Boulder, 2013

Davis, D. E.; Westin, B. A. & Brown, G. S. "Applying MOMI to a
dielectric foliage layer above ground for propagation prediction"
USNC--URSI National Radio Science Meeting, University of Colorado at
Boulder, 2013

Number of Presentations: 7.00

Non Peer-Reviewed Conference Proceeding publications (other than abstracts):

Received   Paper

TOTAL:

Number of Non Peer-Reviewed Conference Proceeding publications (other than abstracts):

Peer-Reviewed Conference Proceeding publications (other than abstracts):

Received   Paper

TOTAL:

Number of Peer-Reviewed Conference Proceeding publications (other than abstracts):

(d) Manuscripts

Received   Paper

TOTAL:

Number of Manuscripts:

Books

Received   Paper

TOTAL:

Patents Submitted

Patents Awarded

Awards

Graduate Students

NAME	PERCENT_SUPPORTED	Discipline
Daniel E. Davis	0.50	
Benjamin A. Westin	0.10	
FTE Equivalent:	**0.60**	
Total Number:	**2**	

Names of Post Doctorates

NAME	PERCENT_SUPPORTED
FTE Equivalent:	
Total Number:	

Names of Faculty Supported

NAME	PERCENT_SUPPORTED	National Academy Member
Gary S. Brown	0.05	
FTE Equivalent:	**0.05**	
Total Number:	**1**	

Names of Under Graduate students supported

NAME	PERCENT_SUPPORTED
FTE Equivalent:	
Total Number:	

Student Metrics
This section only applies to graduating undergraduates supported by this agreement in this reporting period

The number of undergraduates funded by this agreement who graduated during this period: 0.00

The number of undergraduates funded by this agreement who graduated during this period with a degree in science, mathematics, engineering, or technology fields: 0.00

The number of undergraduates funded by your agreement who graduated during this period and will continue to pursue a graduate or Ph.D. degree in science, mathematics, engineering, or technology fields: 0.00

Number of graduating undergraduates who achieved a 3.5 GPA to 4.0 (4.0 max scale): 0.00

Number of graduating undergraduates funded by a DoD funded Center of Excellence grant for Education, Research and Engineering: 0.00

The number of undergraduates funded by your agreement who graduated during this period and intend to work for the Department of Defense 0.00

The number of undergraduates funded by your agreement who graduated during this period and will receive scholarships or fellowships for further studies in science, mathematics, engineering or technology fields: 0.00

Names of Personnel receiving masters degrees

NAME
Daniel E. Davis
Total Number: **1**

Names of personnel receiving PHDs

NAME
Benjamin A. Westin
Total Number: **1**

Names of other research staff

NAME	PERCENT_SUPPORTED
FTE Equivalent:	
Total Number:	

Sub Contractors (DD882)

Inventions (DD882)

Scientific Progress

A new numerical method has been applied to the problem of rigorously accounting for the terrain surface on the propagation of point-to-point communications signals. This method has been tested against data in the 900 to 2.3 GHz frequency range acquired in the National Radio Quiet Zone at National Radio Astronomy Observatory and found to provide reasonably good results. The two major shortcomings of the model are its two-dimensional nature and the lack of foliage inclusion. Both experimental and analytical work was expended on developing a correction for the effects of foliage with reasonably good results. Clearly, the numerical model should perform best in a bare terrain environment. The effect of sparse terrain elevation sampling was found to be very important within 0.5 km of the transmitter and diminished as the receiver moves beyond 1 km.

Technology Transfer

A Technique for Evaluating the Uncertainties in Path Loss Predictions Caused by Sparsely Sampled Terrain Data

Daniel E. Davis

Thesis submitted to the Faculty of the

Virginia Polytechnic Institute and State University

in partial fulfillment of the requirements for the degree of

Master of Science

in

Electrical and Computer Engineering

Gary S. Brown, Chair

William A. Davis

William J. Floyd

June 26, 2013

Blacksburg, Virginia

Keywords: Method of Ordered Multiple Interactions, Rough Surface Scattering,

Propagation Loss, Radio Propagation

A Technique for Evaluating the Uncertainties in Path Loss Predictions Caused by Sparsely Sampled Terrain Data

Daniel E. Davis

(ABSTRACT)

Radio propagation models provide an estimate of the power loss in a communication link caused by the surface of the ground, atmospheric refraction, foliage, and other environmental factors. Many of the models rely on digital topographic databases to provide information about the terrain, and generally the databases are sparsely sampled relative to the electromagnetic wavelengths used for communication systems. This work primarily develops a technique to evaluate the effects of that sparsity on the uncertainty of propagation models.

That is accomplished by accurately solving the electromagnetic fields over many randomly rough surfaces which pass through the sparse topographic data points, many possible communication links, all of which fit the underlying data, are represented. The power variation caused by the different surface realizations is that due to the sparse sampling. Additionally, to verify that this solution technique is a good model, experimental propagation measurements were taken, and compared to the computations.

Acknowledgments

First and foremost, thanks to my wife Suzanne. She has put up with the delays and the trips out to Green Bank. My thanks also go to Dr. Brown for his support and help over the last few years. And many thanks to Thad Black for his aid in learning MOMI, and Ben Westin for his help in programming and working through the math. Finally, for the others in EMIL, Bob Stockland and Kevin Diomedi, thank you for providing support in getting through the writing. To my parents and Suzanne's, thank you for tolerating the time we've spent here and the missed holidays that we've worked through.

The experimental work presented in Chapter 7 required the help of many individuals from VT, NSWC, and NRAO. In addition to Ben and Dr. Brown, Wes Sizemore at NRAO, and Bruce Naley, Punk Chilton and Natasha Lagoudous from NSWC all put in lots of work during the weeks conducting the experiment. Bruce was invaluable for climbing 100 feet up the water tower, with the antenna and spectrum analyzer, to take measurements. Additionally, equipment was provided by NSWC, and many at NRAO provided help in experiment planning, regulatory approval, and scrounging for parts, and fixing broken equipment.

Contents

List of Figures

List of Tables

Chapter 1

Introduction

In the process of planning wireless communication systems, it is important to be able to predict the loss in the communications link that is due to the path of the wireless transmission [1]. For terrestrial links, this path loss includes both the effects of the spreading of the wave-front, as well as effects dependent on the terrain over which the radio waves propagate [2]. Models for the path loss in the presence of the terrain have been developed over many years. One way of categorizing these models is to break them into area prediction and point-to-point methods [2]. Area prediction models usually utilize general terrain characteristics to estimate the probability of a level of loss at any point a fixed distance from the transmitter. Point-to-point models utilize more specific terrain data to predict the actual loss present in link from a fixed transmitter location to a fixed receiver location.

Any model which attempts to incorporate the effects of the specific environment of the

link must be based upon terrain data. Terrain data is available as raster data, which is sampled data in a grid. In the United States, the US Geological Survey (USGS) makes available the National Elevation Dataset (NED) [3]. The NED covers the entire United States in what is descibed as the "best available" elevation data, and has a resolution of one arc-second, which is approximately thirty meter spacing [3]. Additional NED data is also available in some areas at a resolution of one-third arc-second (about ten meters) and in even fewer areas for one-ninth arc-second (about three meters) resolution.

Rough-surface scattering theory has shown that elements down to and even below the order of an wavelength can have significant effects on the scattered electromagnetic field [4,5]. The wavelength of an electromagnetic wave is given by the relationship

$$c = \lambda f \tag{1.1}$$

where c is the speed of light, approximately $2.998 \times 10^8 \frac{m}{s}$ in air [6], f is the frequency, and λ is the wavelength [7]. Thus, for frequencies above 300 MHz, the wavelength is less than one meter, and above 1.0 GHz, it is less than thirty centimeters. Clearly, these wavelengths are significantly smaller than even the three meter resolution of the best terrain data, and much smaller than the thirty meter resolution available for the USA. Thus, exact computation of terrain loss from currently available terrain data is not theoretically possible.

Excluding the inexactness of the data, other simplifications may be made by limiting the type and number of terrain features modeled. Aspects such as size, shape, and material properties of the features considered, and the extent of the terrain beyond the direct propa-

gation path that is considered are common factors affecting the complexity of a propagation model [2]. As already mentioned, the terrain data that is employed in such predictions is sampled with a spacing of tens or hundreds of electromagnetic wavelengths. Certainly, having to sample the terrain on a centimeter scale to predict propagation over many kilometers for high frequency applications is unreasonable. Conversely, simplification by undersampling, while reasonable, introduces an unknown level of uncertainty into the predictions. It is the goal of this thesis to provide a means for testing the validity of these assumptions and to show their effects in several test cases.

The following proceedure is the proposed method for accomplishing this evaluation of undersampling. Begin assuming that the topographic data is know at fixed points along the transmission path, such as the data in a database such as the NED. Because the connection of the data points is unknown, the points are connected with random curves based on estimated surface statistics. This process is repeated to create a large number of possible surface realizations. Then, assuming that the surface is a perfect electrical conductor (PEC), the scattering from each surface realization is computed by solving for the currents that represent the total tangential fields along the surface. The currents are obtained by numerically solving the magnetic field integral equation (MFIE) [8].

The MFIE is solved with the Method of Ordered Multiple Interactions (MOMI). MOMI, developed by Kapp and Brown [9], allows for the solution of the discretized MFIE even when the surface becomes very large by avoiding matrix inversion and the storage of the kernel of the integral equation. In cases of scattering from surfaces on the order of tens of

thousands to hundreds of thousands of wavelengths long, these memory storage reductions are highly important. MOMI does this by separating the propagator matrix into upper and lower triangular matrices, and a diagonal matrix, and reformulating the MFIE into a new integral equation. This MOMI integral equation, when solved by Neumann iteration, requires inversion of the triangular matrices, but this is accomplished via forward or backward substitution, and thus avoids the costly storage of the entire matrix [9]. This approach is equivalent to preconditioning the MFIE.

Once the tangential fields along the surface are known, they can be used to compute the fields present in the rest of the region. Since all other properties are held constant during this process, the differences in the fields between realizations are solely the result of the uncertainty in the terrain profile. Thus, it is possible to evaluate how the sparsity of the terrain data affects the propagation prediction. At a basic level, statistical properties of the results, such as the mean and standard deviation in the path loss computed through this method, can be used to identify how the uncertainty caused solely by that sparsity.

While MOMI is a good technique for the solution of scattering from large surfaces, some issues must be addressed prior to its application to this problem. In previous applications of MOMI, the effects of the surface truncation have been avoided by the use of a tapered beam to limit the illumination to the region near the center of the surface. For this study that option is not available since the source is essentially located at one end of the propagation path and the field points continue all the way to the other end of the path. Thus, the error due to illumination of the artificial surface edge needs to be considered. An error bound on

the effects that arise due to disregarding currents outside the illuminated surface is necessary for the computation of the scattering; such a bound is developed.

A methodology for providing random connections of the known elevation points is also developed. To produce numerous surfaces which could all produce the same sampled terrain data, a technique is developed for merging randomly rough surfaces with a spline surface. This new surface has the roughness spectrum of the random surface added to the spectrum of a spline through the data points, and continues to pass through the original data. Thus, each surface which is created is a random but smooth connection of the original sampled data points, and could be used to reproduce the original terrain data.

Additionally, after the initial application of MOMI to the propagation problem, the results were not found to be satisfactory. Two changes to the technique have been developed for use in propagation prediction. The first is necessary to aid in the conversion between the two dimensional problem that MOMI solves and the three dimensional reality of propagation. This is accomplished by changing the way the scattered fields are computed from the two dimensional surface currents to account for the power loss in the third dimension. The second change is the inclusion of antenna patterns so that the MOMI computations more closely mirror real transmission cases.

Finally, the results produced by MOMI need to be verified against measured data to ensure that they are reasonably accurate. Therefore, a series of radio propagation measurements were performed in the mountains around Green Bank, West Virginia. The measurements cover four frequencies and six propagation paths, and are the basis for validating the

propagation model developed in this work.

All of this work is developed in the following chapters. Chapters 2 to 4 consist of a review of existing work. Chapters 5 to 8 consist primarily of new contributions.

Chapter 2 reviews the work that has been done to date in both propagation experimentation and prediction. Both empirical and theoretical propagation models are reviewed. Also covered is the previous work on the development of MOMI and the equivalent forward-backward method.

Chapter 3 covers the basic computations of electromagnetic theory as they relate to this work. The chapter contains derivations of the electric and magnetic fields radiated by both electric and magnetic currents. Following from that, the fields of a line source and a current sheet are both computed. These derivations form the basis for the rest of the computations that will be performed.

Chapter 4 discusses the development of the method of ordered multiple interactions. It begins with the formulation of the two dimensional magnetic field integral equation from Maxwell's equations. That is followed with a discussion of the method of moments discretization of the integral equation for both transverse magnetic and transverse electric cases. Then MOMI is derived from the discretized MOM formulation.

Chapter 5 contains the formulation of an error bound on the truncation of the Magnetic Field Integral Equation solution for a flat surface. This error bound, which is developed directly from the integral equation, will provide a reasonable assurance that the solutions

developed in later chapters do not suffer due to surface truncation.

Chapter 6 discusses the techniques used to model the terrain and compute the path loss. It describes the process for generating surfaces from sampled data points. The process involves fitting a spline to the data, and then adding in randomly rough surfaces to the spline fit. Finally, it describes the computation of path loss, a term used in the communications link equation, from the total field and source terms.

Chapter 7 covers the propagation measurements made in West Virginia. First, it details the propagation paths over which the measurements were made. Then, the experimental technique is described and the measurement results are presented.

Chapter 8 shows the results of the MOMI computations on the propagation paths used for the experimental measurements. Several results are first presented with the use of an omnidirectional source. However, the use of an omnidirectional source is found to be deficient. Following that is the development of the new 2D to 3D radiation term and the technique for including radiation patterns. Finally, computational results are compared to the experimental measurements using the changes to the technique.

Chapter 9 summarizes the results and presents the conclusions.

Chapter 2

Background and Literature Review

This work covers both radio propagation experimentation and modeling, and focusses in depth on propagation modeling with the method of ordered multiple interactions (MOMI). What follows in this chapter is a review of these subjects broken down into three sections. The first section covers the general work done in propagation experimentation. The second section covers propagation models, and is divided between empirical models and theoretical models. Finally, a section is devoted specifically to the developments of the method of moments (MOM) and MOMI.

2.1 Radio Propagation Experiments

The theory of electromagnetic waves was formulated by Maxwell in 1865 [10]. In his paper unifying the previous work on electricity and magnetism, he posited that light was an elec-

tromagnetic wave, and that electromagnetic waves could propagate through space. Maxwell presented the mathematics behind his theory and showed that the speed at which electromagnetic waves should propagate was within the measured tolerance of the speed of light. From that point to the present, many different experiments have been carried out on radio propagation. The following covers the experimental work in long distance radio propagation.

Radio waves were observed by Hertz in a series of experiments conducted from 1887 to 1890 [11]. Hertz observed that oscillatory electromagnetic fields could be created with spark gaps, and transmitted across the laboratory. During the 1890's, Marconi began developing a practical wireless telegraphy system, including demonstrated transmission of ship-to-shore communications by 1899 [12]. Several years later, transatlantic communication was demonstrated [13]. Marconi recognized that although he had working transmission systems, the actual details of the propagation were not yet understood [14]. However, Marconi generally avoided providing any specifics of the experiments that his company carried out other than whether or not communication was successful [15–17].

In 1928 and 1929, Barfield and Munro presented a pair of papers with measurements of the signal strength of a London station broadcasting at 824 KHz [18,19]. The measurements extended out on radials from London to distances between 90 km and 160 km. In the first paper, the results are compared to Sommerfeld's prediction for attenuation over a dielectric earth, with the measurements falling off more rapidly than predicted by Sommerfeld's solution. The author surmises that foliage is the cause of the difference and develops a corrective factor for the attenuation caused by foliage. The second paper addresses measurements of

the same source focussed on towns as opposed to rural areas. The authors show that measurements of the field strength are significantly lower in towns, with the hypothesis that buildings cause the additional attenuation. However, they are not able to come up with a good theoretical method for predicting the loss due to structures.

In 1932, Kirby and Norton made measurements of AM radio stations around the eastern United States and used the results to compute the dielectric properties of the earth [20]. A year later, Feldman used measurements of the direct and reflected rays in the line-of-sight region to measure the dielectric properties for transmissions up to 30 MHz [21]. At the same time, Trevor and Carter conducted experiments at 44 MHz and 61 MHz [22]. Feldman, as well as Trevor and Carter, used a combination of airborne and ground based receivers, and based predictions on optical techniques of reflection. Trevor and Carter determined that optical techniques were moderately accurate, but could sometimes be wrong by significant amounts.

Propagation experiments for 65 MHz and 200 MHz, carried out by Englund, Crawford, and Mumford, were reported in 1935 [23]. These experiments focused on beyond line-of-sight results at these frequencies. The authors found that while smooth-earth diffraction results provided a general guide to the signal levels over the horizon, significant differences could occur due to atmospheric refraction. At the same time, Burrows, Decino, and Hunt made measurements designed to verify the limits on use of line-of-sight and flat ground approximations up to 150 MHz [24]. They also compared results against predictions for diffraction around the edge of the earth. The group also noted that fading occurred throughout the day

for the over-the-horizon paths. The resulting conclusion was that common approximations used for predicting propagation at lower frequencies do not hold above approximately 100 MHz.

Carter and Wickizer examined the effects of multi-path transmission on a broad bandwidth, publishing the results in 1936 [25]. They measured the channel response for a 6 MHz bandwidth, centered at 179 MHz, for a transmission in downtown New York City. Their results showed that limited multi-path interference could cause large variations in the response across such a wide frequency band.

In 1939, Maclean and Wickizer preformed measurements over a two week period to examine fading beyond the line-of-sight [26]. Measurements were made at 49.5 MHz and 52.75 MHz, at three points along a straight line path. The measurements showed no correlation of fading with time at the locations. Wickizer followed up on these with additional mobile ground based measurements at 52.75 MHz along radials out from the transmitter [27]. He discussed the effects of terrain, structures, and overhead wires on the received power level.

McPetrie published several experiments at higher frequencies in 1940. McPetrie and Saxton evaluated 100 MHz and 150 MHz transmissions utilizing optical theory, showing good agreement when within the line-of-sight of the transmitter [28]. McPetrie and Strickland used similar experiments while approaching grazing incidence to test for the presence of the surface wave [28].

Hull conducted many measurements of propagation at 60 MHz in the 1930's, but these

results were not published until 1945, when Friend collected them after Hull's 1938 death [29]. Hull's measurements included near daily power measurements for several years time, and provided a large data set for studying atmospheric effects. Friend used these to compute the range of atmospheric refraction levels seen over several years by Hull.

Research before and during World War II made possible the higher frequency transmissions that are commonly used today [30,31]. Many studies were conducted during the period that were not publicly distributed, with most focusing on over-ocean and atmospheric effects. Studies found that at higher frequencies, obstructions and atmospheric refraction had much more effect on the propagation loss than at lower frequencies. In a summary of British wartime research, Smith-Rose cites gains in understanding of diffraction, the electrical properties of soil and ground, ionospheric reflection, refraction and ducting, and atmospheric absorption [30]. Norton cites similar work produced in the USSR, Japan, United States, and Germany, with a particular focus on ionospheric and atmospheric work [31].

In 1946, McPetrie and Ford published a pair of papers on work carried out during 1942 and 1943 evaluating the propagation of 30 MHz to 3 GHz transmissions [32, 33]. These included tests of foliage and building obstruction, as well as diffraction across the top of a smooth hill. In the same year, Mueller described rain and atmospheric attenuation measurements at 4.8 GHz [34]. Mueller emphasized that measurements at the high frequency rarely matched predictions for propagation over flat ground due to the undulations in the terrain.

Allen provides a good summary of the theoretical and empirical prediction methods available when reporting his 1947 experiments [35]. He describes the effects of the ground

wave, troposcatter, and sky wave on signals, prior to showing how measured data compares to those curves. Allen is clear that at the time, propagation mechanisms are not well understood above approximately 50 MHz. His analysis is primarily dedicated to evaluating the coverage areas and likelihood of interference of television signals at different frequency bands. Allen concludes that coverage areas are not significantly affected, but interference is reduced, in the higher end of the VHF band compared to the lower end.

Also in 1947, Wickizer and Braaten reported on long-term measurements carried out at 45 MHz, 474 MHz, and 2.8 GHz, for over-the-horizon paths [36]. Their results showed that much more variability was seen in the higher frequency power measurements than in the 45 MHz reception. They showed that beyond the horizon, signal levels were correlated to weather conditions, supporting atmospheric refraction as the cause for fading.

Finally, Katzin, Bauchman, and Binnian also reported on propagation experiments in 1947 [37]. They measured atmospheric ducting effects for 3 GHz and 10 GHz transmissions when over the ocean. In-depth analysis of wind speeds and atmospheric profiles taken during the measurements showed that the factors of wind, temperature, and humidity changes with altitude cause ducts to form. The authors noted that the ducts were more pronounced at the higher frequency.

Another set of propagation experiments was carried out in 1948 by Brown, Epstein, and Peterson [38]. In preparation for using higher frequencies for color television transmission, they measured the signal strength along two radials from New York City out to distances of 50 miles. Transmitters at 67 MHz and 288 MHz were located atop the Empire State

Building, while 510 MHz and 910 MHz transmissions were broadcast from the 87th floor. The results were compared to those predicted by assuming a smooth dielectric spherical earth with a linearly changing atmosphere. They showed that at the lower frequencies, the smooth earth approximation provided a good prediction; however at the higher 510 MHz and 910 MHz frequencies the resulting signal strengths were much lower than predicted. The resulting signal variation at higher frequencies was primarily attributed to multi-path, and they determined that the use of directional receiving antennas could provide much higher received signal levels.

Durkee reported results in 1948 on over land propagation between 700 MHz and 24 GHz [39]. Durkee measured fading over a fixed path to find season variations in the signal strength. His results showed that fading could range from just 2 dB over a day to more than 20 dB variation in a brief time. Generally, higher frequency transmissions showed greater susceptibility to the atmospheric conditions.

Saxton produced a pair of pair of papers in 1951 examining VHF propagation. The first provided a theoretical basis for higher levels of atmospheric refraction at higher frequencies [40]. The second, with Luscombe and Bazzard, reported experiments at 45 MHz and 90 MHz, to examine beyond the horizon propagation loss [41]. Kirke also reported on 90 MHz propagation experiments in 1951 [42]. Both experiments examined coverage areas at these frequencies, examining how over-the-horizon transmission was affected by topography and fading. Both also produced estimates of how transmitter height effects the propagation loss.

Young performed a series of experiments of mobile radio reception between 150 MHz

and 3.7 GHz in 1952 [43]. These early mobile phone experiments were also carried out in the vicinity of New York City, examining signal strengths at multiple frequencies and in urban, sub-urban, and rural environments communicating with a base station in New York. He presents statistical tables of measured path loss versus distance compared to the ideal smooth earth loss and determines that, due to noise and loss factors, 500 MHz is the best frequency band for a mobile phone system.

Crawford wrote about point-to-point propagation experiments performed at microwave frequencies in 1952 [44]. His experiment focused on fading in the point-to-point link, specifically evaluating how fading varied across frequencies. Using the frequency sweeps, he was able to verify that fading was indeed the result of multi-path.

In 1953, Dickson, et al., showed by theory and experiment that mountain obstructions tend to reduce fading at VHF frequencies [45]. They demonstrated that because a large mountain obstruction limits the possible transmission paths, it will reduce the fading due to multi-path. They also showed that a properly situated mountain could even reduce transmission loss compared to a smooth earth case by eliminating the interference between a refracted and smooth-earth diffracted path.

Bullington published many papers on measurements performed in the 1950's [46–50]. A paper in 1950 [46] provided comparisons of measured data in VHF and UHF bands with smooth earth and diffraction theories, with a focus on required separation distance between stations to avoid interference. In 1953, he reports on over the horizon propagation measurements made at 500 MHz and 3.7 GHz, showing that the results are well above the levels

predicted by the smooth spherical earth theory at these frequencies [47]. Similar tests made in Newfoundland by Bullington, Inkster, and Durkee were published in 1955 and 1956 [49,50]. While the empirical relationships of signal strength to distance are presented in both cases, no attempt is made to present a new theoretical model. Bullington also reports on measurements performed in developing the microwave relay system in the 1954 [48]. The experiments focused on the ground reflection coefficients at 4.0 GHz between the locations of the towers. No theoretical relationship was discerned, but a statistical relationship is presented based on the predominant shape of the terrain profile between the locations.

In 1958, Rice began an investigation into some of the specific factors affecting loss in an urban environment [51]. He examined the loss present in the signal on the ground floor of building versus that just outside the building, determining that at 35 MHz and 150 MHz, the loss due to the building was on the order of 20 dB to 25 dB, with the losses being more uniform at the higher frequency, and decreasing loss at higher points in the buildings.

In 1962, Hagg and Rolfe measured the variations in transatlantic signals at 41 MHz [52]. They measured BBC transmission from Britain crossing to Canada, and noted how the direction of arrival and signal strength varied over several months.

In 1964, Ossanna looks at how the urban environment affects fading through a received power spectrum [53]. Using measurements made with a mobile receiver, the power spectra are computed and the fading at different frequencies is compared. Similarly, Nylund performed mobile measurements at 150 MHz, and showed that the fading caused by multi-path in urban, sub-urban, and rural environments is all Rayleigh distributed [54].

Allsebrook and Parsons performed measurements on television signals around British cities in 1977 [55]. The results were compared to an area model by Okumura, and evaluated the differences between flat urban and sloping urban environments. They indicated that in all cases, the buildings present in an urban environment played an important role in computing the loss, and, likewise, in a hilly environment, knowledge of the terrain was an important factor. Parsons, et al., continued their examination of path loss in 1983, examining signal levels in rural areas [56]. They determined that higher frequencies had larger path loss than was otherwise predicted by present models, even accounting for Rayleigh fading.

Durden, Klein, and Zebker measured the effects of foliage on both the amplitude and phase of signals at UHF, L-band, and C-band [57]. Their 1993 experiment transmitted from the ground under a canopy up to an aircraft passing overhead. Their results were compared to detailed Monte-Carlo simulations of transmission through foliage. This is an example of many similar tests which have been done to attempt to isolate the effects of single elements on the transmitted signal, in this case foliage.

Like the foliage measurements of Durden, a number of recent studies have focused on propagation in special cases. Owen and Pudney performed indoor measurements at 900 MHz and 1700 MHz [58]. Zhang, et al., in 1998, measured propagation within long-wall face coal mines at 900 MHz [59]. In 1999, Kim, et al., measured the signal at 908 MHz and 1900 MHz at street level in an Urban high-rise environment. The results were compared with 2D and 3D ray tracing models [60]. Rodriguez, Martinez, and Garcia-Pardo likewise did testing of reception at street level in the urban environment in 2009 and compared to several urban

area prediction models [61].

In 2000, Rao, et al., measured several VHF and UHF television signals in urban, suburban, and rural environments in India [62]. The measurements were compared to a wide variety of area-prediction path loss models, with the Hata model providing the best predictions.

In 2003, Savage and Ndzi carried out a thorough study of propagation through foliage [63]. Measurements were conducted at 1.3 GHz, 2.0 GHz, and 11.6 GHz at a variety of sites with differing types of foliage. They determined that leaf state, vegetation density, and forest geometry were the predominant factors in predicting foliage attenuation, and were much more important that tree species or leaf shape.

2.2   Radio Propagation Models

The goal of a propagation model is to provide a technique which can be used to predict the losses in a radio system. Propagation models attempt to predict the losses in power which occur from the point where the signal leaves the radiator to its arrival in the vicinity of the receiving antenna or other point of interest. For terrestrial propagation, this is usually for a communications link between two points over the earth. Thus, a propagation model may include the effects of the atmosphere, the terrain, foliage, man made structures, or other items which affect the propagation of radio waves [64].

Much work has been done in developing techniques for dealing with each of these various

sources of loss (or gain). This work is focussed on the propagation effects specifically associated with the terrain. Non-flat or irregular terrain can cause loss or gain from reflections, refraction, shadowing, blockage, and diffuse multi-path. Thus, many different techniques have been developed to deal with the variety of mechanisms. Existing models can generally be divided in two different types, empirical/statistical models, and theoretical models.

Empirical Models

Beverage produced a summary and comparison of experimental work on ultra high frequency propagation in 1937 [65]. His comparison suggested that for higher frequencies, propagation could be modeled effectively with a combination of optical techniques. Using reflection for line-of-sight paths, and diffraction and refraction for over-the-horizon paths, the rate of decay could be predicted accurately. However, he notes that past studies disagree on results for the sky wave, or ionospheric refraction paths, with results appearing to rely on many long term factors such as the solar cycle.

In 1947, Bullington summarized much of the work done to that point and provided a collection of tables that could be used for estimating losses from various factors [66]. His work included free space loss, tropospheric scatter, Rayleigh fading, ridge-line diffraction, and a summary of experimental results for over-the-horizon cases. He also included near-field effects for foliage, buildings, and nearby hills. The tables could provide estimates for a wide variety of specific design cases, and were useful above 30 MHz. The work was updated and revised in 1957, with more data for higher frequencies [64].

Epstein and Peterson developed an empirical model accounting for most propagation effects in 1953 [67]. Their work was based on tests they carried out in the vicinity of New York City [38], and combined the use of knife-edge diffraction models for obstructions with additional empirical evidence. They acknowledged that additional work was needed in both theory and measurements to improve the model.

Also in 1957, Egli presented a formula for predicting median terrain loss based upon published surveys of RF losses between 40 MHz and 1 GHz [68]. Egli's model is simple and is still useful as a quick method for predicting the general level of loss [2], as it requires knowledge of only the heights of the antennas, the distance between them, and the frequency of the signal. However, it does not account for specific terrain features, and is thus only a very general prediction tool.

Longley, Rice, et al. developed a detailed computer model for propagation during the 1960's [69]. The model requires detailed inputs of many terrain statistics to provide a prediction. It can be used in either an area mode, which uses statistics of the terrain to predict signal levels over a region, or a point-to-point mode, which uses a terrain profile in addition to statistics. The National Telecommunications and Information Administration (NTIA) currently provides an improved form of their model called the Irregular Terrain Model (ITM) [70]. The ITM is currently incorporated into many commercial prediction products [2].

Quasi-smooth terrain was dealt with by Hata in 1980 [71]. His empirical formula was developed from urban propagation data in Japan. The Hata model uses inputs of distance,

frequency, and antenna heights and provides gross correction values for large cities, small cities, suburban areas, and open terrain. Hata emphasizes that the formula, while useful for planning purposes, is limited in the terrestrial range over which it is accurate. Because the Hata model is valid in the frequency ranges and distances which are used in this work, it will be used for a baseline comparison. The parameters of the Hata model are laid out in section 6.4.

2.2.1   Theoretical Models

Theoretical models were developed along with the empirical models, but have become more prevalent as computing power has increased. The theoretical models attempt to use a simplification of the path data, along with electromagnetic theory, to produce a specific point-to-point terrain loss estimate. Following are models based on integral equation methods, diffraction theory, and optical theory. Because these models account for the specific terrain effects and are based on topographic data, the goal is to be more precise than the general median loss predictions of the empirical models.

The first theoretical solution to account for an antenna radiating in the presence of a dielectric ground was published by Sommerfeld in 1909 [72]. His solution shows how a vertically oriented dipole should radiate in the presence of a flat ground plane. Although the ground is not perfectly flat, his solution provides a means of computing how an antenna should radiate within nearly flat regions. In 1918, Watson presents the solution for a dipole

radiating over a spherical earth [73]. His solution expands upon the flat dielectric solution of Sommerfeld, and shows how waves should diffract around the globe when the wavelength is sufficiently large to consider the earth smooth.

In 1933, Schelleng, Burrows, and Ferrell present a framework for using ray optics, that is reflection, refraction, and diffraction, to account for higher frequency propagation [74]. The authors demonstrate that refraction can be approximated by the use of a larger earth radius in the diffraction computations. They also show that experimental measurements of refraction suggests that a four-thirds earth radius best fits the average atmospheric profile. Burrows took Watson's solution for a smooth spherical earth and expanded it for an atmosphere with variable dielectric properties [75]. Burrows shows that the use of a four-thirds earth radius approximation sufficiently accounts for the variable atmosphere in the spherical earth model.

Norton published a pair of papers in 1936 and 1937 which collected the prior computations, simplified their results, and showed the distances and frequency ranges in which they had been experimentally validated [76, 77]. He also provided formulas for computing the electric field over the earth from the current distribution on an antenna. He expanded on this, summarizing recent results and providing computed ground wave curves, in 1941 [78]. Burrows and Gray also presented similar curves in 1941 [79].

Rice produced a pair of works in 1944 and 1948 covering the combination of signal and noise [80, 81]. These two works developed the statistical nature of received signals in the presence of interference. Rice shows that such signals should have random fading following

what is now known as the Rician distribution. While not specifically a propagation model, the work was foundational in laying the statistical basis for future models.

A different simple theoretical model was developed by Friis in 1946 [82]. The formula, now known as the Friis Transmission Formula, is derived from basic principals of conservation of power, and defines the concept of effective area of an antenna. The formula predicts how signals should behave in an unobstructed line-of-sight environment. Although Friis does not develop the specifics, he suggest modifications to the formula for use in the presence of terrain and lossy media. Norton developed many of these potential modifications, as well as modifications for the inclusion of antenna patterns and a variety of system losses, publishing his results in 1953 [83].

In 1952, Hufford presented an integral equation approach to solving the terrain scattering problem [84]. Hufford suggests that the integral equation approach should be the most accurate, as it accounts for all methods by which the ground may affect propagation (multiple reflections and diffractions as well as ground waves). He used a Leontovich boundary condition to simplify the coupled scalar equations into a single equation. Hufford's equation is a Volterra integral equation which accounts only for forward scattering. He showed that his method provided accurate approximate solutions to the problems of scattering from a flat surface and a curved earth. However, other problems were computationally intractable at the time.

In 1968, Clarke developed a statistical treatment of the prediction problem [85]. Without going into detail as to the specific sources of reflection or diffraction, he assumes that the

signal received by a mobile receiver will be composed of randomly time-delayed plane waves arriving from random directions. At high enough frequencies, where the random time-delays are large enough to introduce completely random phase, this will produce either a Rayleigh distribution if no coherent signal is present, or a Rician distribution for a coherent signal in the presence of incoherent multi-path. These results are then compared to experimental data for mobile receivers.

Ott and Berry followed on from Hufford's work in 1970 by looking at large slopes and terrain features, and showing that the results compare favorably to those predicted by knife-edge diffraction [86, 87]. Like Hufford's equation, Ott's integral equation is also a Volterra equation accounting only for forward scattering. Ott also showed that numerical solution of the integral equation could produce additional information about field, such as showing a focusing at the top of a hill, which diffraction theory did not provide. Later, Ott compared numerical results from this work to measurements taken in the VHF range, showing favorable results at intermediate ranges [88].

As was previously mentioned, Epstein's work in 1953 relied on both empirical modeling and the theory of knife-edge diffraction [67]. Vogler applies diffraction across multiple knife-edges to the propagation problem [89]. Meeks applies the multiple knife-edge diffraction technique to paths with experimental data [90]. Meeks showed that a two knife-edge diffraction model did a satisfactory job of providing predictions for line-of-site paths, but broke down in more obstructed paths.

During the same time frame, the application of the Geometric Theory of Diffraction

(GTD) to the propagation problem was undertaken by Chamberlin and Luebbers [91]. They used GTD to predict the diffraction from terrain by simulating terrain features with wedges. The results were compared to the Longley-Rice model and measured data. Luebbers also compared the GTD model to Meek's data [92] to show the improved accuracy of GTD over the knife-edge theory in more obstructed regions. Geometric optics and GTD is well summarized by Deschamps [93]. Additional improvements to optical theory, resulting in the Uniform Theory of Diffraction (UTD), were made by Kouyoumjian and Pathak in the 1974, eliminating the singularity that exists in the GTD solution at the shadow boundary [94].

Ott showed an improved integral equation method in 1992 [95]. This method removed several of the assumptions about the shape of the surface which had been made in the development of previous integral equations. The new equation exhibited better numerical stability and provided useful results into the UHF range of frequencies.

At the same time, Janaswamy developed a Fredholm integral equation for propagation prediction [96]. This equation accounted for both forward and backward propagation, but was much more time intensive to solve than Ott's equation. Thus Janaswamy deemed it unsuitable for large propagation problems, but good for dealing with near-source obstructions.

In 1994, Eppink and Kuebler produced the Terrain Integrated Rough Earth Model (TIREM) for the US military [97]. This model consolidates many of the previously produced empirical and theoretical models into one coherent collection with rules for when each should be used. TIREM uses different models for line-of-sight and beyond-line-of-sight propagation, as well as different techniques for over ground and over water propagation.

Furthermore, different models are used in different frequency ranges.

Hviid suggests the use of a perfect magnetic conductor (PMC) as the ground surface for an electric field integral equation approach to a propagation solution for vertical polarization [98]. This assumption is justified as the reflection coefficient for both real ground and a PMC approach -1 as grazing incidence is approached. Hviid also converts his integral to a Volterra type equation by assuming only forward scattering is important.

Fernandez, et al., examine the application of the spectrally accelerated forward-backward (FBSA) method to terrain profiles [99]. The results are compared to those obtained with the full forward-backward method, however results are not compared to any other prediction methods. Tunc, et al., do compare the FBSA method to the Epstein-Peterson method as well as to the ITU-R and Hviid's integral equation method [100]. They show that the FBSA method compares well with the Epstein-Peterson results. However, unlike the present work they focus on frequencies in the 200 MHz to 900 MHz range. Additionally, their paths have very minor terrain height variations of only forty or fifty meters.

2.3   MOM and MOMI

Love, building on the work of both Kirchoff and Green, developed both the theory of reciprocity and the equivalence theory, presenting them in 1901 [101]. The equivalence theory, which comes from the uniqueness properties for solutions of Maxwell's equations, states that knowledge of the tangential electromagnetic fields along the closed boundary of a region is

sufficient to compute the fields within the region. Additionally, the tangential fields along the boundary cause the fields to vanish outside the region.

Schelkunoff showed in 1936 that these tangential fields along the boundary are equivalent to electric and magnetic currents along the boundary surface, and the computation of the fields within the region is accomplished by computing the radiation from the equivalent currents [102]. Additionally, Schelkunoff explains how the equivalence theorem can be used to break apart a problem into regions of homogeneous material properties, thus simplifying the radiation in each region. Applying the equivalence condition to the electric field along a boundary produces the electric field integral equation, while applying it to the magnetic field produces the magnetic field integral equation.

Rumsey published the reaction method for discretizing electromagnetics problems in 1954 [103]. In 1966, Harrington, building on Rumsey's work, applied the method of moments (MOM), or variational method, to electromagnetic field problems with the goal of utilizing computers for their solution [104]. Harrington's treatment has since been the basis for numerical solution of electromagnetic boundary value problems. His work covers the means of discretizing many equations used in electromagnetics, including the electric field integral equation (EFIE), for numerical solution of radiation and scattering problems by creating a matrix equation from the integral equation.

Numerous solution methods have been proposed for solving large-scale integral equations in electromagnetics. Peterson, Ray, and Mittra [8], as well as Morita, Kumagai, and Mautz [105] both cover many methods for numerical solution. But of particular interest

for rough surface scattering, in 1995, Kapp described the method of ordered multiple interactions (MOMI) [106], while Holliday, et al., develop a very similar forward-backward method [107]. These two techniques both focus on an iterative method for solving the magnetic field integral equation (MFIE) over a PEC surface to provide a faster solution than direct matrix inversion can provide. Forward-backward separates the effects of forward and backward propagation along the surface. These forward and backward propagations are then alternately considered until convergence is attained, usually in a short time. The alternate MOMI formulation shows that any ordering, not just forward and backwards along the surface, can be considered, and provides a firm linear algebra basis for the solution technique. Furthermore, MOMI frames the solution as a preconditioning method which develops an alternate integral equation.

Many improvements were made to these techniques in following years. Holliday, et al., showed that equations for highly-lossy materials can be solved with the forward-backward method [108]. Adams and Brown combined the fast multipole method (FMM) with MOMI to create a faster method for large bodies [109]. Chou and Johnson similarly showed a spectral acceleration method for forward-backward (FBSA) which can be applied to the Electric Field Integral Equation (EFIE) [110]. Meanwhile, Toporkov, et al., showed that a more rigorous inclusion of surface curvature provides a significant gain in the ability to reduce sampling in an integral equation approach [111]. More recently, Iodice addressed the use of forward-backward on dielectric interfaces was of limited usefulness, as it often did not converge [112]. However, Westin later showed that these convergence issues could be

overcome [113].

Chapter 3

Propagation Computation Techniques

This chapter develops the necessary tools for the computation of electric and magnetic fields in two dimensions. The work presented here is based upon fundamental electromagnetic theory and has been well covered by numerous authors [7,114–117]. The following derivations form the foundation that is necessary for the solution of the propagation and scattering problem. To develop MOMI and to use it to compute the radio propagation on a path, it is necessary to describe how currents, the sources of electromagnetic radiation, produce the fields. First the radiation integral will be derived, then the radiation specific to a line source, and a current sheet are developed. All of the following work is done in time harmonic form, assuming all quantities oscillate at a single frequency, ω, and a $e^{j\omega t}$ time variation which has been suppressed in all of the equations.
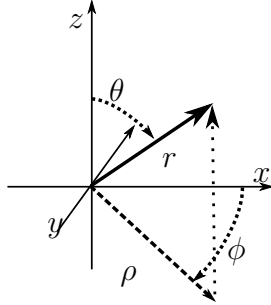
Figure 3.1: Basic co-ordinate systems.

In following chapters, this basis will allow the construction of integral equations which describe the multiple interactions of equivalent currents induced along an interface. Those integral equations can be solved in numeric form to provide a solution to the scattering problem. The formulations in this chapter will also serve to show how the equivalent currents, once known numerically, radiate to produce the scattered field.

Figure 3.1 shows the three basic coordinate systems. This includes cartesian, (x, y, z), cylindrical, (ρ, ϕ, z), and spherical, (r, θ, ϕ). All three systems are used extensively throughout the following chapters, and interchanged to utilize whichever form is most convenient for the task at hand.

3.1   Justification for 2D Modelling

One of the basic assumptions used throughout the rest of this thesis is that a two-dimensional model is useful for path loss computations. Certainly, of the entirety of the propagation models presented in chapter 2, almost all the point-to-point models use the great circle

path between two points on the earth for the prediction and ignore effects from outside that plane. The exceptions to this are a few intra-city models dealing with the effects of buildings. However, just because others have done it that way is not sufficient justification.

Hufford does address the question in the development of his integral equation [84]. His integral equation is developed from a three dimensional formulation by examining stationary phase locations for the transmitter and receiver path. By utilizing a prolate spheroidal coordinate system, with the transmitter and receiver at the foci, the stationary phase points are defined as those in which the gradient of the ground surface is tangential to the spheroids. Under this geometry, the direct path between the transmitter and receiver contains stationary phase points for any surface. However, while outside of the direct path some points of reflection or diffraction may exist, they are dependant on geometry and should be much more rare. For a more complete model, such points could be computed from topographic data transformed to the prolate spheroidal system and optics used to compute their effects. However, following the lead of other point-to-point propagation models, this work will focus on computing the effects along the great cirlce path using two-dimensional computations.

3.2   General Form for Time Harmonic Radiation

The first step to consider is the formulation of the fields radiated by a time harmonic current. Maxwell's equations are given below in time harmonic form with both the magnetic and electric currents, **M** and **J** [7]. While **M** may not exist in reality, it provides a useful

mathematical extension of the equations, introducing a symmetry which will aid in providing complete solutions [114].

$$\nabla \times \mathbf{E} = -j\omega\mathbf{B} - \mathbf{M} \tag{3.1a}$$

$$\nabla \times \mathbf{H} = j\omega\mathbf{D} + \mathbf{J} \tag{3.1b}$$

$$\nabla \cdot \mathbf{B} = q_m \tag{3.1c}$$

$$\nabla \cdot \mathbf{D} = q_e \tag{3.1d}$$

Here, $\mathbf{E}$ is the electric field, and $\mathbf{D}$ is the electric flux density. Similarly, $\mathbf{H}$ is the magnetic field, and $\mathbf{B}$ is the magnetic flux density. q_e and q_m are the electric charge and magnetic charge, respectively [7]. All of these quantities are functions of space and harmonic in time. The constitutive equations are also needed to complete the system of equations. These are

$$\mathbf{B} = \mu\mathbf{H} \tag{3.2a}$$

$$\mathbf{D} = \epsilon\mathbf{E} \tag{3.2b}$$

$$\mathbf{J} = \sigma\mathbf{E} \tag{3.2c}$$

The constitutive equations define the material properties and their impact on the fields by relating the magnetic field to its flux density and the electric field to its flux density, as well as how currents arise in conductive media. In free space these properties are $\mu_0 = 4\pi \times 10^{-7}$ H/m, $\epsilon_0 \simeq 8.854 \times 10^{-12}$ F/m, and $\sigma = 0$, with the subscript 0 signifying the free space quantity. In addition, the material properties can be incorporated as an impedance, $\eta = \sqrt{\mu/\epsilon}$, and a wavenumber, $k = \omega\sqrt{\mu\epsilon}$. Combining (3.1a) and (3.1b) with

(3.2a) and (3.2b) yields the more concise coupled pair of equations

$$\nabla \times \mathbf{E} = -j\omega\mu\mathbf{H} - \mathbf{M} \tag{3.3a}$$

$$\nabla \times \mathbf{H} = j\omega\epsilon\mathbf{E} + \mathbf{J} \tag{3.3b}$$

For the purposes of developing radiation principles, i.e. the production of fields by currents, the region under consideration is assumed to be homogeneous and free of magnetic sources. Magnetic sources will be dealt with later through duality. The construction of the radiated field can be accomplished through the introduction of a new quantity, the magnetic vector potential, **A**, which is defined such that the curl of the vector potential equals the magnetic flux density.

$$\mathbf{B} = \mu\mathbf{H} = \nabla \times \mathbf{A} \tag{3.4}$$

The prupose of introducing the vector potential is to provide a straightforward way to compute the fields based on the electric currents [114]. Thus, the vector potential has been introduced for convenience. The scalar electric potential, Φ, is defined by combining (3.3a) with (3.4). Because there are no magnetic currents in the region, and the curl of a gradient is zero, Φ is defined via its gradient.

$$\mathbf{E} + j\omega\mathbf{A} = -\nabla\Phi \tag{3.5}$$

Finally, because only the curl of the vector potential has been defined so far, the divergence of **A** is specified using the Lorenz gauge [7]. This gauge is used because it preserves

the property of propagation of source information through the potentials at the speed of light. The definition is given in (3.6).

$$\nabla \cdot \mathbf{A} = -j\omega\epsilon\mu\Phi \tag{3.6}$$

By applying the Lorenz gauge with (3.3b), and noting that, by defintion, $k^2 = \omega^2\mu\epsilon$, the vector wave equation for $\mathbf{A}$ is obtained. It will be shown that, because $\mathbf{A}$ satisfies this wave equation, the computation of the magnetic vector potential from the electric current density will be possible through an integration of $\mathbf{A}$ with a suitable Green's function [115].

$$\nabla^2\mathbf{A} + k^2\mathbf{A} = -\mathbf{J} \tag{3.7}$$

Combining (3.5) and (3.7) and considering (3.4), the solutions for the magnetic and electric fields in simple media in terms of $\mathbf{A}$ are

$$\mathbf{H} = \frac{1}{\mu}\nabla \times \mathbf{A} \tag{3.8a}$$

$$\mathbf{E} = -j\omega\mathbf{A} + \frac{1}{j\omega\mu\epsilon}\nabla(\nabla \cdot \mathbf{A}) \tag{3.8b}$$

By taking advantage of the symmetry of Maxwell's Equations, i.e., changing the conditions so that $\mathbf{J} = 0$ and considering the presence of magnetic sources $\mathbf{M}$, an electric vector potential $\mathbf{F}$ can be defined in terms of the electric field.

$$\mathbf{D} = \epsilon\mathbf{E} = -\nabla \times \mathbf{F} \tag{3.9}$$

And, by using duality, that is a combination of the symmetry and linearity of Maxwell's equations [7], the equivalent solution for the magnetic field from $\mathbf{F}$ is derived by the simple

replacement of symmetric terms in (3.8b).

$$\mathbf{H} = -j\omega\mathbf{F} + \frac{1}{j\omega\mu\epsilon}\nabla(\nabla \cdot \mathbf{F}) \tag{3.10}$$

Because the system is linear and superposition holds, combining the fields from the electric and magnetic vector potentials yields a final form which can be used for further radiation computations [114]. This form describes the full electric and magnetic fields in terms of the vector potentials, and thus from electric and magnetic current sources.

$$\mathbf{E} = -\nabla \times \mathbf{F} - j\omega\mathbf{A} + \frac{1}{j\omega\mu\epsilon}\nabla(\nabla \cdot \mathbf{A}) \tag{3.11a}$$

$$\mathbf{H} = \nabla \times \mathbf{A} - j\omega\mathbf{F} + \frac{1}{j\omega\mu\epsilon}\nabla(\nabla \cdot \mathbf{F}) \tag{3.11b}$$

3.2.1 Computation of the Vector Potentials

The relationships above describe the process of computing the electric and magnetic fields given the vector potentials $\mathbf{A}$ and $\mathbf{F}$. One route to attain formulas for the computation of these quantities is through the use of Green's theorems and Green's functions [7]. Green's theorems are mathematical identities defining a symmetry relationship between two functions. Using Green's theorems to relate the vector potential created by a current to the vector potential created by a point source, which is termed a Green's function, results in a simple form for computing the potentials.

The scalar Green's theorem is based on the mathematical vector identity in (3.12).

$$\nabla \cdot (\psi\nabla\phi) = \psi\nabla^2\phi + \nabla\psi \cdot \nabla\phi \tag{3.12}$$

Here ψ and ϕ are any scalar functions of space. Green's first identity is the result of integrating both sides of the above equation in all three dimensions and applying the divergence theorem to the left hand side [7].

$$\oiint \psi \frac{\partial \phi}{\partial n} ds = \iiint (\psi \nabla^2 \phi + \nabla \psi \cdot \nabla \phi) dv \tag{3.13}$$

The left hand side is a surface integral over the surface bounding the region of the volume integral on the right hand side, and $\frac{\partial}{\partial n}$ is the derivative with respect to the normal of the boundary surface.

Switching ψ and ϕ and then subtracting the new result from the above form produces Green's second identity.

$$\oiint \left(\psi \frac{\partial \phi}{\partial n} - \phi \frac{\partial \psi}{\partial n} \right) ds = \iiint \left(\psi \nabla^2 \phi - \phi \nabla^2 \psi \right) dv \tag{3.14}$$

One particular Green's function is defined by solving for the radiation due to a point source. Thus, for the purpose of computing $\mathbf{A}$, the Green's function is chosen to satisfy the homogeneous wave equation (3.7) for a spatially impulsilsive source and to be zero at the boundary at infinity [118]. Note that the vector components of $\mathbf{A}$ and $\mathbf{J}$ can be separated into Cartesian coordinates and solved for independently. An $\hat{\mathbf{x}}$ oriented current will give rise only to an $\hat{\mathbf{x}}$ oriented vector potential. So the vector wave equation is then simplified into a scalar wave equation.

$$\nabla^2 A(r) + k^2 A(r) = -J(r) \tag{3.15}$$

For a Green's function, the source is a spatial point source. Therefore, the Green's function

satisfies the following equation.

$$\nabla^2 G(r) + k^2 G(r) = -\delta(r) \tag{3.16}$$

This equation will be solved in the following section for the radiation from a line source. For now, consider that the Green's function is any function that satisfies (3.16) and goes to zero at infinite distance.

The intent is to use (3.14) along with a function satisfying (3.16) to obtain a solution for the potential A which satisfies (3.15). To do this, let $\psi = A(\mathbf{r}_0)$ and $\phi = G(\mathbf{r} - \mathbf{r}_0)$. By combining (3.14) with (3.15) and (3.16), the result is

$$\oiint \left(A(\mathbf{r}_0) \frac{\partial G}{\partial n}(\mathbf{r} - \mathbf{r}_0) - G(\mathbf{r} - \mathbf{r}_0) \frac{\partial A}{\partial n}(\mathbf{r}_0) \right) \mathrm{d}s_0 = \iiint \left(-A(\mathbf{r}_0)\delta(\mathbf{r} - \mathbf{r}_0) + J(\mathbf{r}_0)G(\mathbf{r} - ro) \right) \mathrm{d}v_0$$

$$\tag{3.17}$$

By allowing the region of integration to go to infinity and assuming the radiation condition, that both G and its normal derivative go to zero at infinity and that A is finite, the left hand side of the equation reduces to zero. In the right hand side, the integration with the delta function simplifies the result to a formula for the computation of A from J.

$$A(\mathbf{r}) = \iiint J(\mathbf{r}_0)G(\mathbf{r} - \mathbf{r}_0)\mathrm{d}v_0 \tag{3.18}$$

This scalar result can be expanded to all three vector components by referring again to the reasoning by which the vector wave equation for $\mathbf{A}$ was collapsed to a scalar wave equation for A. This was done since each vector component in the current contributes only to the corresponding vector component in the potential. Also, by again considering duality,

the result for the electric vector potential is obtained by replacing $\mathbf{J}$ with $\mathbf{M}$ and $\mathbf{A}$ with $\mathbf{F}$.

$$\mathbf{A}(\mathbf{r}) = \int \mathbf{J}(\mathbf{r}_0)G(\mathbf{r} - \mathbf{r}_0)\mathrm{d}v_0 \tag{3.19}$$

$$\mathbf{F}(\mathbf{r}) = \int \mathbf{M}(\mathbf{r}_0)G(\mathbf{r} - \mathbf{r}_0)\mathrm{d}v_0 \tag{3.20}$$

What still remains for a complete solution to the computation of the fields is to determine the form of the Green's function. In two dimensions, this is accomplished by examining the radiation from a line current.

3.3   Field of a Line Source

The primary source of interest for two-dimensional computations will be either an infinite magnetic or electric line source. In the two-dimensional spaces under consideration, all currents will be taken to be line sources of infinite length. The field of a $\hat{\mathbf{z}}$ directed electric line source passing through the origin will be computed. This source will then be translated into an arbitrarily directed source at a general location, and the fields resulting from an equivalent magnetic line source will be derived using duality.

3.3.1   General Solution for a Line Source

Consider a line of electric current, I_e, oriented in the $\hat{\mathbf{z}}$ direction along the z-axis and radiating in free space. This current can be represented by the following equation, where ρ is the

distance from the origin of the x-y plane.

$$\mathbf{J}_i(\mathbf{r}) = \hat{\mathbf{z}} I_e \delta(x)\delta(y) = \hat{\mathbf{z}} I_e \delta(\rho) \tag{3.21}$$

Using the vector wave equation, (3.7), remember that, as previously noted, $\mathbf{A}$ will have the same vector components as $\mathbf{J}$. Thus, computations are limited to A_z and (3.7) becomes

$$\left[\nabla^2 + k^2\right] A_z = I_e \delta(\rho). \tag{3.22}$$

This scalar wave equation is separable in cylindrical coordinates, for which the solution of the wave equation is available. The proposed form of A_z is

$$A_z = C B_n(k_\rho \rho) h(n\phi) h(k_z z) \tag{3.23}$$

where $B_n(x)$ is a Bessel Function of order n, and $h(x)$ is a harmonic function, either a sine, cosine, or complex exponential, C is a constant, and $k^2 = k_\rho^2 + k_z^2$ [7].

Because there is no impetus in the system for variations around ϕ, $h(n\phi)$ is assumed to be a constant, that is $n = 0$. In this case, $h(n\phi) = 1$. For the k_z term, either a positive or negative complex exponential is used, representing a wave travelling in either the negative or positive $\hat{\mathbf{z}}$ direction, respectively. Finally, because outward travelling waves are expected from the source, and to satisfy the boundary condition of zero fields as ρ approaches infinity, the Hankel function of the second kind $H_0^{(2)}(k_\rho \rho)$ is chosen for $B_0(k_\rho \rho)$. The general form is then given the more specific form as below.

$$A_z = C H_0^{(2)}(k_\rho \rho) e^{\pm j k_z z} \tag{3.24}$$

By assuming that I_e is constant and not a function of z, consistent with (3.21), k_z can be assumed to be zero. This simplifies the expression, and results in $k_\rho = k_0$. This assumption implies no variation in the $\hat{\mathbf{z}}$ direction within the source current. When placed into (3.23), only the constant C remains to be found.

$$A_z = CH_0^{(2)}(k_0\rho) \tag{3.25}$$

Ampere's Law states that the circle around the source must contain the current passing through that point [119]. The constant C can be obtained by examining the integral form of (3.1b) in the limit around the origin.

$$\lim_{\rho \to 0} \oint \mathbf{H} \cdot \mathrm{d}\boldsymbol{l} = I_e$$

$$\lim_{\rho \to 0} \oint -Ck_0\rho H_0^{(2)\prime}(k_0\rho)\mathrm{d}\phi = I_e\mu$$

Note that $H_0^{(2)\prime}(x) = -H_1^{(2)}(x)$. The asymptotic form for a small argument of $H_1^{(2)}(k_0\rho)$ can be used in the limit, providing a computable expression [6].

$$\lim_{\rho \to 0} C \oint k_0\rho \left[\frac{k_0\rho}{2 \cdot 2!} + j\frac{0!}{\pi}\frac{2}{k_0\rho} \right] \mathrm{d}\phi = I_e\mu$$

$$C = \frac{I_e\mu}{4j} \tag{3.26}$$

Substituting C back into (3.25) then provides a complete form for $\mathbf{A}$ with a $\hat{\mathbf{z}}$-directed line current.

$$\mathbf{A} = \hat{\mathbf{z}}\frac{I_e\mu}{4j}H_0^{(2)}(k_0\rho) \tag{3.27}$$

Referring back to (3.8b) and (3.8a) with (3.27), and taking the derivatives, provides the final formulation of the fields radiated by a line source in free space in cylindrical coordinates.

$$\mathbf{H} = \hat{\boldsymbol{\phi}}\frac{I_e k_0}{4j}H_1^{(2)}(k_0\rho) \tag{3.28a}$$

$$\mathbf{E} = -\hat{\mathbf{z}}\frac{I_e\omega\mu}{4}H_0^{(2)}(k_0\rho) \tag{3.28b}$$

Using duality to replace the electric line source with a magnetic line source, $\mathbf{M} = \hat{\mathbf{z}}I_m\delta(\rho)$, the fields due to the latter are also obtained.

$$\mathbf{H} = -\hat{\mathbf{z}}\frac{I_m\omega\epsilon}{4}H_0^{(2)}(k_0\rho) \tag{3.29a}$$

$$\mathbf{E} = -\hat{\boldsymbol{\phi}}\frac{I_m k_0}{4j}H_1^{(2)}(k_0\rho) \tag{3.29b}$$

3.3.2   Green's Function

Comparing (3.16) with (3.27) provides the Green's function that was previously described. Therefore, the Green's function to be used for two-dimensional radiation is:

$$\boxed{G(\mathbf{r} - \mathbf{r}_0) = \frac{1}{4j}H_0^{(2)}\left(k_0\left|\mathbf{r} - \mathbf{r}_0\right|\right)} \tag{3.30}$$

3.4   Fields From Surface Currents

The primary goal of the propagation work is to find the fields scattered by the surface. To do this, the fields will be computed from the equivalent currents along the boundary. While the topic of equivalent currents is covered in chapter 4, it will be necessary to evaluate

the fields scattered by a surface current in a simple medium. Such a computation can be undertaken by first computing the vector potential from the surface currents, and from that the electric and magnetic fields. However, it would be more direct, and more computationally efficient, to develop the Dyadic Green's functions for the direct computation of the electric and magnetic fields. Furthermore, by eliminating the need for a discrete approximation of the curl or divergence, the results should be more accurate. The three dimensional result for surface current radiation is covered in texts, such as by Van Bladel [120], and Tai [121]. However, to the author's knowledge, the two dimensional case has only recently been covered by Westin [113], and by Black in unpublished work [122].

Starting from the Green's function for the magnetic vector potential shown in (3.30), the vector potential is the integral over the surface current.

$$\mathbf{A} = \int_{S_0} \mathbf{J}(\mathbf{r}_0) G\left(|\mathbf{r} - \mathbf{r}_0|\right) \mathrm{d}l_0 \tag{3.31}$$

$$\tag{3.32}$$

This equation is then substituted in to (3.8b) and (3.8a) to provide the form for the fields.

$$\mathbf{H} = \frac{1}{\mu} \nabla \times \int_{S_0} \mathbf{J}(\mathbf{r}_0) G\left(k_0|\mathbf{r} - \mathbf{r}_0|\right) \mathrm{d}l_0 \tag{3.33a}$$

$$\mathbf{E} = \left[-j\omega + \frac{1}{j\omega\mu\epsilon} \nabla \left\{\nabla \cdot\right\}\right] \int_{S_0} \mathbf{J}(\mathbf{r}_0) G\left(k_0|\mathbf{r} - \mathbf{r}_0|\right) \mathrm{d}l_0 \tag{3.33b}$$

The notation of (3.33b) with the un-applied derivatives inside the square brakets should be taken to mean that the integral is distributed to both terms and then the divergence is taken
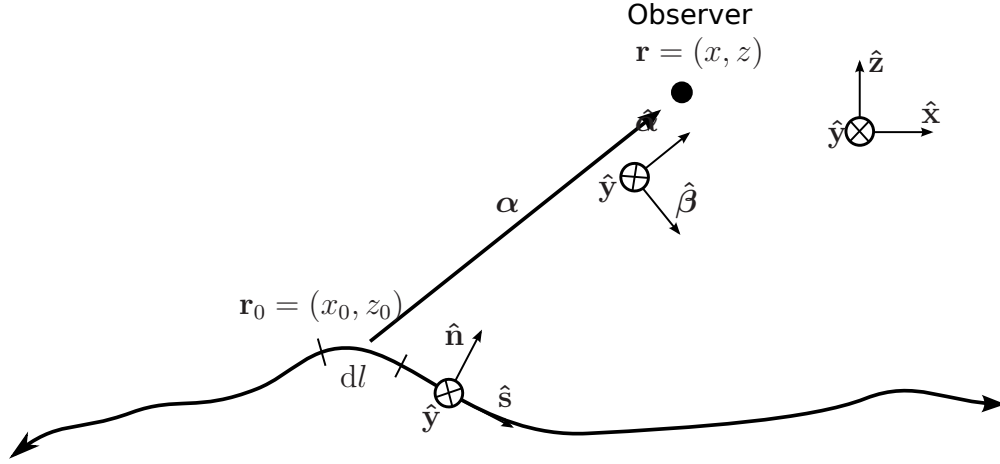
Figure 3.2: Coordinate systems used in surface current radiation.

as appropriate. Because the integrals and derivatives are operating on different variables, and they must exist, they may be interchanged. Furthermore, it should be noted that the r-derivative operating on the current, $\mathbf{J}(\mathbf{r}_0)$, yields zero since $\mathbf{r}_0$ does not depend on $\mathbf{r}$.

Expanding the previous equations in this way produces

$$\mathbf{H} = -\frac{1}{\mu} \int_{S_0} \mathbf{J}(\mathbf{r}_0) \times \nabla G\left(k_0|\mathbf{r} - \mathbf{r}_0|\right) \mathrm{d}l_0 \tag{3.34a}$$

$$\mathbf{E} = \frac{1}{j\omega} \int_{S_0} \left[\omega^2 \mathbf{J}(\mathbf{r}_0) G\left(k_0|\mathbf{r} - \mathbf{r}_0|\right) + \frac{1}{\mu\epsilon} \left\{ \mathbf{J}(\mathbf{r}_0) \cdot \nabla \right\} \nabla G\left(k_0|\mathbf{r} - \mathbf{r}_0|\right) \right] \mathrm{d}l_0 \tag{3.34b}$$

For convenience, two ortho-normal right-handed vector systems are defined. Figure 3.2 shows the two coordinate systems in the presence of the surface. The first system is for the surface described as described in the x-z plane, the $\{\hat{\mathbf{n}}, \hat{\mathbf{s}}, \hat{\mathbf{y}}\}$ triplet, where $\hat{\mathbf{n}}$ is the unit surface normal, and $\hat{\mathbf{s}}$ is unit vector tangential to the surface, can describe the direction of the current flow at a point on the surface. Currents will point along the surface in either the $\hat{\mathbf{s}}$ or $\hat{\mathbf{y}}$ directions, they can not point through the surface – in the $\hat{\mathbf{n}}$ direction. The second

system, the $\{\hat{\boldsymbol{\alpha}}, \hat{\boldsymbol{\beta}}, \hat{\mathbf{y}}\}$ triplet describes the cylindrical system around a given point in space, where $\boldsymbol{\alpha} = \mathbf{r} - \mathbf{r}_0$, and $\boldsymbol{\beta} = \hat{\mathbf{y}} \times \boldsymbol{\alpha}$. These are equivalent to the $\hat{\boldsymbol{\rho}}$ and $\hat{\boldsymbol{\phi}}$ directions in a normal cylindrical system around a line source, but in this case $\hat{\boldsymbol{\alpha}}$ and $\hat{\boldsymbol{\beta}}$ change direction as the source or observation point moves.

To simplify the computations, the transverse electric (TE) and transverse magnetic (TM) cases will be dealt with separately. The TE case involves electric fields pointing in the $\hat{\mathbf{y}}$ direction only, so $\mathbf{J}(\mathbf{r}_0) = \hat{\mathbf{y}} J(x_0)$. The TM case consists of magnetic fields directed in the $\hat{\mathbf{y}}$ direction only; for the TM case, $\mathbf{J}(\mathbf{r}_0) = \hat{\mathbf{s}} J(x_0)$. These two orientations provide a complete basis for solutions to the two-dimensional scattering problem [7]. It will also be convenient to first evaluate the necessary derivatives. Appendix A contains the details of the computation of the derivatives, but the results are summarized here.

$$G\left(k_0|\mathbf{r} - \mathbf{r}_0|\right) = \frac{\mu}{4j} H_0^{(2)}\left(k_0\alpha\right) \tag{3.35a}$$

$$\nabla G\left(k_0\alpha\right) = \hat{\boldsymbol{\alpha}}\frac{k_0\mu}{4j} H_1^{(2)}\left(k_0\alpha\right) \tag{3.35b}$$

$$\left(\hat{\mathbf{y}} \cdot \nabla\right) \nabla G\left(k_0\alpha\right) = 0 \tag{3.35c}$$

$$\left(\hat{\mathbf{s}} \cdot \nabla\right) \nabla G\left(k_0\alpha\right) = \frac{\mu}{4j} \left[(\hat{\mathbf{s}} \cdot \hat{\boldsymbol{\alpha}})(\hat{\boldsymbol{\alpha}} \cdot \nabla) + (\hat{\mathbf{s}} \cdot \hat{\boldsymbol{\beta}})(\hat{\boldsymbol{\beta}} \cdot \nabla)\right] \nabla H_0^{(2)}\left(k_0\alpha\right) \tag{3.35d}$$

$$\left(\hat{\boldsymbol{\alpha}} \cdot \nabla\right) \nabla G(\boldsymbol{\alpha}) = -\hat{\boldsymbol{\alpha}}\frac{k_0^2}{4j} \left[H_0^{(2)}\left(k_0\alpha\right)\right.$$
$$\left. + \frac{1}{k_0\alpha} H_1^{(2)}\left(k_0\alpha\right)\right] \tag{3.35e}$$

$$\left(\hat{\boldsymbol{\beta}} \cdot \nabla\right) \nabla G(\boldsymbol{\alpha}) = -\frac{k_0}{4j\alpha} H_1^{(2)}\left(k_0\alpha\right) \hat{\boldsymbol{\beta}} \tag{3.35f}$$

Combining (3.34a) and (3.34b) with the above equations and substituting in for the TE

case, the resulting scattering integrals are

$$\mathbf{H}_{TE} = \frac{jk_0}{4} \int_{S_0} -\hat{\boldsymbol{\beta}} J(x_0) H_1^{(2)}(k_0\alpha) \, \mathrm{d}l_0 \tag{3.36a}$$

$$\mathbf{E}_{TE} = \hat{\mathbf{y}} \frac{\eta k_0}{4} \int_{S_0} J(x_0) H_0^{(2)}(k_0\alpha) \, \mathrm{d}l_0 \tag{3.36b}$$

For the TM case, the scattering integral results are

$$\mathbf{H}_{TM} = -\hat{\mathbf{y}} \frac{jk_0}{4} \int_{S_0} (\hat{\boldsymbol{\beta}} \cdot \hat{\mathbf{s}}_0) J(x_0) H_1^{(2)}(k_0\alpha) \, \mathrm{d}l_0 \tag{3.37a}$$

$$
\begin{aligned}
\mathbf{E}_{TM} = \frac{\eta k_0}{4} \int_{S_0} \Bigg[& \hat{\boldsymbol{\beta}}(\hat{\boldsymbol{\beta}} \cdot \hat{\mathbf{s}}_0) \left(H_0^{(2)}(k_0\alpha) - \frac{H_1^{(2)}(k_0\alpha)}{k_0\alpha} \right) \\
& + \hat{\boldsymbol{\alpha}}(\hat{\boldsymbol{\alpha}} \cdot \hat{\mathbf{s}}_0) \frac{H_1^{(2)}(k_0\alpha)}{k_0\alpha} \Bigg] J(x_0) \mathrm{d}l_0
\end{aligned}
\tag{3.37b}
$$

When implemented numerically, the vectors in these integrals are projected onto Cartesian coordinates, since $\hat{\boldsymbol{\alpha}}$, $\hat{\boldsymbol{\beta}}$, $\hat{\mathbf{s}}$, and $\hat{\mathbf{n}}$ all change with both $\mathbf{r}$ and $\mathbf{r}_0$. The above sets of equations are used to compute the fields scattered from the equivalent currents along the ground for a propagation path.

3.5   Summary

This chapter has provided the basic propagation computations which are the basis of this work. Starting from Maxwell's Equations the fields produced by an electric or magnetic line current have been developed. From there, the two dimensional Green's function was inferred, and an expression was developed for the fields created by an electric surface current. These equations are used both directly in the computations performed for this work as well as to provide the foundation for the formulations in Chapter 4.

Chapter 4

Method of Ordered Multiple Interactions

The previous chapter developed the necessary equations to compute the field that is scattered from a current sheet, as well as the field radiated by a line source. However, the main difficulty in solving a scattering problem is in computing the equivalent currents along the interface [123]. This chapter develops the techniques which are used to solve the current problem. The first part of the chapter derives the magnetic field integral equation (MFIE). The method of moments (MOM) is then applied to the MFIE to produce a linear system of algebraic equations which can be solved for a numerical solution of the MFIE. Finally, the method of ordered multiple interactions (MOMI) is presented as the preferred solution technique for the system of equations when the propagator matrix is large.

The reason for using the MFIE is that it provides an exact representation of the scattering problem, to within the computational tolerance specified, unlike approximate methods such as physical or geometric optics [123]. Solution accuracy is important for determining the effects of what may be small changes in the terrain on the overall solution.

4.1 The Equivalence Principle

Scattering problems in electromagnetics are often solved by the application of the equivalence principle. A unique solution to Maxwell's equations can be guaranteed in a region by defining either the tangential electric or magnetic field on the region's boundary and the interior sources [7]. Similarly, currents on a surface cause discontinuities in the tangential field at that surface [102]. These currents have the form

$$\mathbf{J}_s = \hat{\mathbf{n}} \times [\mathbf{H}_{out} - \mathbf{H}_{in}] \tag{4.1}$$

$$\mathbf{M}_s = -\hat{\mathbf{n}} \times [\mathbf{E}_{out} - \mathbf{E}_{in}] \tag{4.2}$$

where $\hat{\mathbf{n}}$ is the outward facing surface normal, $(\mathbf{E}_{out}, \mathbf{H}_{out})$ are the fields outside the surface, and $(\mathbf{E}_{in}, \mathbf{H}_{in})$ are the inner fields.

Love and Schelkunoff showed that the introduction of currents along the boundary, representing the tangential fields along the boundary, cause the fields to go to zero inside of the bounded region while staying unchanged outside [101, 102]. Additionally, since the fields inside the region are now null, the material in that region can be changed to anything which is desired, specifically matching the material of the other region, without affecting the prob-

lem. This allows radiation of the currents to occur entirely in a homogeneous medium, which is the problem we solved in the previous chapter. The equivalence principle allows the division of a problem with inhomogeneous media into multiple connected problems of regions of homogeneous media bounded by surface currents. The advantage to this approach is that computing the fields produced by currents in homogeneous simple media is straightforward because the homogeneous Green's function is known.

Also of import is the fact that the fields in a perfect conductor must be zero. Since the perfect electric conductor (PEC) has no tangential electric field on the boundary, $\mathbf{M}_s$ must be zero [7]. Thus, only electric surface currents exist on the PEC boundary. Finally, since the fields in the PEC region are zero, and this nullity is enforced by the surface current, the PEC can be removed from the problem if the currents remain and are left to radiate in free space. This is because any object in a region of null fields should have no effect on other objects.

4.2   The Magnetic Field Integral Equation

The MFIE is derived by evaluating the tangential total fields at the boundary, including the effects of the equivalent current upon itself. The problem that is considered here utilizes a PEC for the earth surface. Following the basic MFIE formulation, the singular term is evaluated, and the remaining principle value integral is then discretized using the method of moments. In evaluating the integral under the MOM formulation, it is considered in both
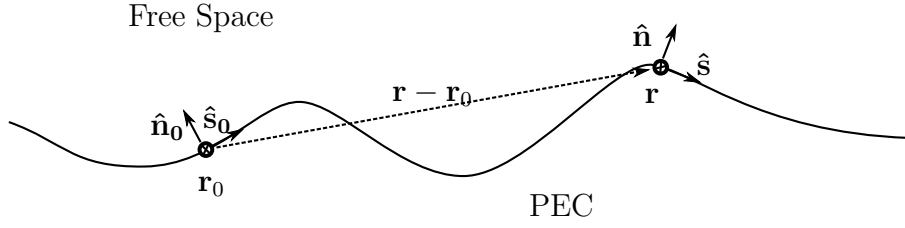
Figure 4.1: Vectors along the surface for the MFIE.

polarizations, with special treatment given to the discretization of the self patch, or diagonal element of the matrix.

Because the fields in a PEC are known, the surface current along the PEC has a simplified form. The inner region is defined as the area consisting of the PEC material and it has already been noted that $\mathbf{M}_s = 0$. Also, the superposition of fields from currents is well established, so the total field above the PEC is divided into the incident fields, $\mathbf{E}_i$ and $\mathbf{H}_i$, and the fields scattered from the surface, $\mathbf{E}_s$ and $\mathbf{H}_s$, and

$$\mathbf{J}_s(\mathbf{r}) = \hat{\mathbf{n}} \times \mathbf{H}(\mathbf{r})|_S = \hat{\mathbf{n}} \times \mathbf{H}_i(\mathbf{r})|_S + \hat{\mathbf{n}} \times \mathbf{H}_s(\mathbf{r})|_S \tag{4.3}$$

Figure 4.1 shows the coordinates for the MFIE surface, including the vectors at the surface points $\mathbf{r}$, the observation point, and $\mathbf{r}_0$, the source point. Combining (4.3) with (3.11b) and (3.19) yields the following.

$$\hat{\mathbf{n}} \times \mathbf{H}(\mathbf{r})|_S = \hat{\mathbf{n}} \times \mathbf{H}_i(\mathbf{r})|_S + \hat{\mathbf{n}} \times \frac{1}{\mu} \nabla \times \oint_S \mathbf{J}_s(\mathbf{r}_0) G(\mathbf{r} - \mathbf{r}_0) \mathrm{d}s_0|_{\mathbf{r} \to S} \tag{4.4}$$

Note that the derivative of the Green's function has a singularity at the point $\mathbf{r} = \mathbf{r}_0$. Thus, two modifications will be made to the integral. Firstly, the region, as specified, is

for a closed surface; for the purposes of solving propagation problems, the surface will be considered to extend to infinity, and for power to be conserved, the tangential field at infinity must be zero. Thus, the closed aspect of the integral will be dropped with that understanding. Secondly, the singularity must be integrated separately from the remainder; the finite part of the integral will be evaluated, and the remainder will become a principal value integral over the surface [105].

4.2.1   Finite Part Evaluation

The singularity arises in a two-fold situation. The fields are not continuous at the surface, so the point $\mathbf{r}$ under consideration must be the limit as $\mathbf{r}$ approaches the surface. The limit from above the surface will be considered, adapted from the technique of Morita, Kumagai, and Mautz, but the same equation is obtained if the development considers the limit from below the surface [105]. The singularity then arises as $\mathbf{r}_0$ approaches $\mathbf{r}$ in the integration. Thus, the surface of integration, S, will be split into regions S_Δ and $S - S_\Delta$. Here, let Δ be the half-width of a narrow region excluded from the general integral. The integral over $S - S_\Delta$ becomes the principal value integral in the limit. Thus, the region left to consider is the region within S_Δ. For the singular part, the coordinate system will be oriented around the point of the singularity, with x along the surface, and z along the normal. Figure 4.2 shows these coordinates oriented around the singular point, which is the origin of the coordinate system.
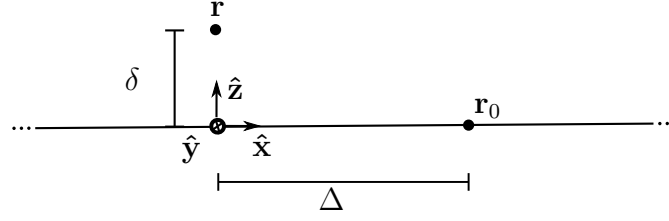
Figure 4.2: Coordinates for computing the integral across the singularity for the MFIE.

Expressing the prior statement mathematically, the principle part is

$$L = \lim_{\Delta \to 0} \lim_{\mathbf{r} \to S} \hat{\mathbf{n}} \times \nabla \times \int_{S_\Delta} \mathbf{J}_s(\mathbf{r}_0) G(\mathbf{r} - \mathbf{r}_0) \mathrm{d}s_0 \tag{4.5}$$

Bringing the differential and the cross product with the surface normal into the integral and distributing them through the product, this becomes

$$L = \lim_{\Delta \to 0} \lim_{\mathbf{r} \to S} \frac{1}{\mu} \int_{S_\Delta} \left[\nabla G(\mathbf{r} - \mathbf{r}_0) \left(\hat{\mathbf{n}} \cdot \mathbf{J}_s(\mathbf{r}_0) \right) - \mathbf{J}_s(\mathbf{r}_0) \left(\hat{\mathbf{n}} \cdot \nabla G(\mathbf{r} - \mathbf{r}_0) \right) \right] \mathrm{d}s_0$$

Note that in the case of a slowly changing surface, $\hat{\mathbf{n}}$ which is vertical, and $\mathbf{J}$ are nearly perpendicular, and thus, the first part goes to zero. Also, note that $\hat{\mathbf{n}} \cdot \nabla G = \frac{\partial G}{\partial n}$.

$$L = \lim_{\Delta \to 0} \lim_{\mathbf{r} \to S} -\frac{1}{\mu} \int_{S_\Delta} \mathbf{J}_s(\mathbf{r}_0) \frac{\partial G}{\partial n} (\mathbf{r} - \mathbf{r}_0) \mathrm{d}s_0 \tag{4.6}$$

Here, let $\mathbf{r}$ be defined as $\delta \hat{\mathbf{z}}$, where δ will go to zero in the limit. Also, let the curvature be small, so that $\mathbf{r}_0 = x_0 \hat{\mathbf{x}}$ and $\mathrm{d}s_0 = \mathrm{d}x_0$. Also, at this point, the assumption of a two dimensional system in a simple medium will be made. Thus, the Green's function will be that developed for the line current in (3.27). Making that substitution into (4.6) results in (4.7).

$$L = \lim_{\Delta \to 0} \lim_{\delta \to 0} -\int_{S_\Delta} \mathbf{J}_s(x_0) \frac{\partial}{\partial n} \frac{1}{4j} H_0^{(2)}(k_0 |\mathbf{r} - \mathbf{r}_0|) \mathrm{d}x_0 \tag{4.7}$$

Knowing that $\frac{\partial}{\partial n} = \frac{\partial}{\partial z}$, and defining $R = |\mathbf{r} - \mathbf{r}_0|$, the integral term becomes

$$L = \lim_{\Delta \to 0} \lim_{\delta \to 0} \frac{k_0}{4j} \int_{S_\Delta} \mathbf{J}_s(x_0) H_1^{(2)}(k_0 R) \frac{\delta}{R} \mathrm{d}x_0 \tag{4.8}$$

Now, since the limit as $\mathbf{r}$ approaches the surface, and as $\mathbf{r}_0$ approaches $\mathbf{r}$ is under consideration, the small argument approximation to the Hankel function is an appropriate substitution. Thus that substitution is made [6], and the equation is simplified.

$$L = \lim_{\Delta \to 0} \lim_{\delta \to 0} \frac{k_0}{4j} \int_{S_\Delta} \mathbf{J}_s(x_0) \left[-j \frac{2}{\pi k_0 R} \right] \frac{\delta}{R} \mathrm{d}x_0$$

$$L = \lim_{\Delta \to 0} \lim_{\delta \to 0} \int_{S_\Delta} \mathbf{J}_s(x_0) \frac{\delta}{2\pi R^2} \mathrm{d}x_0 \tag{4.9}$$

By assuming that $\mathbf{J}_s(\mathbf{r}_0)$ is slowly changing, and thus constant over the integration region, it can be assumed that in the region under consideration $\mathbf{J}_s(\mathbf{r}_0) = \mathbf{J}_s(\mathbf{r})$, and removed from the integral. Also, by the Pythagorian theorem, $R^2 = \delta^2 + x^2$ and the limits of S_Δ are from $-\Delta$ to Δ.

$$L = \lim_{\Delta \to 0} \lim_{\delta \to 0} \mathbf{J}_s(\mathbf{r}) \frac{\delta}{2\pi} \int_{-\Delta}^{\Delta} \frac{1}{\delta^2 + x^2} \mathrm{d}x_0 \tag{4.10}$$

Finally, integrating yields a function which can be evaluated in the limits.

$$L = \lim_{\Delta \to 0} \lim_{\delta \to 0} \mathbf{J}_s(\mathbf{r}) \frac{1}{2\pi} \left[\arctan \frac{\Delta}{\delta} - \arctan \frac{-\Delta}{\delta} \right] \tag{4.11}$$

Applying the limit on δ first [105], the $\arctan \pm\infty = \pm\pi/2$, and this yields (4.5) equal to:

$$L = \frac{\mathbf{J}_s(\mathbf{r})}{2} \tag{4.12}$$

When placed back in to (4.4), along with the Cauchy Principal Value integral of the remainder, this provides the magnetic field integral equation in the form it is commonly seen.

$$\mathbf{J}_s(\mathbf{r}) = 2\hat{\mathbf{n}} \times \mathbf{H}_i + \frac{2}{\mu}\hat{\mathbf{n}} \times \oint_S \nabla G(\mathbf{r} - \mathbf{r}_0) \times \mathbf{J}_s(\mathbf{r}_0)ds_0 \tag{4.13}$$

4.2.2   TE Kernel

At this point, it is appropriate to separate the problem into the TE and TM cases. For the TE case, the assumption is made that the electric field is only present in the $\hat{\mathbf{y}}$ direction, or horizontal polarization, while the magnetic field is in the $\hat{\mathbf{x}}$ and $\hat{\mathbf{z}}$ directions. Since the surface normal is also in the x-z plane, the currents that are excited by the incident field will be solely in the $\hat{\mathbf{y}}$ direction. Therefore, the surface currents $\mathbf{J}_s$ will be replaced by the quantity $\hat{\mathbf{y}}J_s$. Following this line of reasoning, and replacing $\nabla G(\mathbf{r} - \mathbf{r}_0)$ with its equivalent from (3.35b), allows equation (4.13) to be specified as

$$\hat{\mathbf{y}}J_s(\mathbf{r}) = 2\hat{\mathbf{n}} \times \mathbf{H}_i(\mathbf{r}) + \frac{k_0}{j2}\hat{\mathbf{n}} \times \oint_S \hat{\boldsymbol{\alpha}}H_1^{(2)}(k_0\alpha) \times \hat{\mathbf{y}}J_s(\mathbf{r}_0)ds_0 \tag{4.14}$$

Using the vector identity $\mathbf{A} \times (\mathbf{B} \times \mathbf{C}) = \mathbf{B}(\mathbf{A} \cdot \mathbf{C}) - \mathbf{C}(\mathbf{A} \cdot \mathbf{B})$, the expression $\hat{\mathbf{n}} \times (\hat{\boldsymbol{\alpha}} \times \hat{\mathbf{y}})$ becomes $-\hat{\mathbf{y}}(\hat{\mathbf{n}} \cdot \hat{\boldsymbol{\alpha}})$. Thus (4.14) is simplified to (4.15), where all quantities are in the $\hat{\mathbf{y}}$ direction, and $J_0 = \hat{\mathbf{y}} \cdot (2\hat{\mathbf{n}} \times \mathbf{H}_i(\mathbf{r}))$.

$$J_s(\mathbf{r}) = J_0 - \frac{k_0}{j2}\oint_S (\hat{\mathbf{n}} \cdot \hat{\boldsymbol{\alpha}})H_1^{(2)}(k_0\alpha) J_s(\mathbf{r}_0)ds_0 \tag{4.15}$$

4.2.3   TM Kernel

In the TM case, vertical polarization, the assumption is that the magnetic field is only present in the $\hat{\mathbf{y}}$ direction and the electric field will be in the $\hat{\mathbf{x}}$ and $\hat{\mathbf{z}}$ directions. Likewise, any electric currents arising from the $\hat{\mathbf{n}} \times \hat{\mathbf{y}}$ product will point in the $\hat{\mathbf{s}}$ direction. Therefore, surface currents $\mathbf{J}_s$ will be replaced by the quantity $\hat{\mathbf{s}} J_s$. Here, a new notation of $\hat{\mathbf{s}}_0$ and $\hat{\mathbf{n}}_0$ are introduced, representing the surface and normal directions at the point $\mathbf{r}_0$. Using similar techniques to those in the TE case, the integrand of the MFIE can be specified for the TM case, and result in:

$$\hat{\mathbf{s}} J_s(\mathbf{r}) = 2\hat{\mathbf{n}} \times \mathbf{H}_i(\mathbf{r}) + \frac{k_0}{j2}\hat{\mathbf{n}} \times \oint_S \hat{\boldsymbol{\alpha}} H_1^{(2)}(k_0\alpha) \times \hat{\mathbf{s}}_0 J_s(\mathbf{r}_0)\mathrm{d}s_0 \qquad (4.16)$$

By replacing $\hat{\mathbf{s}}_0$ with $\hat{\mathbf{y}} \times \hat{\mathbf{n}}_0$, and applying the same identity as in the TE case, $\hat{\boldsymbol{\alpha}} \times \hat{\mathbf{s}}_0$ can be expanded first to $\hat{\boldsymbol{\alpha}} \times (\hat{\mathbf{y}} \times \hat{\mathbf{n}}_0)$, and then reduced to $\hat{\mathbf{y}}(\hat{\boldsymbol{\alpha}} \cdot \hat{\mathbf{n}}_0)$. Then $\hat{\mathbf{n}} \times [\hat{\mathbf{y}}(\hat{\boldsymbol{\alpha}} \cdot \hat{\mathbf{n}}_0)] = -\hat{\mathbf{s}}(\hat{\mathbf{n}}_0 \cdot \hat{\boldsymbol{\alpha}})$. Finally, for the TM case, allow $J_0 = \hat{\mathbf{s}} \cdot (2\hat{\mathbf{n}} \times \mathbf{H}_i(\mathbf{r}))$, and with all components in the $\hat{\mathbf{s}}$ direction,

$$J_s(\mathbf{r}) = J_0 - \frac{k_0}{j2}\oint_S (\hat{\mathbf{n}}_0 \cdot \hat{\boldsymbol{\alpha}}) H_1^{(2)}(k_0\alpha) J_s(\mathbf{r}_0)\mathrm{d}s_0 \qquad (4.17)$$

4.2.4   Combined TE/TM Form

A comparison of (4.15) and (4.17) shows that the TE and TM cases are similar. In fact, a simplifying notation for the Green's function can be obtained by adopting the notation of $\hat{\mathbf{n}}_{[0]}$ which represents the use of $\hat{\mathbf{n}}$ in the TE case and $\hat{\mathbf{n}}_0$ in the TM case. Then the kernel of

the integral equation becomes

$$G_{MFIE}(\mathbf{r}, \mathbf{r}_0) = -\frac{k_0}{j2}(\hat{\mathbf{n}}_{[0]} \cdot \hat{\boldsymbol{\alpha}})H_1^{(2)}(k_0\alpha) \tag{4.18}$$

Thus, adopting the notation of J_0 for each case, the equations can be broken apart into scalar form as follows.

$$J_s(\mathbf{r}) = J_0(\mathbf{r}) - \frac{k_0}{j2}\int_S (\hat{\mathbf{n}}_{[0]} \cdot \hat{\boldsymbol{\alpha}})H_1^{(2)}(k_0\alpha)\,J_s(\mathbf{r}_0)\mathrm{d}s_0 \tag{4.19}$$

4.3   Numerical Solution

The MFIE describes the currents along the surface of a conductor due to the fields incident on the surface. For a closed body, the fields consist of those incident on the body from an external region and the fields which are radiated by the currents induced on the body. The integral term in the MFIE describes those fields produced by the latter. For numerical solutions, the MFIE is first transformed into a matrix equation by the method of moments. This matrix equation can be solved many ways. For smaller matrices, solution with normal numerical linear algebra libraries such as LAPACK is the simplest solution method [124]. However, for large matrices which may exceed available computer storage, iteration is a more viable method because the matrix need not be stored [106]. In this thesis, iteration is used following a preconditioning procedure known as the method of ordered multiple interactions.

4.3.1   Method of Moments

The MFIE can be solved numerically by applying the method of moments (MOM), also known as the method of weighted residuals. Following Harrington's work as a guide, the discretation is presented with rectangular pulse basis functions and impulse testing functions [125]. The basis functions $b^m(x)$ are assumed to be rectangular pulses of width Δx and centered at location $m\Delta x$. Then the solution of $J_s(x)$ can be approximated by $\sum_{m=A}^{B} J_s^m b^m(x)$ where J_s^m is the value of J_s at the center of the m'th pulse. Likewise $J_0(x)$ can be approximated by $\sum_{m=A}^{B} J_0^m b^m(x)$. Thus the MFIE at this stage is approximated by equation (4.20).

$$\sum_{m=A}^{B} J_s^m b_m(x) = \sum_{m=A}^{B} J_0^m b_m(x) - \frac{k_0}{j2}\oint_S (\hat{\mathbf{n}}_{[0]} \cdot \hat{\boldsymbol{\alpha}})H_1^{(2)}(k_0\alpha)\sum_{m=A}^{B} J_s^m b^m(x_0)\mathrm{d}s_0 \qquad (4.20)$$

Testing functions $t^n(x) = \delta(x - n\Delta x)$ are then used to define a set of independent equations. The set of N testing functions multiply each term in (4.20) and are integrated. In this case, a testing function is located at the center of each basis function. Thus, a set of N independent equations, given by (4.21), with $A < n < B$ is created.

$$J_s^n = J_0^n - \sum_{m=A}^{B} J_s^m \frac{k_0}{j2}\oint_{m\Delta x - \frac{\Delta x}{2}}^{m\Delta x + \frac{\Delta x}{2}} \left[(\hat{\mathbf{n}}_{[0]} \cdot \hat{\boldsymbol{\alpha}})H_1^{(2)}(k_0\alpha)\sqrt{1 + \zeta_x^2(x_0)}\mathrm{d}x_0\right]_{x=n\Delta x} \qquad (4.21)$$

The integral in equation (4.21), referred to as P_{mn} and called the kernel or propagator, must be evaluated for all integer values of m and n. When $n \neq m$, the assumption is made that the support of the integral is small enough that the integrands are nearly constant and can be removed from the integral.

$$P_{mn} = -\frac{k_0}{j2}\int_{m\Delta x-\frac{\Delta x}{2}}^{m\Delta x+\frac{\Delta x}{2}}\left[(\hat{\mathbf{n}}_{[0]}\cdot\hat{\boldsymbol{\alpha}})H_1^{(2)}\left(k_0\alpha\right)\sqrt{1+\zeta_x^2(x_0)}\mathrm{d}x_0\right]_{x=n\Delta x}$$

$$P_{mn} \simeq -\left[(\hat{\mathbf{n}}_{[0]}\cdot\hat{\boldsymbol{\alpha}})H_1^{(2)}\left(k_0\alpha\right)\sqrt{1+\zeta_x^2(x_0)}\Delta x\right]_{x=n\Delta x,x_0=m\Delta x}, \quad m\neq n \qquad (4.22)$$

In the case where $n = m$, the terms must be expanded to evaluate the near field interactions along the surface. The self-patch term is evaluated by introducing a Taylor series expansion for the surface around the center of the patch. The first order term of the self-patch evaluates to one; however, Toporkov, et al., showed that MOMI convergence is improved when the third order term is included as well [111]. To do this, the TE and TM cases must again be evaluated independently.

TE Curvature Term

To evaluate the integral of (4.21) when $n = m$, $\hat{\mathbf{n}}$ and $\boldsymbol{\alpha}$ are replaced by the equivalent forms in terms of the surface function, $\zeta(x)$, and its derivatives. Likewise, the Hankel function is replaced by the small argument approximation. Also, a change of variables is performed, with $x' = x_0 - m\Delta x$. Figure 4.3 shows the coordinates around the single self-patch.

$$P_{mm}^{TE} = -\frac{k_0}{j2}\int_{m\Delta x-\frac{\Delta x}{2}}^{m\Delta x+\frac{\Delta x}{2}}(\hat{\mathbf{n}}\cdot\hat{\boldsymbol{\alpha}})H_1^{(2)}\left(k_0\alpha\right)\sqrt{1+\zeta_x^2(x_0)}\mathrm{d}x_0$$

$$P_{mm}^{TE} \simeq \frac{1}{\pi}\int_{-\frac{\Delta x}{2}}^{\frac{\Delta x}{2}}\frac{\left[-x'\zeta_x(m\Delta x)-(\zeta(x)-\zeta(x'+m\Delta x))\right]\sqrt{1+\zeta_x^2(x'+m\Delta x)}}{\left[x'^2+(\zeta(m\Delta x)-\zeta(x'+m\Delta x))^2\right]\sqrt{1+\zeta_x^2(m\Delta x)}}\mathrm{d}x'$$
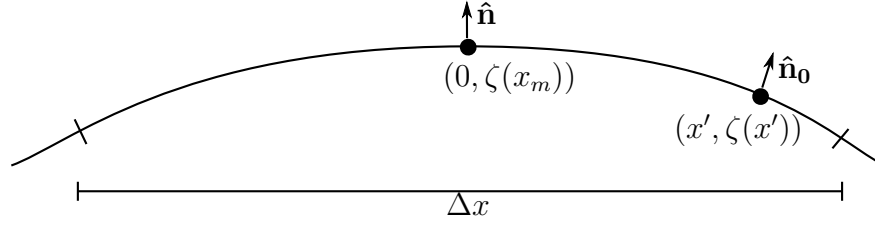
Figure 4.3: Coordinates for computing the self-patch term of the MFIE.

Because the region of integration is small, the Taylor series is used to represent the surface. It is assumed that sampling is dense enough that error is minimal from the third order and greater terms.

$$\zeta(m\Delta x + x') = \zeta(m\Delta x) + x'\zeta_x(m\Delta x) + \frac{x'^2}{2}\zeta_{xx}(m\Delta x) + ... \tag{4.23}$$

$$\zeta_x(m\Delta x + x') = \zeta_x(m\Delta x) + x'\zeta_{xx}(m\Delta x) + ... \tag{4.24}$$

Thus, the propagator self term, with the Taylor series expansion of the surface is shown in equation (4.25). For ease of notation, from this point on, the location $m\Delta x$ will be suppressed when it is the location at which surface quantities are evaluated, i.e. $\zeta_x = \zeta_x(m\Delta x)$.

$$P_{mm}^{TE} = \frac{1}{2\pi}\int_{-\frac{\Delta x}{2}}^{\frac{\Delta x}{2}} \frac{-\zeta_{xx}\sqrt{1 + \zeta_x^2 + 2x'\zeta_x\zeta_{xx} + x'^2\zeta_{xx}^2}}{1 + \zeta_x^2 + x'\zeta_x\zeta_{xx} + \frac{x'^2}{4}\zeta_{xx}^2\sqrt{1 + \zeta_x^2}}\,\mathrm{d}x' \tag{4.25}$$

Finally an assumption about the length of Δx must be made. Making the assumption that Δx is small enough to force $1 + \zeta_x^2 \gg x'\zeta_x\zeta_{xx} + (x'^2/4)\zeta_{xx}$ and $1 + \zeta_x^2 \gg 2x'\zeta_x\zeta_{xx} + x'^2\zeta_{xx}^2$ in the region of integration, an accurate approximation of the self patch term can be computed. This assumption must be kept in mind in the implementation of any solution. Thus,

the TE self-term is given by equation (4.26).

$$P_{mm}^{TE} = -\frac{1}{2\pi}\frac{\zeta_{xx}\Delta x}{1+\zeta_x^2} \tag{4.26}$$

TM Curvature Term

The TM case is computed in a similar fashion to the TE case. The difference is that the normal used for the dot product in the propagator is changing throughout the region of integration. Below is the equation for the TM case, starting with equation (4.21), and substituting in the small argument approximation for the Hankel function and the proper surface elements for the dot product.

$$P_{mm}^{TM} = \frac{k_0}{j2}\int_{m\Delta x-\frac{\Delta x}{2}}^{m\Delta x+\frac{\Delta x}{2}} (\hat{\mathbf{n}}_0\cdot\hat{\boldsymbol{\alpha}})H_1^{(2)}(k_0\alpha)\sqrt{1+\zeta_x^2(x_0)}dx_0$$

$$P_{mm}^{TM} \simeq \frac{1}{\pi}\int_{-\frac{\Delta x}{2}}^{+\frac{\Delta x}{2}} \frac{x'\zeta_x(m\Delta x+x')+(\zeta(m\Delta x)-\zeta(x'+m\Delta x))}{x'^2+(\zeta(m\Delta x)-\zeta(x'+m\Delta x))^2}\,dx'$$

Then by utilizing the Taylor series for the surface out to the second derivative terms, the equation above simplifies to (4.27).

$$P_{mm}^{TM} = \frac{1}{2\pi}\int_{-\frac{\Delta x}{2}}^{+\frac{\Delta x}{2}} \frac{\zeta_{xx}}{1+\zeta_x^2+x'\zeta_x\zeta_{xx}+\frac{x'^2}{4}\zeta_{xx}^2}\,dx' \tag{4.27}$$

Again, making the assumption that $1+\zeta_x^2 \gg x'\zeta_x\zeta_{xx}+(x'^2/4)\zeta_{xx}$ in the integration region, the result is obtained. The TM result differs from the TE case by only a sign change.

$$P_{mm}^{TM} = \frac{1}{2\pi}\frac{\zeta_{xx}\Delta x}{1+\zeta_x^2} \tag{4.28}$$

MOM Solution

Having reduced each integral in the MOM process to a numerical result, the outcome is a set

of N equations, one for each testing function, with M unknowns, one for each basis function.

By substituting the notation of P for the integral of equation (4.21) the resulting equations

have the form of (4.29).

$$J_s^n = J_0^n + \sum_{m=A}^{B} J_s^m P_{mn} \tag{4.29}$$

This set of linear equations is then ordered into a matrix equation with column vectors

$\mathbf{J_s}$, the unknown, and $\mathbf{J_0}$, the source term, both of length N, and the M by N matrix P.

$$\mathbf{J_s} = \mathbf{J_0} + P\mathbf{J_s} \tag{4.30}$$

The solution to this equation can be obtained by iteration if the matrix is too large to

invert. If the matrix is invertible, then the solution is straightforward, with the quantity

$P\mathbf{J_s}$ being moved to the left side, and then left multiplied by the inverse, $(I - P)^{-1}$. Thus,

the result for the unknown current $\mathbf{J_s}$ is finally obtained.

$$\mathbf{J_s} = (I - P)^{-1}\mathbf{J_0} \tag{4.31}$$

4.3.2   Method of Ordered Multiple Interactions

As mentioned before, the discretized MFIE may be solved for very large matrices by iteration.

In this case, however, convergence is often slow [106]. Preconditioning techniques may be

employed to speed the convergence. One such technique, which this work will use, is the method of ordered multiple interactions, so named because it separates the propagator matrix into diagonal and triangular matrices which account for unidirectional propagation. MOMI was developed by Kapp, and further refined by others, with the inclusion of the more accurate diagonal term by Toporkov [106, 111].

Development

Starting with the discretized MFIE, the propagator is separated into a lower triangular matrix, a diagonal matrix, and an upper triangular matrix. The lower triangular matrix, L, represents all propagation from left to right along the surface. The upper triangular matrix, U, likewise represents all right to left propagation. Finally, the diagonal matrix, $\hat{D}$, represents the self interactions of the currents.

$$P = L + \hat{D} + U \tag{4.32}$$

Combinining this expansion of P with (4.31) produces:

$$\left(I - \hat{D} - L - U\right)\mathbf{J} = \mathbf{J}_0 \tag{4.33}$$

With the addition of the proper terms, the left hand side of the above equation can be factored, leaving terms which are simple to invert. The diagonal matrix $D = I - \hat{D}$ is used to consolidate the pair of terms.

$$\left(D - L - U + LD^{-1}U\right)\mathbf{J} = \mathbf{J}_0 + LD^{-1}U\mathbf{J}$$

$$(D - L)\,D^{-1}\,(D - U)\,\mathbf{J} = \mathbf{J}_0 + LD^{-1}U\mathbf{J}$$

By inverting the left hand side, a new matrix equation is obtained. Here, because the terms being inverted are triangular matrices operating on a column vector, the inversion operation is straightforward to perform by forward or backward substitution.

$$\mathbf{J} = (D - U)^{-1} D (D - L)^{-1} \mathbf{J}_0 + (D - U)^{-1} D (D - L)^{-1} L D^{-1} U \mathbf{J} \qquad (4.34)$$

When solving by Neumann iteration, (4.34) becomes

$$\mathbf{J}_{[N]} = \sum_{n=0}^{N} (D - U)^{-1} \left[D (D - L)^{-1} L D^{-1} U (D - U)^{-1} \right]^{n} D (D - L)^{-1} \mathbf{J}_0 \qquad (4.35)$$

where $\mathbf{J}_{[N]}$ is the Nth iterate of the MOMI integral equation.

While the above expression is useful in providing an understanding of MOMI from a physical perspective, that is by iteratively scattering forwards and backwards along the surface, it can be computations improved for implementation. Several multiplications and an inversion may be removed from the solution by the use of a transformation performed by Kapp [106]. Allowing $A = D - L$ and $B = D - U$, and performing an expansion and refactorization on the iterative term of the summation produces the following simplification.

$$D(D - L)^{-1} L D^{-1} U (D - U)^{-1} = D B^{-1} (D - B) D^{-1} (D - A) A^{-1}$$

$$= \left(D B^{-1} - I \right) \left(D A^{-1} - I \right)$$

$$= \left[D (D - L)^{-1} - I \right] \left[D (D - U)^{-1} - I \right] \qquad (4.36)$$

Substituting (4.36) into (4.35) provides a result which is computationally faster because it includes fewer matrix inversions.

$$\mathbf{J}_{[N]} = \sum_{n=0}^{N} (D - U)^{-1} \left(\left[D (D - L)^{-1} - I \right] \left[D (D - U)^{-1} - I \right] \right)^{n} D (D - L)^{-1} \mathbf{J}_0 \qquad (4.37)$$

This transformation allows for faster computation of the currents at each iteration as several matrix multiplications are removed and the identity subtraction is a computationally simple operation. Note that, if working right to left, the currents at the end of each iteration exist in the computation after performing the inversion of $D - U$, but prior to multiplying by D and subtracting I. The solution of the MFIE as presented by (4.37) was implemented in C++ to compute the results shown in Chapter 8.

4.4   Conclusion

This chapter has derived the tools necessary to compute the numerical solution of the surface currents which is needed to solve the general 2-D large surface scattering problem. Beginning with the basic equivalence principle of electromagnetics, the magnetic field integral equation has been derived. The MFIE describes the currents present at the surface of a perfectly conducting body in the presence of an incident electromagnetic field. The method of moments was then used to discretize the MFIE, and the resulting kernel integrals were solved to produce the matrix needed for a numerical solution. Finally, the method of ordered multiple interactions was derived as a technique for solving large matrix forms of the MOM version of the MFIE. MOMI, as represented by equation (4.37) is implemented as the solution technique for the MFIE that is used for the remainder of this work.

Chapter 5

Error Bound on Truncation of Flat Surface Integration

The goal of this thesis is to develop a method to determine the error which is inherent in propagation modeling because topographical data is discretized with large sampling sizes. Therefore, the errors which will occur in the computation should be characterized. One of the errors which has an unknown effect is the result of truncating the integration surface. Because of the nature of the computations which will be carried out, it would be impossible to continue the surface out to infinity, and impractical to extend it far beyond the observation point. This chapter develops a bound on the error caused by the truncation of the integration surface. This bound is, however, too loose to be practical.

For a line source above a planar perfect electric conductor, the exact solution is known

through image theory [7]. This makes the problem useful as a means of examining the order of the error due to the truncation of the surface when computing a numerical solution. Because the field, surface currents, and scattered field are all known exactly, error can be reduced entirely to the error due to truncation of the surface. The setup for determining the error is to place a line source over a PEC plane. Since the exact fields at the surface are known, the integral for the scattered field from the equivalent surface currents is developed. The scattered field integral will then be broken down into a central region which represents the propagation path, and the exterior region representing points beyond the propagation path.

Finally, an attempt is made to find a bound on the contributions of the exterior integrals. This bound will then be compared to actual truncation errors for the flat surface problem. While the bound will be shown to be sufficient for shorter propagation distances, it will not hold up well for longer paths.

5.1 Problem Setup

An infinite line source in the $\hat{\mathbf{y}}$ direction is located above an xy-oriented PEC plane. The normal to this surface is $\hat{\mathbf{z}}$, and the points of interest are:

- $\mathbf{r}$, the point in space at which the field is computed.

- $\mathbf{r}_s$, the location of the source.

- $\mathbf{r}_0$, a scattering point on the surface of the PEC.

Figure 5.1 illustrates these locations, along with a and b, the endpoints of the integration regions.
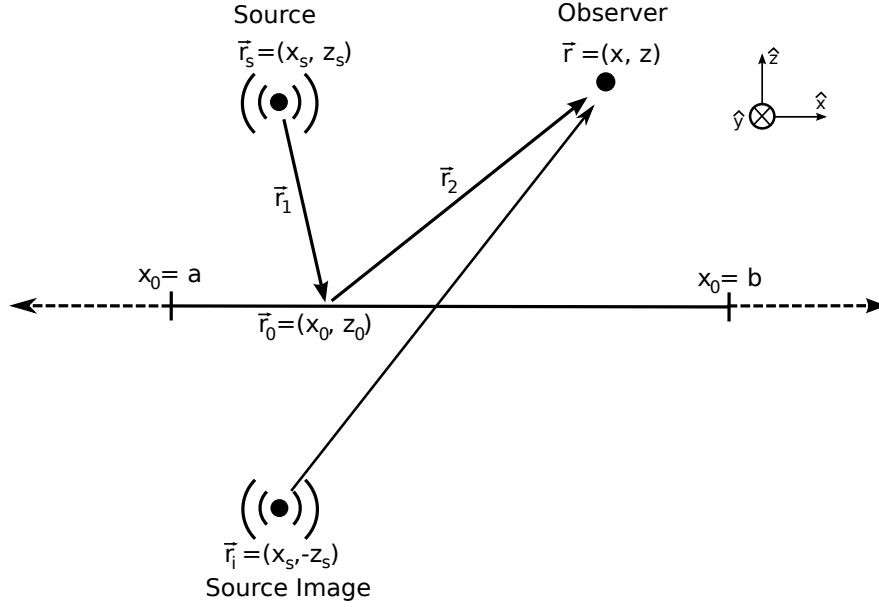
Figure 5.1: Coordinates for the truncated flat surface scattering problem.

From equations (B.2a) and (B.2b), the fields created by the source are, for TE incidence,

$$\mathbf{E}_i = -I_e \frac{k_0 \eta_0}{4} H_0^{(2)} \left(k_0 |\mathbf{r} - \mathbf{r}_s| \right) \hat{\mathbf{y}} \tag{5.1a}$$

$$\mathbf{H}_i = I_e \frac{k_0}{4j} H_1^{(2)} \left(k_0 |\mathbf{r} - \mathbf{r}_s| \right) \left[\frac{\mathbf{r} - \mathbf{r}_s}{|\mathbf{r} - \mathbf{r}_s|} \times \hat{\mathbf{y}} \right] \tag{5.1b}$$

and from (B.3a) and (B.3b) for TM incidence

$$\mathbf{E}_i = -I_m \frac{k_0}{4j} H_1^{(2)} \left(k_0 |\mathbf{r} - \mathbf{r}_s| \right) \left[\frac{\mathbf{r} - \mathbf{r}_s}{|\mathbf{r} - \mathbf{r}_s|} \times \hat{\mathbf{y}} \right] \tag{5.2a}$$

$$\mathbf{H}_i = -I_m \frac{k_0}{4\eta_0} H_0^{(2)} \left(k_0 |\mathbf{r} - \mathbf{r}_s| \right) \hat{\mathbf{y}} \tag{5.2b}$$

As mentioned in Chapter 4, the tangential electric field is driven to zero by the PEC, and this results in total reflection of the incident field [7]. The result is a doubling of the magnetic field at the surface. That is, at the surface, $\mathbf{H} = 2\mathbf{H}_i$ and $\mathbf{E} = 0$. Thus, the current along the flat PEC surface, equal to $\mathbf{J^s} = 2\hat{\mathbf{n}} \times \mathbf{H}_i$ is

$$\mathbf{J}_{TE}^s(\mathbf{r}_0) = I_e \frac{k_0}{2j} H_1^{(2)}(k_0 r_1)(-\hat{\mathbf{x}} \cdot \hat{\boldsymbol{r}}_1)\,\hat{\mathbf{y}} \tag{5.3}$$

$$\mathbf{J}_{TM}^s(\mathbf{r}_0) = I_m \frac{k_0}{2\eta_0} H_0^{(2)}(k_0 r_1)\,\hat{\mathbf{x}} \tag{5.4}$$

The vector $\mathbf{r}_1$ is defined to be $\mathbf{r}_0 - \mathbf{r}_s$, the vector from the source to a point on the surface.

5.2   Truncation of the Scattering Integral

Using equations (3.36a), (3.36b), (3.37a) and (3.37b), the scattered fields can be computed from these currents. The process for the magnetic component of the TM fields follows. Equations (3.37a) and (3.36b) are shown again below for convenience. The scattering integrals will then be truncated, and a bound placed on the truncation effects.

$$
\begin{aligned}
\mathbf{E}_{TM}^s(\mathbf{r}) = -\frac{\eta_0 k_0}{4} \int_{S_0} &\left[\hat{\boldsymbol{\beta}}(\hat{\boldsymbol{\beta}} \cdot \hat{\mathbf{s}}_0)\left(H_0^{(2)}(k_0 r_2) - \frac{H_1^{(2)}(k_0 r_2)}{k_0 r_2}\right)\right.\\
&\left. +\hat{\boldsymbol{r}}_2(\hat{\boldsymbol{r}}_2 \cdot \hat{\mathbf{s}}_0)\frac{H_1^{(2)}(k_0 r_2)}{k_0 r_2}\right] J^s(\mathbf{r}_0)\mathrm{d}s_0
\end{aligned}
\tag{5.5}
$$

$$\mathbf{H}_{TM}^s(\mathbf{r}) = \hat{\mathbf{y}}\frac{k_0}{4j} \int_{S_0} (\hat{\boldsymbol{\beta}} \cdot \hat{\mathbf{s}}_0)H_1^{(2)}(k_0 r_2)J^s(\mathbf{r}_0)\mathrm{d}s_0 \tag{5.6}$$

The vector $\mathbf{r}_2$ is defined to be $\mathbf{r} - \mathbf{r}_0$, the vector from a point on the surface to a point in space, and $\boldsymbol{\beta} = \hat{\mathbf{y}} \times \mathbf{r}_2$ is a vector tangential to $\mathbf{r}_2$ in the x-z plane.

Combining (5.4) with (3.37a) and (3.37b) yields:

$$
\mathbf{E}_{TM}^{s}(\mathbf{r}) = -\frac{k_0^2}{8} I_m \int_{S_0} \left[\hat{\boldsymbol{\beta}}(\hat{\boldsymbol{\beta}} \cdot \hat{\mathbf{s}}_0) \left(H_0^{(2)}(k_0 r_2) - \frac{H_1^{(2)}(k_0 r_2)}{k_0 r_2} \right) \right.
$$
$$
\left. + \hat{\boldsymbol{r}}_2(\hat{\boldsymbol{r}}_2 \cdot \hat{\mathbf{s}}_0)\frac{H_1^{(2)}(k_0 r_2)}{k_0 r_2} \right] \left[H_0^{(2)}(k_0 r_1) \right] \mathrm{d}s_0
\tag{5.7}
$$

$$
\mathbf{H}_{TM}^{s}(\mathbf{r}) = \hat{\mathbf{y}}\frac{k_0^2}{8 j \eta_0} I_m \int_{S_0} (\hat{\boldsymbol{\beta}} \cdot \hat{\mathbf{s}}_0) H_1^{(2)}(k_0 r_2) H_0^{(2)}(k_0 r_1) \mathrm{d}s_0
\tag{5.8}
$$

By substituting in the surface values, the above dot products can be evaluated. Note that the surface is located at $z_0 = 0$. For (5.8), the result is:

$$
\mathbf{H}_{TM}^{s}(\mathbf{r}) = \hat{\mathbf{y}}\frac{k_0^2}{j 8 \eta_0} I_m \int_{-\infty}^{\infty} \frac{z}{r_2} H_1^{(2)}(k_0 r_2) H_0^{(2)}(k_0 r_1) \mathrm{d}x_0
$$

To perform a numerical integration the surface is truncated. Call the left endpoint $x_0 = a$ and the right endpoint $x_0 = b$. The error free scattered field is given as a summation of three integrals.

$$
\mathbf{H}_{TM}^{s}(\mathbf{r}) = \hat{\mathbf{y}}\frac{k_0^2 I_m}{j 8 \eta_0} [I_1 + I_2 + I_3]
\tag{5.9}
$$

$$
I_1 = \int_{-\infty}^{a} \frac{z}{r_2} H_1^{(2)}(k_0 r_2) H_0^{(2)}(k_0 r_1) \mathrm{d}x_0
\tag{5.10a}
$$

$$
I_2 = \int_{a}^{b} \frac{z}{r_2} H_1^{(2)}(k_0 r_2) H_0^{(2)}(k_0 r_1) \mathrm{d}x_0
\tag{5.10b}
$$

$$
I_3 = \int_{b}^{\infty} \frac{z}{r_2} H_1^{(2)}(k_0 r_2) H_0^{(2)}(k_0 r_1) \mathrm{d}x_0
\tag{5.10c}
$$

5.2.1   The TM Bound

These three integrals can be broken down into the numerical integration for the solution and the corresponding error. The middle term of the integration, I_2, is the term that will

eventually be computed numerically. The outer regions, I_1 and I_3, represent the values in the field which are lost due to that truncation, and are thus the error terms.

$$\mathbf{H}_{TM}^s(\mathbf{r}) \simeq \hat{\mathbf{y}} \frac{k_0^2}{j8\eta_0} I_m I_2 \tag{5.11}$$

$$er_{H_{TM}}(\mathbf{r}) = \hat{\mathbf{y}} \frac{k_0^2}{j8\eta_0} I_m [I_1 + I_3] \tag{5.12}$$

Since (5.10a) and (5.10c) have the same integrand but differing limits, (5.10a) will be the focus. Without loss of generality, it is assumed that $a < x_s < x < b$. Also, assuming that the source and receive points are sufficiently inside the edge locations, the large argument approximations for the Hankel functions may be used [6].

$$I_1 \simeq \int_{-\infty}^a \frac{z}{r_2} \left(\frac{2j}{\pi k_0 r_2} \right)^{\frac{1}{2}} je^{-jk_0 r_2} \left(\frac{2j}{\pi k_0 r_1} \right)^{\frac{1}{2}} e^{-jk_0 r_1} \mathrm{d}x_0$$

$$I_1 \simeq -\frac{2}{\pi k_0} \int_{-\infty}^a \frac{ze^{-jk_0(r_1+r_2)}}{\left[(x-x_0)^2 + z^2 \right]^{\frac{3}{4}} \left[(x_0-x_s)^2 + z_s^2 \right]^{\frac{1}{4}}} \mathrm{d}x_0 \tag{5.13}$$

For purposes of determining error, the magnitude of I_1 will bound the error caused by the truncation of the left edge. Because the interest is a bound on I_1, the absolute value can be brought into the integral.

$$|I_1| \leq \frac{2}{\pi k_0} \int_{-\infty}^a \left| \frac{z}{\left[(x-x_0)^2 + z^2 \right]^{\frac{3}{4}} \left[(x_0-x_s)^2 + z_s^2 \right]^{\frac{1}{4}}} \right| \mathrm{d}x_0 \tag{5.14}$$

By noting that $\sqrt{(x-x_0)^2} \leq \sqrt{(x-x_0)^2 + z^2}$, and $(a-x_s)^2 + z_s^2 \leq (x_0-x_s)^2 + z_s^2$ over the entire integrand, these lesser values can be used in the bound in place of their more

complicated larger forms. The result is a simple integral of a rational function.

$$|I_1| \leq \frac{2}{\pi k_0} \int_{-\infty}^{a} \left| \frac{z}{|x - x_0|^{\frac{3}{2}} \left[(a - x_s)^2 + z_s^2 \right]^{\frac{1}{4}}} \right| dx_0 \tag{5.15}$$

$$|I_1| \leq \frac{z}{\pi k_0 \sqrt{x - a} \left[(x_s - a)^2 + z_s^2 \right]^{\frac{1}{4}}} \tag{5.16}$$

The identical process can be repeated for (5.10c) to determine that

$$|I_3| \leq \frac{z}{\pi k_0 \sqrt{b - x} \left[(x_s - b)^2 + z_s^2 \right]^{\frac{1}{4}}} \tag{5.17}$$

By combining these in (5.12) the result is a bound dependant on the location of the source and observation point, as well as the truncation points.

$$|er_{H_{TM}}(\mathbf{r})| \leq \frac{k_0 z I_m}{8 \pi \eta_0} \left[\frac{1}{\sqrt{x - a} \left[(x_s - a)^2 + z_s^2 \right]^{\frac{1}{4}}} + \frac{1}{\sqrt{b - x} \left[(x_s - b)^2 + z_s^2 \right]^{\frac{1}{4}}} \right] \tag{5.18}$$

Because an exact solution for the scattered field is known, this bound can be put in terms of a ratio of error to that solution. The image theory solution for the scattered field is the field produced by a line source at the image point $\mathbf{r}_i = (x_s, -z_s)$. The large argument form of the Hankel function can be used here as well.

$$\mathbf{H}_{TM}^{s}(\mathbf{r}) = -I_m \frac{k_0}{4\eta_0} H_0^{(2)} (k_0 |\mathbf{r} - \mathbf{r}_i|) \, \hat{\mathbf{y}} \tag{5.19}$$

$$|\mathbf{H}_{TM}^{s}(\mathbf{r})| \simeq \frac{k_0 I_m}{4\eta_0} \sqrt{\frac{2}{\pi k_0 \sqrt{(x - x_s)^2 + (z + z_s)^2}}} \tag{5.20}$$

Combining (5.18) and (5.20) defines this error ratio. At the same time, k_0 can be replaced by $2\pi/\lambda_0$. The result shows that the elevation over the surface is proportional to the error. The slope of this error is the mean of the ratios resulting from the left edge and the right

edge.

$$\frac{|er_{H_{TM}}(\mathbf{r})|}{\mathbf{H}^s_{TM}(\mathbf{r})} \leq \frac{z}{2\sqrt{\lambda_0}} \left[\frac{[(x-x_s)^2 + (z+z_s)^2]^{\frac{1}{4}}}{\sqrt{x-a}\,[(x_s-a)^2 + z_s^2]^{\frac{1}{4}}} + \frac{[(x-x_s)^2 + (z+z_s)^2]^{\frac{1}{4}}}{\sqrt{b-x}\,[(x_s-b)^2 + z_s^2]^{\frac{1}{4}}} \right] \tag{5.21}$$

This can be further simplified if the assumption is that the transmitter and receiver are located far apart and relatively near to their respective edges. In that case, the root of the distance between source and receiver is nearly equal to that between the receiver and its most distant edge.

$$\left[(x-x_s)^2 + (z-z_s)^2\right]^{1/4} \simeq \sqrt{x-a}$$

Likewise, the same can be applied to the distance from the source to its most distant edge.

$$\left[(x-x_s)^2 + (z-z_s)^2\right]^{1/4} \simeq \left[(x_s-b)^2 + z_s^2\right]^{1/4}$$

Thus those ratios can be considered to be one. Also, by replacing $\sqrt{\lambda_0} = \lambda_0/\sqrt{\lambda_0}$, the expression can be displayed entirely in the form of distances in wavelengths.

$$\frac{|er_{H_{TM}}(\mathbf{r})|}{\mathbf{H}^s_{TM}(\mathbf{r})} \leq \frac{z}{2\lambda_0} \left[\frac{\sqrt{\lambda_0}}{[(x_s-a)^2 + z_s^2]^{\frac{1}{4}}} + \frac{\sqrt{\lambda_0}}{\sqrt{b-x}} \right] \tag{5.22}$$

Finally, by dropping the z component of the remaining distance, a simple expression which shows that the error is proportional to the observation height and inversely proportional to the square root of the distances in from the edge of the source and the receiver.

$$\frac{|er_{H_{TM}}(\mathbf{r})|}{\mathbf{H}^s_{TM}(\mathbf{r})} \leq \frac{z}{2\lambda_0} \left[\sqrt{\frac{\lambda_0}{x_s-a}} + \sqrt{\frac{\lambda_0}{b-x}} \right] \tag{5.23}$$

5.2.2   The TE Bound

Repeating the process for a TE source produces a very similar result. In the TE case, however, the bound increases as the source comes off of the surface instead of as the observer elevates. This can be seen in (5.24) the TE counterpart to (5.21).

$$\frac{|er_{E_{TE}}(\mathbf{r})|}{\mathbf{E}^s_{TE}(\mathbf{r})} \leq \frac{z_s}{2\sqrt{\lambda_0}}\left[\frac{[(x-x_s)^2+(z+z_s)^2]^{\frac{1}{4}}}{\sqrt{x_s-a}\,[(x-a)^2+z^2]^{\frac{1}{4}}} + \frac{[(x-x_s)^2+(z+z_s)^2]^{\frac{1}{4}}}{\sqrt{b-x_s}\,[(x-b)^2+z^2]^{\frac{1}{4}}}\right] \tag{5.24}$$

This is even more true in the simplified form of (5.25), which corresponds to (5.23).

$$\frac{|er_{E_{TE}}(\mathbf{r})|}{\mathbf{E}^s_{TE}(\mathbf{r})} \leq \frac{z_s}{2\lambda_0}\left[\sqrt{\frac{\lambda_0}{x_s-a}} + \sqrt{\frac{\lambda_0}{b-x}}\right] \tag{5.25}$$

The results show that in both TE and TM cases, keeping the transmitter and receiver elevations low relative to the distance away from the truncated edge will limit the effects of the surface truncation.

5.3   The Bound and Actual Errors

The above bound has a simple form which is easy to understand. However, the accuracy of the bound must still be examined. Because the bound disregarded the phase of the integral, it is assumed that the bound will greatly exceed the actual error. In all the plots which follow, the plotted bound is (5.21) in the TM case and (5.24) in the TE case. The actual error can be computed for test cases by numerically integrating the truncated integral I_2, (5.10b), and comparing it to the image theory result.

(a) $z = \lambda_0$

(b) $z = 5\lambda_0$

(c) $z = 10\lambda_0$
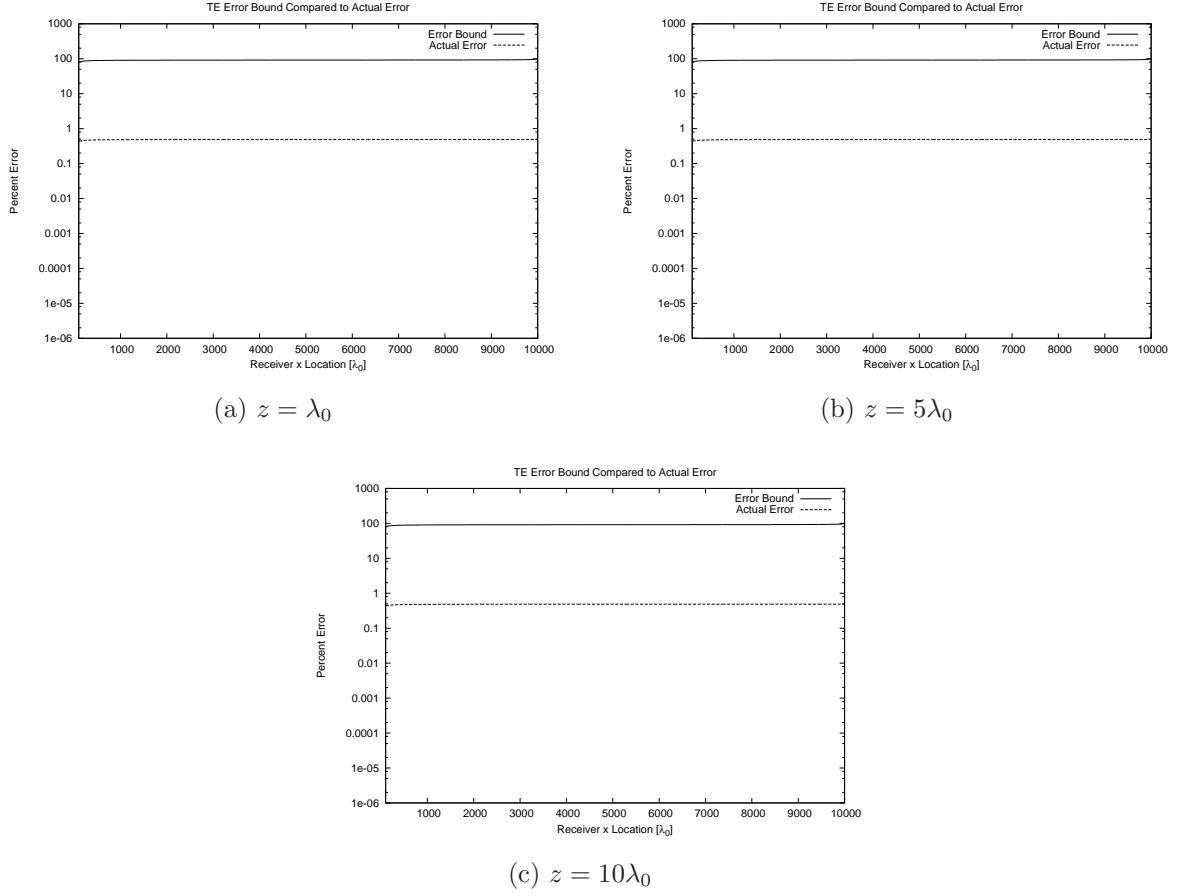
Figure 5.2: Error as a function of distance from the source compared to the bound for a TE source over a flat surface with fixed endpoints. ($a = -30\lambda_0$, $b = 10030\lambda_0$, $x_s = 0$, $z_s = 10\lambda_0$)

Figure 5.2 shows the comparison of the error bound to the actual error between the numerically scattered field and the theoretical values. All six figures show the results for an observation point moving horizontally at a fixed height above the surface. In these comparisons, the surface and source are fixed, while the observation point is moving. In all these cases, a line source is placed 10 wavelengths above the surface, and the surface extends 30 wavelengths to the left of the source. Also, in all cases, the surface ends 10,030 wavelengths to the right of the source. Put another way, the surface is 10,060 wavelengths long, and $x_s - a = 30\lambda_o$.

Figure 5.2a illustrates the TE case with the observation height fixed one wavelength above the surface. Figure 5.2b is an identical case but with the observation height five wavelengths above the surface. Figure 5.2c is likewise identical except for the ten wavelength observation height. These figures show that the developed error bound should keep the error below 100%, which is certainly too high a level compared to the actual error. The actual error is below 1% for all three figures. As (5.25) indicates, the error in the TE case should not be too sensitive to the observation height, and, indeed, the plots look nearly identical.

Figure 5.3 shows the same results for the TM case with one wavelength, five wavelength, and ten wavelength heights above the surface, respectively. Equation (5.23) suggests that the TM case should be more sensitive to the observation height, and that is indeed the case, for both the bound and the actual error. The developed bound is between 10% and 100%, dependent on the height, while the actual error is two orders of magnitude or more below the bound.

(a) $z = \lambda_0$

(b) $z = 5\lambda_0$

(c) $z = 10\lambda_0$
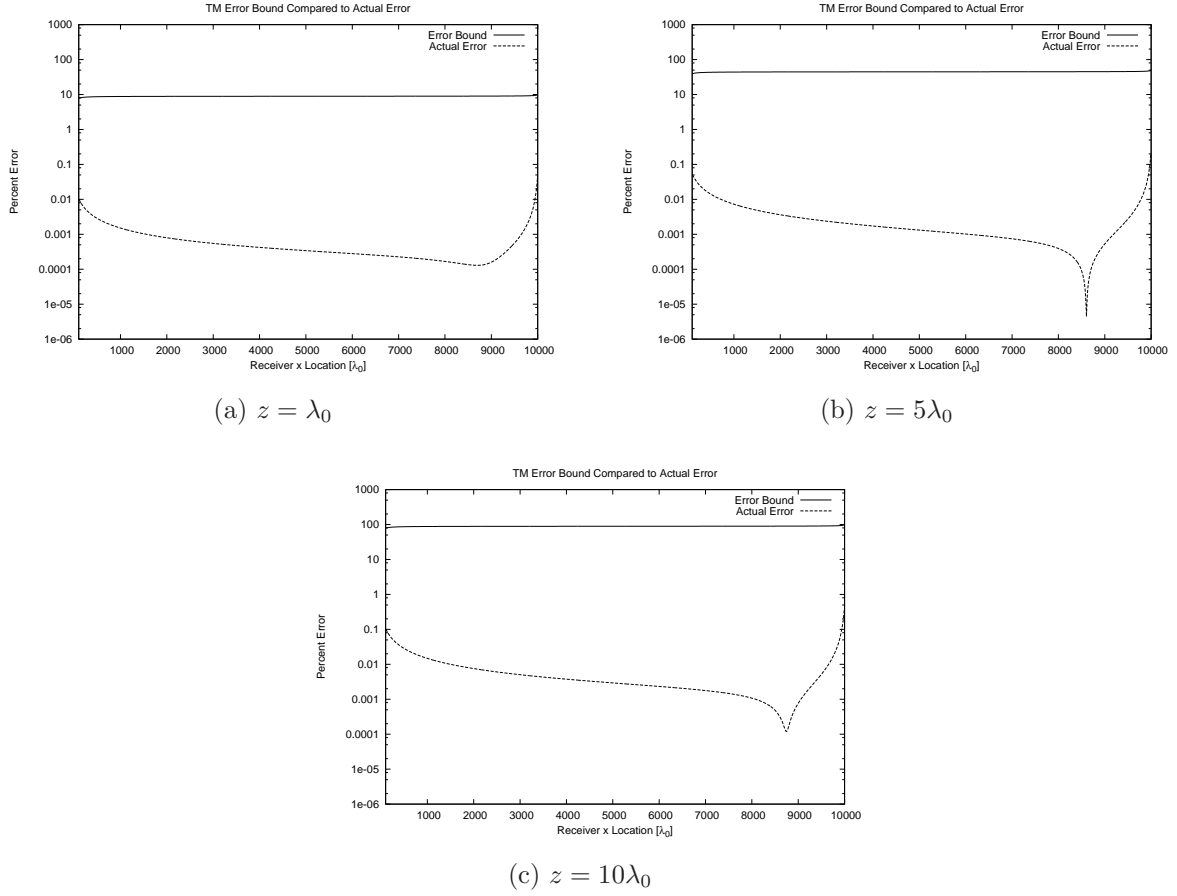
Figure 5.3: Error as a function of distance from the source compared to the bound for a TM source over a flat surface with fixed endpoints. ($a = -30\lambda_0$, $b = 10030\lambda_0$, $x_s = 0$, $z_s = 10\lambda_0$)

(a) TE

(b) TM
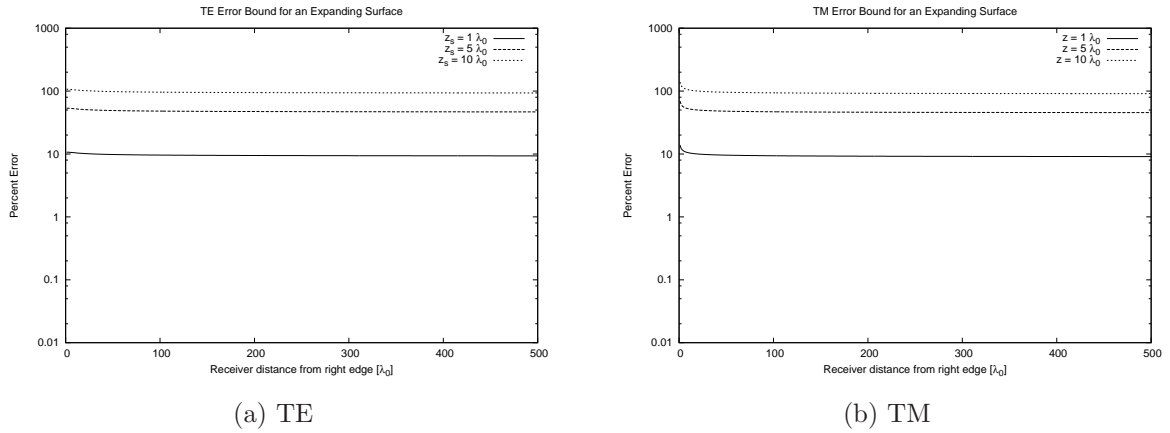
Figure 5.4: Error bound as the right edge of the surface moves away from the observation point, for a fixed source at a fixed observation distance over a flat surface. ($a = -30\lambda_0$, $x_s = 0$, $x = 10000\lambda_0$, $z = 10\lambda_0$)

Figures 5.4a and 5.4b show how the error bound changes as the surface expands, for the TE and TM cases, respectively. In both cases, the source location, observation location, and left edge of the surface are fixed. The plots show how the error is reduced as the right edge of the surface extends out past the observation point. In all cases, the source is located above the origin, and the surface extends thirty wavelengths to the left of the source. The observation point in these cases is always located above $x = 10,000\lambda_o$.

Because equation (5.25) indicates sensitivity to the source height, Figure 5.4a shows the bound for three different source heights, while the observation point is fixed ten wavelengths above the surface. Similarly, because the TM case is sensitive to observer height, Figure 5.4b plots three different receiver heights with a fixed source height of ten wavelengths. Both the TE and TM bounds are similar, with only a more dramatic increase in the TM bound as the surface approaches the point of observation.

(a) TE   (b) TM
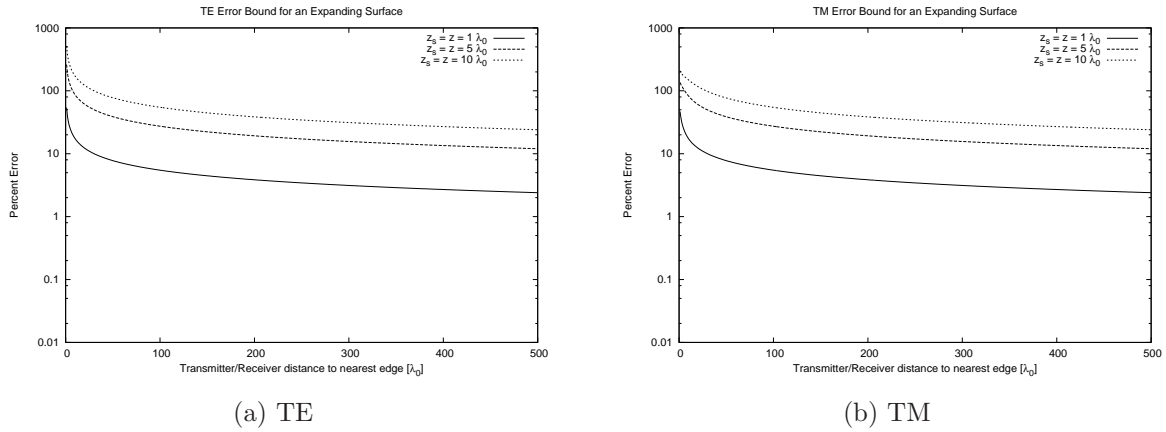
Figure 5.5: Error bound as both edges of the surface expand symmetrically, for three TM source/observation height pairs at a fixed observation distance over a flat surface. ($x_s = 0$, $x = 10000\lambda_0$)

Similar to those discussed above, Figures 5.5a and 5.5b show how the error bound changes

as the surface expands. However, in this case, both the left and right edges of the surface are expanding out symmetrically. Figure 5.5a shows the TE bound and Figure 5.5b the TM. In these plots, the distance between the source and observation point is again fixed at 10,000 wavelengths. In both plots, the three lines represent raising both the source and observation points one, five, and ten wavelengths off the surface.

Comparing Figure 5.5a to 5.4a shows, as should be expected, that extending both edges of the surface instead of just a single edge has a dramatic effect on the error bound. Likewise, Figures 5.5b to 5.4b display the same results for the TM case.

5.4   Conclusions

The equivalence principal on which MOMI is based expects the problem space to be either completely bounded, or extend out to infinity. However, MOMI can not reasonably perform computations out to infinity. Nor can the space be completely bounded for a propagation problem. Also, propagation models tend not to provide path data for points outside the transmitter to receiver path. The result is that integration must be truncated while the edges are still illuminated.

Therefore, this section sought to develop an error bound for the effects of truncating the scattering integral. This bound was created for the case of a line source over a flat surface, in both TE and TM cases. The equivalent currents for a line source over a flat surface were used as the base currents for the scattered field. These currents should scatter to produce

the same field predicted by image theory. A bound to the finite integral was developed by bounding the magnitude of the discarded portions of the integral.

A relatively simplistic form of the relative error bound is possible, taking the form of (5.23) for the TM case and (5.25) for the TE case. However, a comparison of the bound to the actual error shows that the bound, as should be expected, grossly overstates the error. That does not, however, make the bound useless. The bound does indicate, and the plots of actual error likewise show, that the surface should extend somewhat beyond the transmitter and the receiver locations. This will need to be applied in Chapter 6, where the path data only exists starting at the transmitter location and ending at the receiver location.

Chapter 6

Rough Surface Generation and Path Loss Computation

Previous chapters have described the background of radio propagation and the solution of the scattering problem and computation of the fields present over the surface. This chapter covers the techniques used to compute path loss over a terrain profile using those tools. First, the structure of the computation of path loss using MOMI is described. Then, a technique is developed for generating the semi-random surfaces which pass through known points obtained from a topographical database, but are random between the sampled data. Following that is a description of the computation of path loss from the source and scattered fields. The chapter concludes with a brief overview of the Hata path loss model, which will be used for comparison purposes.

One of the key issues in predicting loss over mapped terrain is that the mapping is incomplete. All surfaces used in predictions are mapped to a certain level of precision. Often the map data is tabulated in a computer based on a specific grid, such as sampling every thirty or one hundred meters. To estimate the effect that this sampling has on the predictions, this work takes several paths sampled at a thirty meter frequency. Those data points are fitted to a spline and the spline surface is added to a random surface. The resulting surfaces fit the underlying data but are randomly connected. After the surfaces are generated, the scattering from the semi-random surfaces is computed using the techniques of Chapters 3 and 4. Then the path Loss due to the terrain is computed from the scattering results.

Path loss was defined by Friis to encompass the power spread over a spherical wavefront in free space [82]. Using his definition, an equivalent term including the terrain loss effects is developed. Also discussed is the necessary conversion between the results of the two dimensional computations and the three dimensional power spread of a real system. This conversion is developed from the examination of the communication link equation in two dimensions and in three dimensions.

Lastly, the Hata model is summarized so that it can be used for comparison to the MOMI results. The rural Hata propagation model was chosen for comparison because it was developed in forested, mountainous terrain [71]. The propagation paths which are examined later are rural mountainous paths. This will conclude the development of the tools needed to evaluate the accuracy path loss computations due to the sparsity of topographical

information.

6.1   Combination of Monte-Carlo Techniques and Path Loss Computations

This thesis seeks to examine how the uncertainties in the terrain data may affect the path loss predictions. These uncertainties would have some effect on any of the above mentioned theoretical models. Because the goal of this study is to examine the uncertainties introduced by this undersampling, it is necessary to use a prediction technique which is as accurate as possible. Following the work of Hufford, Ott, Berry, Janaswamy, and Fernandez, a two dimensional integral equation approach is used [84, 86, 87, 95, 96, 99]. The method used here, applying the method of ordered multiple interactions (MOMI) to the solution of the magnetic field integral equation (MFIE) [9], presented in chapter 4, includes fewer assumptions about the propagating wave than the above mentioned integral equation approaches.

By combining the Monte-Carlo techniques described below with the electromagnetic solution techniques presented in subsequent chapters, the goal is to examine the uncertainty of the path loss predictions introduced by the sampled terrain data. The total method can be summarized as follows.

1. Fit a spline to the surface data for the intended path.

2. The spline is then stored and a randomly rough surface is generated and added to

the spline surface with the modulation of (6.8), forming a single surface realization which matches the original sparsely sampled surface data and enhances the roughness spectrum beyond the original data.

3. MOMI is used to solve for the equivalent currents induced at the surface by an electric (TE) or magnetic (TM) line source located at the desired source location.

4. The currents are used to compute the scattered field, which is added to the incident field, at the desired observation points.

5. The fields at the observation points, and the power radiated, are used to compute the path loss for this realization.

6. Steps 2 through 5 are repeated with new randomly rough surfaces used each time.

7. Statistics are computed for the path loss data, including mean and variance.

This method allows the accumulation of statistics for path loss for many surfaces which could conceivably fit the underlying map data. These statistics should rely in part on the map data and in part on the assumed roughness spectrum with which it is augmented. Following chapters will show examples of this technique and some of the results which can be obtained from it.

6.2   Generation of Monte-Carlo Surfaces

True terrain has variations which occur at all scales, from the gross scale of topographic maps, down to the scale of rocks along the ground. Because map data and specifically computerized topographic data ignore the finer scales of the terrain, it is not possible to simply disregard some levels of data to determine the level of accuracy. No existing techniques were found for providing random connections between known points. Instead, it was necessary to develop a method of fitting multiple surfaces to predefined terrain data. These multiple surfaces represent a set of possible connections of the terrain path. However, it is assumed that the mean path is generally smoothly fit along the data points, so to account for this a spline fit of the true map data is used as the basis for the underlying mean surface over which rough surfaces will be added. Ogilvy covers the generation of randomly rough surfaces from a known roughness spectrum [4], and that method is used here for generating a base randomly rough surface. Additionally, a cubic spline can be used to fit a curve with a continuous second derivative to the known topographic data [126]. Thus, the total surface for the i'th realization, $\zeta^{[i]}(x)$ is the sum of a spline surface, $\zeta_S(x)$, and a modulated randomly rough surface, $\zeta_{rm}^{[i]}(x)$.

$$\zeta^{[i]}(x) = \zeta_s(x) + \zeta_{rm}^{[i]}(x) \tag{6.1}$$

6.2.1   The Spline Surface

The spline surface is a natural cubic spline fit of thirty meter surface data from the US Geo-
logical Survey's National Elevation Dataset [3]. A cubic spline is chosen because it provides
a surface which fits the data and provides continuous first and second derivatives [126]. The
following describes how the spline surface is generated from the map data.

For a set of M+1 known data points, the spline is a sum of M cubic polynomials, $S_m(x)$,
which have been defined to fit so that the values of the m'th polynomial match the thirty
meter data at locations x_m and x_{m+1}, and so that the first and second derivatives of the
cubics are continuous across those points. Let the known points be $f(x_m)$.

$$\zeta_s(x) = S_m(x) \text{ where } x_m \leq x \leq x_{m+1} \tag{6.2}$$

$$S_m(x) = f(x_m) + s_m(x - x_m) + A_m(x - x_m)^2 + B_m(x - x_m)^2(x - x_{m+1})$$

$$\text{for } x_m \leq x < x_m + 1 \tag{6.3}$$

The condition that $S_m(x_m) = f(x_m)$ is clear from the above equation. Also, the value
$S'_m(x_m) = s_m$ is the derivative at x_m. Then, to allow $S_m(x_{m+1}) = f(x_{m+1})$, and $S_m(x_{m+1}) = s_{m+1}$ the values of A_m and B_m must be given by the following.

$$A_m = \frac{f(x_{m+1}) - f(x_m) - s_m h_m}{h_m^2} \tag{6.4}$$

$$B_m = \frac{s_{m+1} - s_m - 2A_m h_m}{h_m^2} \tag{6.5}$$

where $h_m = x_{m+1} - x_m$. This form gives each cubic in terms of the two known end points
and the derivatives at the endpoints. What is left then is to determine the values of the first

derivative, s_m, which produce a continuous second derivative at the joints. This condition is

satisfied by s_m which fit

$$h_m s_{m-1} + 2(h_{m-1} + h_m)s_m + h_{m-1}s_{m+1} = \beta_m$$

$$\beta_m = 3h_m \frac{f(x_m) - f(x_{m-1})}{h_{m-1}} + 3h_{m-1} \frac{f(x_{m+1}) - f(x_m)}{h_m}, \text{ m} = 2, 3, ..., \text{M}$$

(6.6)

Thus, for M+1 points with M-1 joints between the cubics, this provides a set of M-2

equations (shown above) and M unknowns, the values of s_m. Many methods are available

for choosing the remaining two equations, but the choice used here is to numerically estimate

the first derivative at the endpoints.

$$s_1 = \frac{f(x_2) - f(x_1)}{x_2 - x_1}$$

$$s_{M+1} = \frac{f(x_{M+1}) - f(x_M)}{x_{M+1} - x_M}$$

This system of equations is solved for the coefficients, and the resulting spline is used as the

mean surface.

6.2.2   The Random Surface

The random surface, ζ_r, is a randomly generated zero-mean surface with a flat power spec-

tral density (PSD). The surface is created as a sum of sines and cosines with frequencies

spaced evenly through the spectrum. The amplitudes, A_p and B_p, are zero mean Gaussian

random variables with a variance equivalent to the desired spectral power at the p'th sample

frequency, f_p.

$$\zeta_r(x) = \sum_{p=1}^{P} \left[A_p \sin(2\pi f_p x) + B_p \cos(2\pi f_p x) \right] \sqrt{\Delta f_p} \tag{6.7}$$

The power contained in each frequency is $(A_p^2/2 + B_p^2/2)\Delta f_p$, which should match the desired spectrum over many realizations [4].

These random surfaces are then modulated so that they go to zero at the known surface points. This allows the resulting total surface to match the known data. The random surface is modulated by a scaled quadratic with zeros at the consecutive known points and maximum value of one at the center of the interval.

$$\zeta_{rm}(x) = \zeta_r(x) \left[\frac{4(x - x_m)(x_{m+1} - x)}{(x_{m+1} - x_m)^2} \right] \tag{6.8}$$

(a) Original randomly rough surfaces   (b) Modulated randomly rough surfaces
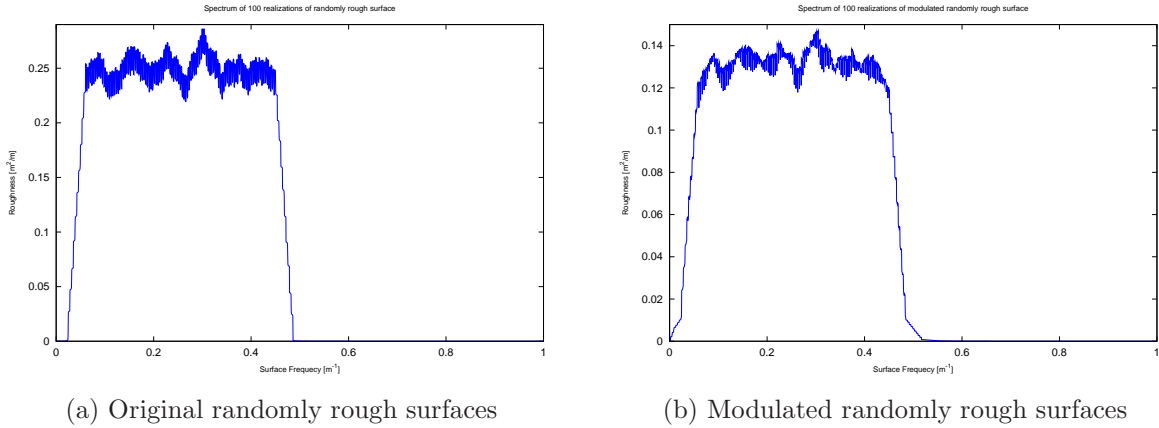
Figure 6.1: Spectrum for 100 randomly rough surfaces based on a flat spectrum.

Then the total surface, as mentioned in equation (6.1), has the mean value of the spline surface, and the added roughness of the modulated rough surface. Furthermore, it satisfies the necessary property of passing through every point which is known a-priori. Figure 6.1a

shows the sample spectrum of one hundred realizations of the non-modulated rough surface, and Figure 6.1b shows the spectrum of the modulated surface

6.3   Path Loss and the 2D to 3D Conversion

Path loss, as used for this work, is the loss attributed to both free space wave spreading and terrain scattering. It is the ratio of the power present in the fields at a given location divided by the total power radiated. The transmitted power is a function of current. The power in the field is represented by the Poynting vector. After computing the path loss as represented by the two dimensional system, a spreading factor is added to convert to the predicted loss in a three dimensional system.

Path loss is a term which was developed for the link equation to represent the loss due to power spreading. In three dimensions, the Friis transmission equation represents received power in terms of the transmitted power, P_t; the effective areas of the transmitting and receiving antennas, A_t and A_r; the distance between the antennas, r; and the electromagnetic wavelength λ [82].

$$P_r = P_t \frac{A_t A_r}{\lambda^2 r^2} \tag{6.9}$$

Antenna theory likewise has a well established identity relating the quantities of effective area, A, and antenna gain, G [127].

$$A = \frac{G\lambda^2}{4\pi} \tag{6.10}$$

Combining the above two equations, and keeping the subscripts t for the transmitter and r for the receiver, produces the following form.

$$P_r = P_t G_t G_r \frac{\lambda^2}{(4\pi r)^2} \tag{6.11}$$

Free space path loss is then defined to encompass the remaining fractional term of the link equation.

$$L_p = \frac{(4\pi r)^2}{\lambda^2} \tag{6.12}$$

With all these terms accounted for, the received power for a free-space link can be predicted by knowing the frequency, transmitting power, antenna gains, and distance.

$$P_r = \frac{P_t G_t G_r}{L_p} \tag{6.13}$$

Utilizing the above equation, the definition of path loss that is used here-after is any loss occurring between the transmitter and receiver, and accounted for in (6.13) by the term L_p.

6.3.1   Computing Path Loss

Path loss has been previously defined as the loss in the link between a transmitter and receiver which is solely due to the propagation. Subsequent chapters will show how to solve the scattering problem in two dimensions and compute the electric and magnetic fields present at the receiver. However, the question arises, how are these fields used to compute a three dimensional value of path loss?

By examining the link equation again, and specifically looking at the link equation in two dimensions compared to three dimensions, as well as examining what different terms mean, this question can be answered. The first step in determining how to compute path loss is to determine what quantities are known from the two dimensional computations already described.

Inherent in the use of the line source is that $G_t = 1$. Likewise, the scattering computations described above provide the fields regardless of directionality, implying that $G_r = 1$. P_r and P_t are described below.

Power Density

The spatial power density present in a time harmonic field is represented by the cross product of the electric field and the complex conjugate of the magnetic field [7]. This quantity, the Poynting vector, has units of Watts per square meter in a three dimensional system, and Watts per meter in a two dimensional system. The real part represents the power travelling through an infinitesimal area which is perpendicular to the direction of the vector, while the imaginary part represents the power stored in, or oscillating around, the area.

$$\mathbf{S} = \mathbf{E} \times \mathbf{H}^* \tag{6.14}$$

The Poynting vector, $\mathbf{S}$, describes the power flow of the propagating wave, and is therefore what will be used as the basis of determining the path loss to the receiving location. The magnitude of the Poynting vector is the power density, S, and has units of Watts per square

meter. Then from this, and using the same technique from which path loss was developed, the received power is the power density integrated over the aperture of the receiving antenna. Assuming that the power density is constant over the effective area of the antenna, the received power is simply given by (6.15).

$$P_r = SA_r \tag{6.15}$$

Utilizing the above equivalence between effective area and gain, the received power can be expressed in terms of the antenna gain as well.

$$P_r = S\frac{G_r\lambda^2}{4\pi} \tag{6.16}$$

Finally, this form can be equated with (6.13) to obtain a form for path loss as a function of the power density.

$$L_p = \frac{4\pi P_t G_t}{\lambda^2 S} \tag{6.17}$$

The above equation is a form that can be used to obtain the path loss if the fields of the problem can be obtained.

Transmitted Power

The power radiated by the source is the reference value used in the path loss computation. This value is attained by integrating the Poynting Vector in a complete circle around the source at a distance of infinity, thus obtaining the power radiated out through the circle by

the source [7].

$$P_t = \lim_{\rho \to \infty} \int_0^{2\pi} \mathbf{S} \cdot \hat{\boldsymbol{\rho}} \rho \mathrm{d}\phi \tag{6.18}$$

This is done by combining (6.14) with (3.28a) and (3.28b), and integrating around the origin in ϕ. For the transverse electric case, this is given by (6.19)

$$P_t^{TE} = \lim_{\rho \to \infty} \int_0^{2\pi} -j\frac{I_e^2 k_0^2}{16\eta_0} H_0^{(2)}(k_0\rho) H_1^{(2)*}(k_0\rho) \hat{\boldsymbol{\rho}} \cdot \hat{\boldsymbol{\rho}} \rho \mathrm{d}\phi \tag{6.19}$$

Note that the dot product reduces to one, and there is no ϕ variation in the integrand. From Abramowitz and Stegun, the asymptotic form of the Hankel function is chosen for use as ρ approaches infinity [6].

$$H_\nu^{(2)}(z) \sim \sqrt{\frac{2}{\pi z}} e^{-j(z-\pi\nu/2-\pi/4)} \mathrm{as} z \to \infty$$

When included with (6.19), the conjugate forms of the exponential cancel, and the result for the TE case is given in (6.20).

$$P_t^{TE} = \frac{I_e^2 k_0^2}{4\eta_0} \tag{6.20}$$

To obtain the power transmitted by a TM line current, the same process can be carried out utilizing the fields from (3.29a) and (3.29b) for the TM case.

$$P_t^{TM} = \frac{I_m^2 k_0^2 \eta_0}{4} \tag{6.21}$$

Link Equation in Two Dimensions

The process in the prior section found a form for path loss for a three dimensional link given the power density present at a point in space. However, MOMI works in a two-dimensional

space, not a three dimensional space. By going through the process of developing a two-dimensional link equation, the correct conversion factor for the two dimensional to three dimensional path loss can be determined. In two dimensions, the power spread is not over a $4\pi r^2$ area sphere, but over a $2\pi r$ length line. The power density in free space should be the transmitted power $P_t G_t$, multiplied by a gain, and spreading over the circumference of a circle of distance r [82].

$$S = \frac{P_t G_t}{2\pi r} \tag{6.22}$$

Remembering that $P_r = SA_r$, and, as in the three dimensional case, converting aperture to gain using (6.10), provides a two dimensional form of the link equation.

$$P_r^{2D} = \frac{P_t^{2D} G_t G_r \lambda^2}{8\pi^2 r} \tag{6.23}$$

Just as the definition of free-space path loss is the collection of the remaining terms in the link equation, the two-dimensional link equation allows for the definition of a two dimensional equivalent to free space path loss L_p^{2D}.

$$L_p^{2D} = \frac{\lambda^2}{8\pi^2 r} \tag{6.24}$$

By taking a ratio of three dimensional free space path loss of (6.12), and two dimensional free space path loss, a conversion factor can be obtained.

$$L_p = L_p^{2D} \frac{1}{2r} \tag{6.25}$$

Alternately, if the fields computed from the two-dimensional problem are considered and the conversion factor is worked in to (6.17), a direct relationship can be obtained. What

is now known are the two gains G_t, G_r, the transmitted power per unit length P_t, and the power density at the receiver for the two dimensional problem S^{2D}. Therefore, the result is a three dimensional path loss directly from the two dimensional quantities via the following relationship.

$$L_p = \frac{P_t}{S^{2D}} \frac{8\pi r}{\lambda^2} \tag{6.26}$$

This quantity can be used in the link equation in place of free space path loss to account for path loss including terrain losses. By using it in this way, along with any upper and lower bounds determined from the statistical analysis which will be described later, better predictions of received power should be obtained. Most importantly, this allows for the comparison of this two dimensional method to existing three dimensional models and possibly to experimental data.

Finally, the results of loss will most often be presented in decibel form, with L_p^{dB} representing this result. The conversion between the two forms is show in equations (6.27) and (6.28).

$$L_p^{dB} = -10 \log_{10} (L_p) \tag{6.27}$$

$$L_p = 10^{\frac{-L_p^{dB}}{10}} \tag{6.28}$$

The negative sign in the conversion is purely to produce negative values of path loss when shown in dB for plotting. This produces results which are directly proportional to the power present at a location instead of inversely.

6.4   The Hata Model

As mentioned in Chapter 2, the Hata model was developed from empirical data to provide a rough guide to propagation loss. The model is developed in [71], and provides a single equation for loss based on distance, transmitter height, receiver height, and the choice of urban, suburban, or open terrain. The Hata model will be used in some cases for comparison to MOMI computations. The model is valid for frequencies between 150 and 1500 MHz, and from 1 to 20 km. The model provides an estimate of the median loss for the given parameters. The basic equation for loss in open terrain provided by Hata is

$$L_p = -69.55 - 26.16 \log_{10} f_c - 13.82 \log_{10} h_t - a(h_r)$$
$$+ (44.9 - 6.55 \log_{10} h_t) \log_{10} R - Q \text{ (dB)} \tag{6.29}$$

$$a(h_r) = 3.2(\log_{10} 11.75 h_r)^2 - 4.97 \text{ (dB)} \tag{6.30}$$

$$Q = 4.78 * (\log_{10} f_c)^2 - 18.33 * \log_{10} f_c + 40.94 \text{ (dB)} \tag{6.31}$$

Here, f_c is the frequency in megahertz, h_t is the height of the transmitter in meters, and h_r is the height of the receiver in meters, and R is the distance between the transmitter and the receiver in kilometers. The receiver height adjustment factor, $a(h_r)$, that is provided here, is for urban terrain with frequencies over 400 megahertz. The open terrain adjustment factor, Q, provides for the difference between urban areas and open areas. Together, these factors yield the estimate of path loss, L_p, in decibels. Note that while this model does not account at all for the specific terrain features, it is an efficient basic prediction tool.

6.5   Summary

This completes the development of the computational scheme used for computing a path loss prediction for a propagation path. As presented in this chapter, MOMI will be used to solve the fields over many randomly rough fits to the sparse topographic data of the path. The randomly rough surfaces combine an underlying cubic spline fit to the topographic data with a modulated zero-mean rough surface. The fields over each surface are used to compute the path loss over such a two dimensional surface. Each result is an estimate of possible path loss resulting from the propagation over a surface fitting the topographic data along the direct path between the transmitter and the receiver location. Subsequent chapters show the experimental measurements which have been made to validate the model, as well as the results of computations following this technique.

Chapter 7

Propagation Experiments for Model Validation

One difficulty with developing methods for computing terrain loss is validation of the models. Validating against experimental propagation data is an ideal means of testing, as it compares the model to real world measurements. This chapter presents experimental radio propagation measurements which were made in the vicinity of Green Bank, West Virginia. The goal of the measurement campaign was to provide sufficient point-to-point propagation data in mountainous environment to test the computations carried out in the next chapter.

Because the National Radio Astronomy Observatory (NRAO) in Green Bank, West Virginia, also needs to validate the model being used for the management of the National Radio Quiet Zone (NRQZ), the NRQZ was chosen as the location for obtaining the validation data.

NRAO is licensed to transmit for short times at whatever frequencies and power levels are required for their own scientific testing. Thus, by working with NRAO in the NRQZ, it was possible to quickly gain the necessary clearances to transmit at frequencies of interest and power levels sufficient to overcome the expected propagation losses. Additionally, the NRQZ provides low levels of interference, since the purpose of the quiet zone is to provide an interference free environment for radio astronomy.

Thus paths were chosen in the area around NRAO-Green Bank to provide a variety of environmental obstacles. Initial parameters of interest were to find a line-of-sight path, a near line-of-sight path, and a heavily obstructed path. A fixed reciever was located on the roof of the Jansky Lab (JL), while a mobile receiver would make measurements at several points between the transmitter and Jansky lab. Due to the mountainous terrain with limited roads, making numerous mobile measurements was deemed impractical. This is probably one reason why limited data exists for propagation in mountainous terrain. The Janksy Lab receiver site is located at 38 25' 52.82" North latitude by 79 49' 09.16" West longitude. The roof elevation as measured by Global Positioning System (GPS) is 844.7 meters above mean sea level (AMSL).

Four center frequencies were chosen for the experiment. Frequencies that were used were 904.15 MHz, 926.15 MHz, 1296.905 MHz, and 2303.15 MHz. These frequencies were chosen because of interest by NRAO for similarity to cellular and wireless internet frequencies. The setup provides a moderate set of data that can be used for validating propagation models in rough terrain.

A large number of propagation experiments were covered in Chapter 2. Prior to World War II, propagation experiments were limited to frequencies of 200 MHz and below [18–29]. Studies covering over-the-horizon transmission at higher frequecies were performed from the 1940s to the 1980s, focusing primarily on very long distance transmission for spatial separation of transmitters operating at similar frequencies [36–38, 40–42, 45–50, 56] . Other propagation experiments at the time either focussed on propagation in cities or line-of-sight propagation for microwave relays [43, 44, 51, 53, 54]. More recent tests have continued to focus on the effects of special cases such as foliage, propagation in coal mines, and propagation along urban streets [57, 59, 60, 63].

With the exception of work carried out by Dickson [45] and Hata [71], obstructed propagation in mountainous terrain has not been significantly measured. Hata's study was carried out in Japan, and was geared towards producing an area prediction model, with no attention paid to specific obstructions along a path. Thus, data has not been taken which can be used to validate a point-to-point model in mountainous terrain. Therefore, a propagation experiment was set up to take data which could be used to check the accuracy of the computations in the following Chapter.

7.1   Paths

The experiments were carried out in two stages. The first stage was a week of measurements made in August 2009 from two transmitter locations. The locations were chosen to provide

a line-of-sight path, a near line-of-sight path, and a heavily obstructed path. Following the analysis of that data, a decision was made to obtain additional data from four other transmitter locations. Thus, a second set of measurements was made in August 2010, targeting a path grazing the top of a foliated obstacle, as well as single and double diffraction paths across bare topped mountains.

Below are the details of the paths chosen for the different sets of experiments. This includes the line-of-sight and near line-of-sight paths from the Jack Ball transmitter location in 2009 and the heavily obstructed Horse Ridge transmitter location in 2009. In 2010, the grazing shot of a foliated obstacle was from the Short North 2 transmitter, while the transmitter at Bear Mountain provided diffraction over a single bare ridge, and Watering Pond North and Watering Pond Knob provided double diffraction paths.

7.1.1   2009 Paths

For the first set of experiments, two transmitter sites were chosen. The first, at the Jack Ball cabin (JB), was utilized with the Jansky Lab (JL) receiver as well as two additional mobile receiver points. The second, Horse Ridge (HR), utilized three mobile receiver points in addition to the Jansky Lab roof.

Figure 7.1 shows an overhead view of the Jack Ball transmitter location and its associated receiver locations. The square marked JB is the transmitter location, while Jansky Lab, the intermediate point (IP1), and water tower (WT) receiver locations are marked with

Figure 7.1: Jack Ball to Jansky Lab path
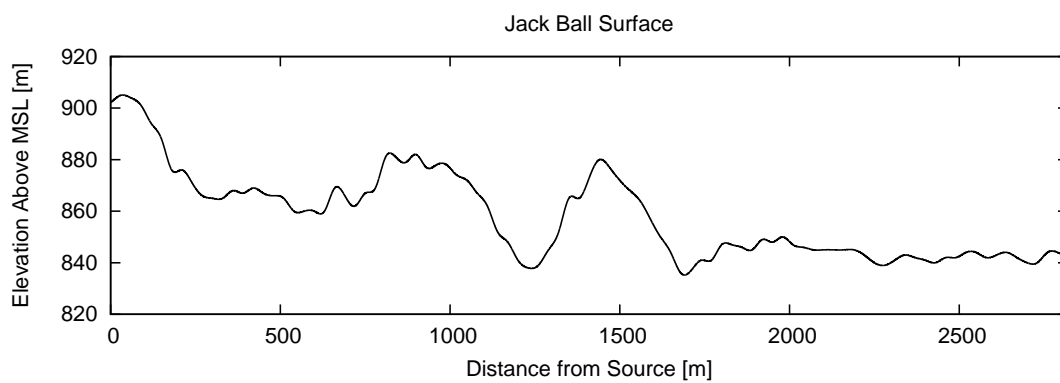
Figure 7.2: Profile of the Jack Ball to Jansky Lab path

circles [128]. The Jack Ball transmitter location is 38 26' 26.59" North latitude by 79 47' 22.88" West longitude, with GPS determined ground elevation of 912.8 meters AMSL. The JB to JL path contains a single foliated obstruction, which is a hill which peaks at approximately 1450 meters from the transmit location. Depending on the transmitter and receiver heights, this is either a slightly diffracting shot over the top of the obstacle, or a path with no ground obstructions. In either case, the foliage obstructs the path. The intermediate point (IP1) has a location of 38 26' 3.48" North latitude by 79 48' 33.99" West longitude, and elevation of 839.3 meters AMSL. The water tower was chosen as a receiver location as it provides a clear line-of-sight to the transmitter. The water tower location is 38 25' 59.19" North latitude by 79 49' 11.63" West longitude, ground elevation 833.4 meters AMSL, and a tower height of 34.4 meters.

The spline fit to the thirty meter terrain data for the Jack Ball to Jansky Lab path is plotted in figure 7.2 [3]. This path is approximately 2.8 km long, and contains either a single slight obstruction, or no obstruction, between the beginning and end of the path, based on the potential height above ground level of the transmitter and the receiver. While foliage is ignored for this model, the obstacle, located at approximately 1450 meters from the source, is foliated. At 1296 MHz, the path is approximately 12,000 wavelengths long. While this is not exceptionally long for a propagation path, it is long for a full wave solution technique.

Figure 7.3 shows an overhead view of the Horse Ridge transmitter location and its receiver sites [128]. The Horse Ridge site is the square labeled HR, while the Jansky Lab and intermediate receiver locations are circles. The three intermediate locations (IP3, IP4, and
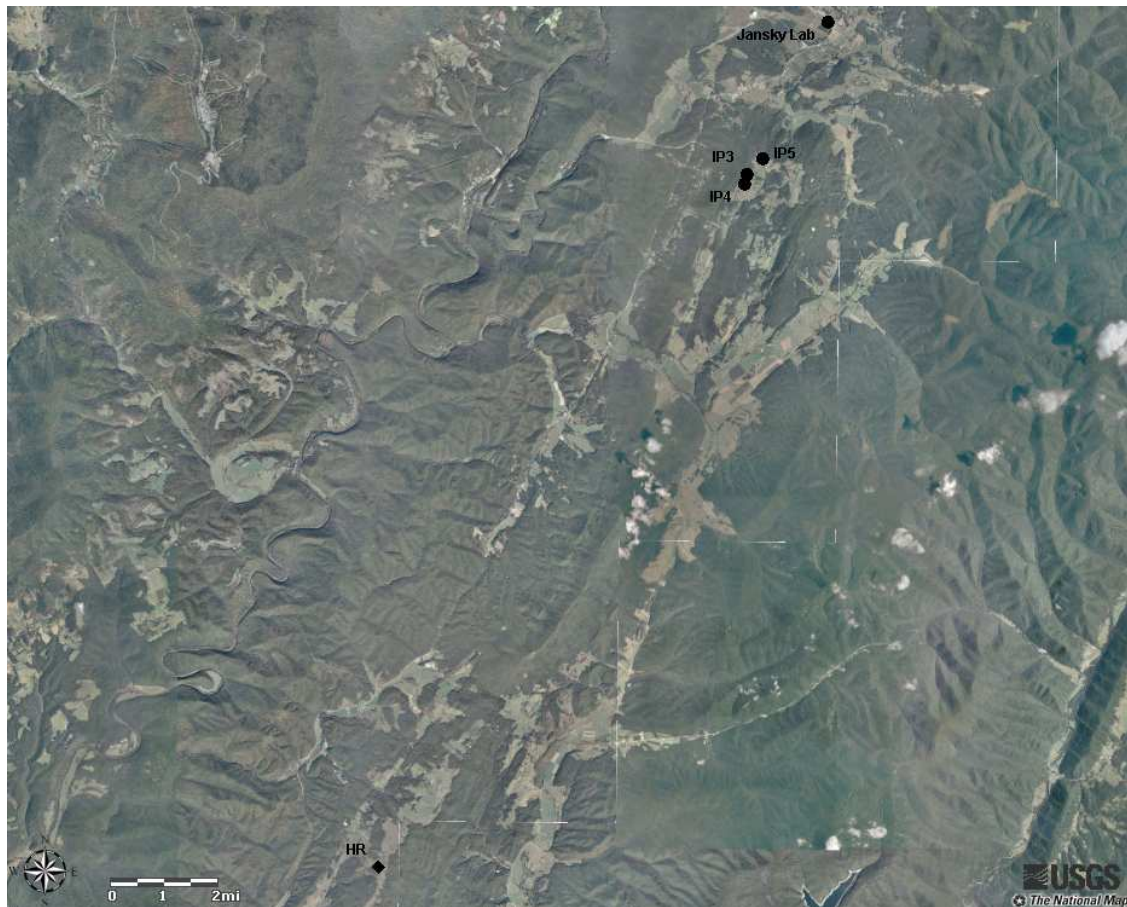
Figure 7.3: Horse Ridge to Jansky Lab path

IP5) are

- IP3 38 23' 50.95" North latitude by 79 50' 32.20" West longitude, ground elevation 910.0 meters AMSL

- IP4 38 23' 42.72" North latitude by 79 50' 34.44" West longitude, ground elevation 916.7 meters AMSL

- IP5 38 24' 2.83" North latitude by 79 50' 15.70" West longitude, ground elevation 882.9 meters AMSL
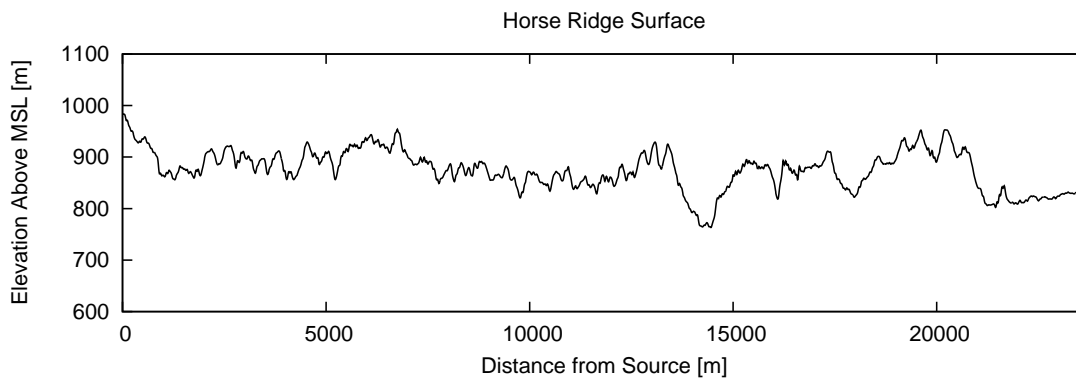
Figure 7.4: Profile of Horse Ridge to Jansky Lab path

The fit to the thirty meter terrain data for the Horse Ridge to Jansky Lab path is plotted in figure 7.4 [3]. The Horse Ridge transmitter is located at 38 14' 35.48" North latitude, 79 56' 48.38" West longitude, with GPS determined ground elevation of 990.6 meters AMSL. The Horse Ridge to Jansky Lab path is approximately 23.7 km long, and contains a large number of foliated ridges. The key obstruction between a transmitter located at the start of the path, and the Jansky Lab, is a ridge located approximately 20 km from the source.

While the Jack Ball path is short and has only a single obstruction to the receiver locations, the Horse Ridge path provides a longer path with multiple diffracting obstacles. Each of the intermediate points is likewise obstructed by foliated ridges. IP3 is 19.4 km from the transmitter, while IP4 is 19.2 km away and IP5 is 19.9 km away. All lie approximately along the straight line from Horse Ridge to the Jansky Lab.

7.1.2   2010 Paths

For the second round of experiments in 2010, paths of interest were those consisting of bare-earth diffractions. Transmission locations were chosen to have a grazing diffraction path, a heavily diffracting path, and two double-diffraction paths. For all of these paths, the sole receiver location was picked to be fixed at the Jansky Lab roof.
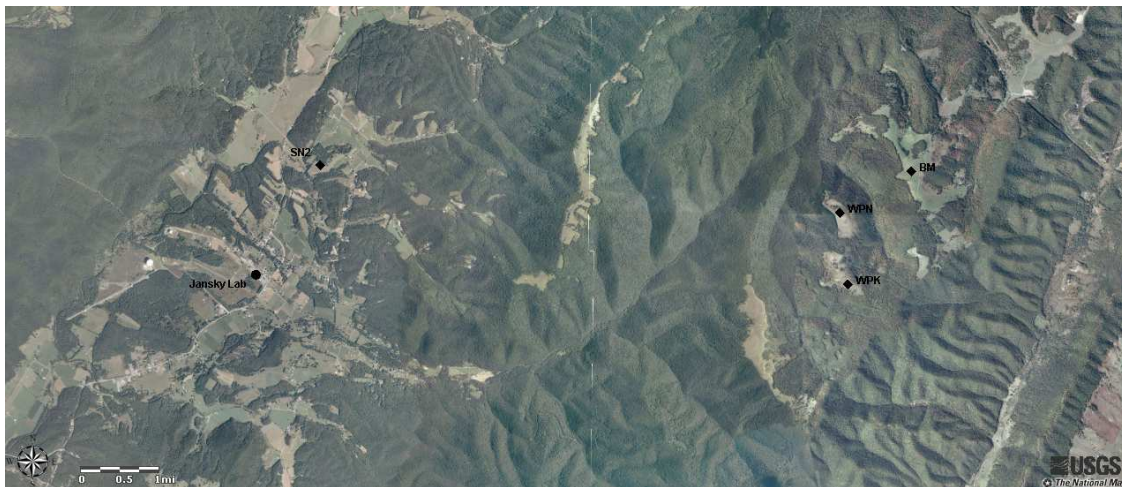
Figure 7.5: 2010 transmitter and receiver locations

The Short North Two (SN2) path is a 2.1 kilometer path with a single low grazing ob-

Short North 2 Surface
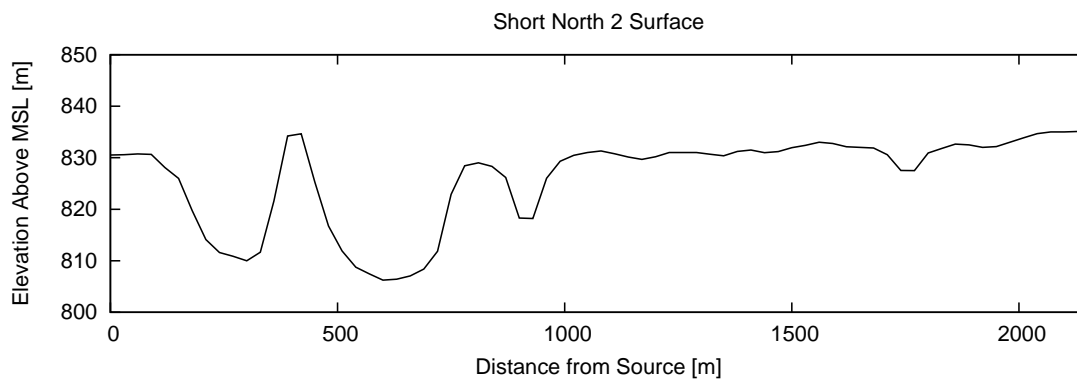
(a) Short North 2 to Jansky Lab

Bear Mountain Surface
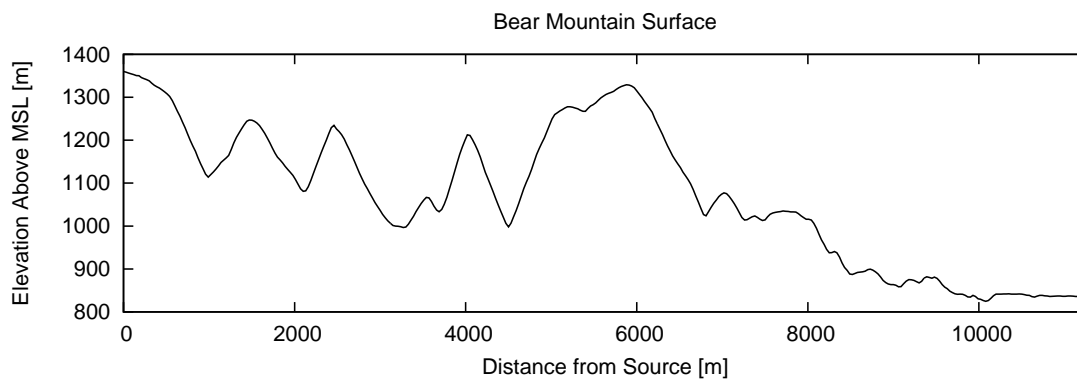
(b) Bear Mountain to Jansky Lab

Figure 7.6: Elevation Profiles for 2010 paths
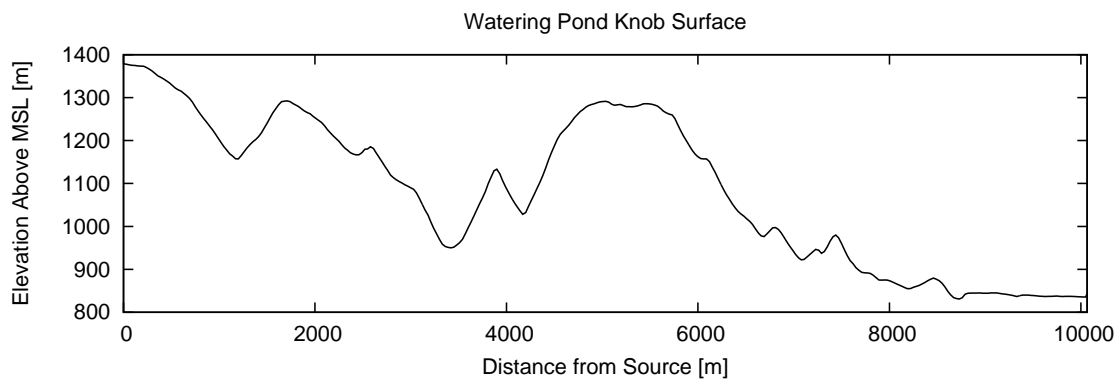
(c) Watering Pond Knob to Jansky Lab
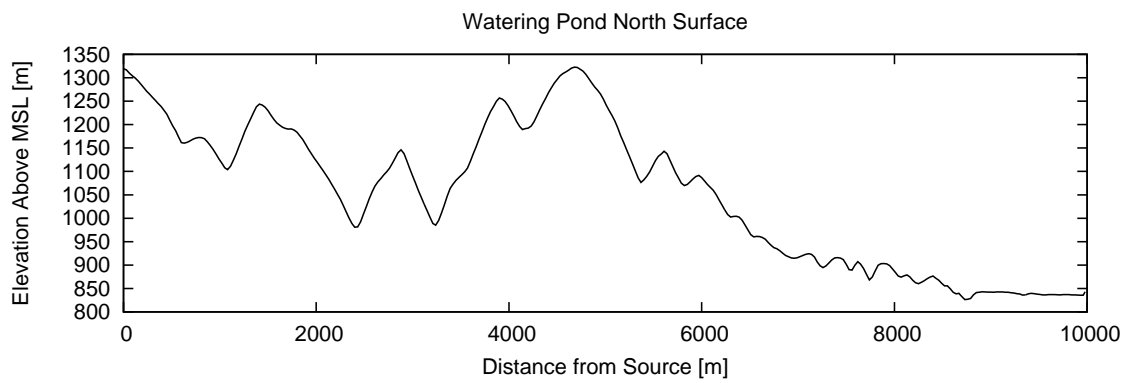
(d) Watering Pond North to Jansky Lab

Figure 7.6: Elevation Profiles for 2010 paths

struction. The obstruction is heavily foliated, and located close to the transmitter location at 3826'52.90" North latitude by 7948'24.60" West longitude. GPS measured ground elevation is 830.5 meters AMSL. The receiver for this path is located on the Jansky Lab roof. Overall, the path is fairly flat, with a total elevation variation of only 30 meters. The intent of the path is to check the validity of the model in the grazing incidence region. Figure 7.5 shows an overhead view of the path, from which it is observed that the path has intermittent foliage [128]. Additionally, Figure 7.6a shows the elevation profile of the path.

The Bear Mountain (BM) path is an 11.3 kilometer path with a large obstruction located near the midpoint of the path. The obstruction is a bare ridge line, providing a measurement of diffraction over a mountaintop. The transmitter is located at 3826'49.40" North latitude by 7941'30.40" West longitude and GPS measured elevation of 1360.2 meters AMSL, with the receiver at the Jansky Lab roof. Figure 7.6b shows the profile of the Bear Mountain path. This path is mountainous, with over 530 meters in elevation variation. The transmitter is located in a clearing near the ridge of a mountain.

The Watering Pond Knob (WPK) path is just over 10 kilometers and has approximately 550 meters of elevation change. It was chosen to provide double-diffraction of bare mountaintop. Looking at the profile shown in Figure 7.6c, the double peak of the obstructing mountain near the midpoint of the path is evident. The transmitter is located at 3825'47.40" North latitude by 7942'14.50" West longitude with an elevation of 1378.9 meters AMSL, and the receiver is at the Jansky Lab roof. Like the BM path, the transmitter is near the ridge line.

The Watering Pond North (WPN) path is just under 10 kilometers and has approximately

500 meters of elevation change. It provides another single bare diffracting ridge, again located near the middle of the path. Like the BM and WPK paths, the WPN path has a transmitter located high up a mountain side, at 3826'26.50" North latitude by 7942'20.10" West longitude and ground elevation of 1319.4 meters AMSL, and the receiver is at the Jansky Lab roof. Figure 7.6d shows the profile for this path.

All three of the mountainous 2010 test paths have significant foliage obstruction except along the obstacle peak. This can be seen in the overhead view in Figure 7.5. While this was not entirely desired, accessible locations without this difficulty could not be found in the NRQZ, which is mostly forested. The heavy foliage near the transmitters, combined with the weather conditions, caused a change to the measurement procedure. The foliage created significant time-variable multipath along all four paths. This resulted in large changes in signal levels at some frequencies. To work around this problem, maximum and minimum signal levels over a one-minute period were recorded, instead of just the steady signal levels seen in the 2009 measurements.

The BM, WPK, and WPN paths all provide test locations of a mountain-top transmitter diffracting over an adjacent ridge and into the next valley. Although there are foliage effects along the path, the ridge lines are clear. In all three paths, the mountain is a large obstruction, with diffraction providing the only reasonable signal path. These should provide a good test of the predictive capability of point-to-point models in mountainous terrain.

7.2   Methodology

This section specifies the experimental setup, including information on the transmitter and receiver, as well as the antennas. The transmitter was a pulsed radar transmitter connected to a Yagi antenna specific for each transmitting frequency. The lab-roof used matching Yagi antennas connected to a spectrum analyzer, with a low noise pre-amplifier when needed. The mobile receiver was a hand-held spectrum analyzer connected to a log-periodic antenna.

Following the details of the equipment used for the test is an explanation of the test procedure. The basic test procedure was to set up the equipment, point the transmitting antenna towards the receiver location, point the receiving antenna towards the transmitter, and record the received signal level. For a given frequency setup, the transmitter height was then changed and the measurements repeated. More specific details are given below.

7.2.1   Experiment Setup

The setup for the propagation experiments involves both the transmitter site and the receiver site. After determining suitable transmitter locations, a truck with the transmitter equipment is located at the transmitter location. A suitable site for the tower location is determined based on ground conditions, and the transmitter tower erected. During the experiment, the appropriate antenna is attached to the mast in the correct polarization orientation and connected to the transmitter. The antenna is then raised to the desired height, and visually aimed along the correct bearing. Then the transmitter is switched on

and allowed to stabilize before a confirmation is sent to the test director that the current configuration is ready for measurement.

The transmitter consists of a signal generator, pulse generator, and RF Amplifier, provided by Naval Surface Warfare Center, Dahlgren, VA (NSWC). Like all equipment for the test, the transmitter equipment is calibrated before testing, and checked after testing to ensure that the equipment maintained correct calibration. The transmitting antennas are Yagi antennas matched to the transmitting frequencies. The antenna patterns were measured by NSWC prior to the experiment and the measured antenna gain used to calibrate the results. Details of the antenna gains are provided in Table 7.1.

For the primary receiver site, the Jansky Lab roof, a twenty foot man-portable tower is erected on the roof top. During testing, the appropriate antenna is affixed to the mast in the correct polarization orientation. The antenna is connected by coaxial cable to the receiver, which is a calibrated bench top spectrum analyzer. The antenna is then visually pointed at the pre-determined bearing to the transmitter location. The spectrum analyzer is set on zero span at the target frequency with a one minute sweep time. The minimum possible resolution bandwidth setting, 100 kHz, is used. Because of the inability to receive the signal at some frequencies for the Horse Ridge Path in 2009, a low noise amplifier (LNA) was used for some paths in 2010. If the signal to noise ratio is low, or the signal is unobservable without amplification, then a 50-dB LNA is added to the receiver path before the spectrum analyzer. The Jansky Lab receiver site antennas are identical to the transmission antennas. During setup, the entire receiver path, including which antenna is used, which cables are

used, and the inclusion of any amplifiers, is recorded for later calibration purposes.

For the mobile receiver site, the hand-held antenna is connected to the portable spectrum analyzer. When taking a measurement, the antenna is held five feet off the ground and slowly swept across a narrow range of bearings where the transmitter should be located to find the bearing to maximum power reception. The bearing to maximum reception is then the bearing at which the measurement is observed and recorded. The same spectrum analyzer settings are used for the hand held spectrum analyzer as for the Jansky Lab bench-top spectrum analyzer. The hand-held log periodic antenna has a built in LNA which can be switched on if necessary to improve the signal-to-noise ratio.

Antennas

Four antennas were chosen for the measurements. At the transmitter and fixed receiver sites, three different Yagi antennas were used, one for 904 MHz and 926 MHz, a second for 1296 MHz, and a third at 2303 MHz. For the mobile receiver, a log periodic antenna was chosen as it has the bandwidth to operate across all the frequencies without the need to carry multiple or large antennas. The antenna patterns were measured prior to the experiment, and the gains used to calibrate the results. Table 7.1 shows the measured maximum gain for the transmitter and Jansky Lab receiver antennas, as well as the measured half power beamwidths. The gain is shown in decibels over an isotropic radiator, and the half power beamwidth in degrees. Table 7.2 shows the gain and beamwidth of the hand-held antenna used for the intermediate receiver locations. Table 7.2 also shows the calibrated gain of the

built-in LNA at each frequency.

Table 7.1: Yagi Antenna gains and beamwidths.

Frequency	Gain	3 dB Beamwidth
904 MHz	16.7 dBi	25°
926 MHz	17.4 dBi	23°
1296 MHz	16.1 dBi	14°
2303 MHz	14.0 dBi	37°

Table 7.2: Handheld Antenna gains and beamwidths.

Frequency	Antenna Gain	3 dB Beamwidth	LNA Gain Gain
904 MHz	4.7 dBi	119°	12.3 dB
926 MHz	5.0 dBi	118°	12.5 dB
1296 MHz	4.1 dBi	119°	11.8 dB
2303 MHz	2.8 dBi	121°	9.5 dB

7.2.2   Measurement Procedure

The test director, located at Jansky Lab, co-ordinates the activities of the transmitter and receiver teams via radio. For a given transmitter location, once a combination of transmitter height, frequency, and polarization has been confirmed ready for test by the transmitter team, and the receiver teams have verified that they are correctly set up and receiving the signal, the test director co-ordinates a measurement.

At the coordinated time, all teams measure the signal on zero-span for one minute. Then maximum and minimum signal levels for the one minute measurement are recorded by each team. Once each team has confirmed a successful measurement with the test director, the director can specify a new configuration for the transmit team, and if necessary the receiver team, to configure. At a given transmitter site and receiver site pair, each combination of transmitter height, frequency, and polarization is cycled through before proceeding to the next transmitter location.

The transmitter procedure is summarized as follows.

1. Setup the antenna, connect it to the transmitter, and raise it to the correct height.

2. Turn on the transmitter and adjust it to the correct frequency.

3. Verify that the transmitted signal is stable.

4. Notify the test director that the configuration is ready for measurement.

5. Record the transmitted power at the time of the measurement.

At the receiver, the procedure is summarized as:

1. Setup the antenna, connect it to the spectrum analyzer, and raise it to the correct height.

2. Wait for notification that the transmitted signal is stable.

3. Set the spectrum analyzer to a broad span, and verify that the signal is visible at the correct frequency and that the signal is more than several dB above the noise floor.

4. If the signal is not well above the noise floor, connect the LNA, and then recheck the signal visibility.

5. Set the spectrum analyzer to zero span at the measurement frequency and notify the test director that the receiver is ready for test.

6. Record the received maximum and minimum power over the one minute measurement window.

7.3   Measurement Results

Detailed tables of calibrated measurements are available in Appendix C. This section presents summarized results for each path, including the mean and standard deviations if multiple measurements were taken for a configuration. Recorded power measurements were converted to path loss by subtracting out all other known losses. The Friis Transmission Formula, equation (7.1), shows that the received power is a combination of transmitted power, antenna gains, and path loss [82].

$$P_r = \frac{P_t G_t G_r G_{LNA}}{L_t L_r L_p} \tag{7.1}$$

Here, P_t is the transmitter power, G_t is the gain of the transmitting antenna, G_r is the gain of the receiving antenna, G_{LNA} is the gain of the low noise amplifier, L_t represents any losses

in the transmitter, such as cabling losses, L_r are cabling losses in the receiver, and L_p is the path loss. When expressed in decibels, the path loss is computed as show in (7.2.

$$L_p^{dB} = P_r^{dB} - L_t^{dB} - L_r^{dB} - P_t^{dB} - G_t^{dB} - G_r^{dB} - G_{LNA}^{dB} \qquad (7.2)$$

Thus, the path loss, in dB, is computed from the received power by adding in all other losses, subtracting out all other gains, and subtracting off the received power. Here, loss values are expressed with negative decibel values and gains with positive decibel values.

7.3.1   Jack Ball transmitter location

Measurements were made on August 3, 4, and 6, 2009, between 9:00 am and 4:30 pm. The weather was foggy and cloudy in the mornings, and clear in the afternoons. Table 7.3 shows the results of measurements made at the Jansky Lab roof. The mean value computed for the path loss at each frequency, transmitter height, and polarization combination, as well as the standard deviation in the measurements when multiple measurements were made at one configuration, are presented in the table. Because mobile measurements were being made at both IP1 and the water tower, measurements setups were available at least twice for the twenty foot and thirty foot transmitter cases. Note that the standard deviations in the measurements range from 0.5 dB to 2.7 dB. N/A for standard deviation indicates that only one measurement was made at a particular configuration.

Table 7.4 shows the results of the measurements made at IP1. Only a single series of measurements was made, thus only the measured path loss is shown for each frequency,

Table 7.3: Experimental path loss measurements for transmission from Jack Ball to Jansky Lab.

Freq.	Tx Height	H-Pol		V-Pol	
(MHz)	(ft)	Path Loss (dB)	Std. Dev. (dB)	Path Loss (dB)	Std. Dev. (dB)
904	10	-116.11	N/A	-119.51	N/A
904	20	-114.33	1.87	-115.37	1.82
904	30	-112.59	1.03	-112.67	0.98
926	10	-116.44	N/A	-119.54	N/A
926	20	-116.25	1.06	-116.04	2.45
926	30	-112.69	0.57	-112.54	0.52
1296	10	-115.13	N/A	-118.27	N/A
1296	20	-117.52	2.67	-118.54	0.23
1296	30	-114.67	2.18	-115.31	0.57
2303	10	-132.72	N/A	-130.94	N/A
2303	20	-126.47	1.10	-127.06	0.19
2303	30	-121.36	1.47	-121.87	0.59

transmitter height, and polarization combination. Table 7.5 shows the measurements made at the catwalk of the water tower. Similarly to at IP1, only a single set of measurements was made at each setup. Also present in table 7.5 is the free space path loss, as computed by (6.17). This is provided because the path from Jack Ball to the water tower is a line-of-sight path with no obstructions, so many models suggest it should be close to the free space loss. It can be seen that the water tower measurements are generally within one to two decibels of the free space prediction. This accuracy provides a measure of confidence in the measurement setup.

Table 7.4: Experimental path loss measurements for transmission from Jack Ball to Intermediate Point 1.

Freq.	Tx Height	Path Loss (dB)	
(MHz)	(ft)	H-Pol	V-Pol
904	20	-121.16	-121.56
904	30	-120.44	-120.23
926	20	-122.09	-124.38
926	30	-120.41	-120.46
1296	20	-130.47	-131.13
1296	30	-127.43	-129.13
2303	20	-138.31	-133.23
2303	30	-133.95	-129.55

Table 7.5: Experimental path loss measurements for transmission from Jack Ball cabin to the water tower.

Freq.	Tx Height	Path Loss (dB)		
(MHz)	(ft)	H-Pol	V-Pol	Free Space
904	10	-98.41	-100.93	100.43
904	20	-102.30	-101.27	100.43
904	30	-101.41	-101.27	100.43
926	10	-98.81	-100.35	100.64
926	20	-102.30	-103.08	100.64
926	30	-102.73	-101.68	100.64
1296	10	-107.63	-107.03	103.56
1296	20	-103.97	-104.50	103.56
1296	30	-105.05	-105.57	103.56
2303	10	-106.61	-105.41	108.55
2303	20	-110.23	-109.38	108.55
2303	30	-109.38	-109.73	108.55

7.3.2   Horse Ridge transmitter location

Measurements from the Horse Ridge location were made on August 5, 2009. The weather was similar to the weather for the Jack Ball transmission. The 30 feet transmitter height measurements at Jansky Lab were made three times, while single measurements were taken at IP3, IP4, and IP5. To allow multiple intermediate point measurements to be taken, the procedure here was altered after the first location to only transmit from 30 feet, where the best chance of detecting the signal should be present.

Table 7.6 shows results as measured at Jansky Lab. This includes most of the expected data points, although the signal was not observed at 2303 MHz. The noise floor there was equivalent to a path loss of -155 dB for horizontal polarization and -152 dB for vertical polarization. As the path loss increases with frequency, and exceeded these levels at 1296 MHz, it is not surprising that a signal was not visible. The signal was below the noise floor at 2303 MHz. 10 and 20 ft. transmitter heights were not measured due to time constraints. N/A for standard deviation indicates only one measurement was made in that configuration. Table 7.7 shows the results of the measurements at IP3. While some measurements were made at that location at differing transmitter heights, a decision was made to focus on the 30 foot transmitter height to avoid the time delays associated with multiple antenna adjustments. The signal was below the noise floor at 2303 MHz. 10 and 20 ft. transmitter heights were not measured at this location due to time constraints. Table 7.8 shows the results of the measurements at IP4. As with IP3, measurements focused on the 30 foot transmitter height. This is the only location at which the 2303 MHz signal was visible from

Table 7.6: Experimental path loss measurements for transmission from Horse Ridge to Jansky Lab.

Freq.	Tx Height	H-Pol		V-Pol	
(MHz)	(ft)	Path Loss (dB)	Std. Dev. (dB)	Path Loss (dB)	Std. Dev. (dB)
904	30	-142.27	1.55	-142.78	0.84
926	10	-145.27	N/A		
926	20	-144.94	N/A		
926	30	-142.71	1.22	-142.22	1.07
1296	10	-160.31	N/A		
1296	20	-154.72	N/A	-156.14	N/A
1296	30	-155.32	1.64	-156.76	0.54

Table 7.7: Experimental path loss measurements for transmission from Horse Ridge to Intermediate Point 3.

Freq.	Tx Height	Path Loss (dB)	
(MHz)	(ft)	H-Pol	V-Pol
904	30	-140.18	-137.27
926	10	-141.43	
926	20	-140.97	
926	30	-137.43	-142.53
1296	20	-149.73	-155.07
1296	30	-151.33	-156.19

the Horse Ridge transmitter; it is also the closest receiver location to the transmitter. 10 and 20 ft. transmitter heights were not measured at this location due to time constraints. Table

Table 7.8: Experimental path loss measurements for transmission from Horse Ridge to IP4.

Freq. (MHz)	Tx Height (ft)	Path Loss (dB)	
		H-Pol	V-Pol
904	30	-127.11	-130.22
926	30	-129.20	-130.97
1296	30	-132.43	-138.40
2303	30	-142.75	-137.41

7.9 shows the results of the measurements at IP5. As with IP3, measurements focused on the 30 foot transmitter height. Also as at IP3, 2303 MHz measurements were not possible. As with the other intermediate points, 10 and 20 ft. transmitter heights were not measured due to time constraints.

Table 7.9: Experimental path loss measurements for transmission from Horse Ridge to IP5.

Freq. (MHz)	Tx Height (ft)	Path Loss (dB)	
		H-Pol	V-Pol
904	30	-153.52	-148.23
926	30	-149.58	-150.08
1296	30	-151.83	-153.65

7.3.3   Short North 2 to Jansky Lab

As previously mentioned, the measurements made in 2010 were chosen to fill in some of the gaps in the 2009 data set. The Short North 2 to Jansky Lab path was chosen for the

grazing incidence across a hill top. Also, the measurement procedure was changed to include measurement of minimum and maximum signal levels over a 1 min. observation period. This allows some measure of the foliage effects. Additionally, as seen in Table 7.10, some results are included for a forty foot transmitter height. These measurements were taken on August 2 and 3, 2010. However, only one set of measurements was made at each setup for this experiment, so standard deviation from multiple measurements is not available. Significant time variation in the results is evidence of multipath scattering resulting from the foliage obstruction and wind.

7.3.4   Bear Mountain to Jansky Lab

Table 7.11 shows the results of measurements made between Bear Mountain and Jansky Lab. The ten foot transmitter height was not used at this location. Measurements were made the afternoon of August 3, 2010. Note that variation in the environment is lower than for the Short North 2 path, although some measurements were made the same day. Due to time constraints, 10 ft. transmitter heights at all frequencies, and 30 ft. transmission at 2303 MHz were not measured.

7.3.5   Watering Pond North to Jansky Lab

Table 7.12 shows the measurement results from the Watering Pond North to Jansky Lab, as made on the morning of August 4, 2010. The weather that morning was overcast with wind

Table 7.10: Experimental path loss measurements for transmission from Short North 2 to Jansky Lab.

Freq.	Tx Height	H-Pol Path Loss (dB)		V-Pol Path Loss (dB)	
(MHz)	(ft)	Min	Max	Min	Max
904	10	-121.30	-122.17	-134.26	-134.26
904	20	-116.84	-117.61	-122.38	-124.59
904	30	-116.56	-117.28	-123.02	-123.44
904	40	N/A	N/A	-119.32	-121.42
926	10	-123.81	-125.08	-131.18	-131.18
926	20	-120.80	-121.15	-129.37	-132.60
926	30	-121.68	-122.73	-127.06	-127.73
926	40	N/A	N/A	-119.63	-122.25
1296	10	-121.88	-121.88	-123.82	-124.90
1296	20	-121.72	-125.28	-124.23	-126.67
1296	30	-121.03	-121.70	-127.81	-129.44
1296	40	-119.42	-121.23	N/A	N/A
2303	10	-145.84	-148.68	-135.51	-140.65
2303	20	-140.35	-144.02	-136.96	-144.25
2303	30	-141.28	-154.99	-137.07	-146.06

Table 7.11: Experimental path loss measurements for transmission from Bear Mountain to Jansky Lab.

Freq. (MHz)	Tx Height (ft)	H-Pol Path Loss (dB)		V-Pol Path Loss (dB)	
		Min	Max	Min	Max
904	20	-182.78	-185.62	-167.66	-169.34
904	30	-177.35	-180.31	-163.91	-166.89
926	20	-172.45	-173.77	-163.51	-164.73
926	30	-164.46	-165.53	-159.43	-160.98
1296	20	-169.31	-171.09	-171.72	-173.25
1296	30	-175.31	-177.55	-160.50	-162.08
2303	20	-165.97	-167.03	-170.00	-172.54

and rain. Larger variations are present in the results than in the Bear Mountain Path, likely due to higher winds. To fit in both the Watering Pond North and Watering Pond Knob measurements that day, the ten foot transmitter height was not measured. Measurements listed as N/A were not taken due to the arrival of incliment weather.

Table 7.12: Experimental path loss measurements for transmission from Watering Pond North to Jansky Lab.

Freq. (MHz)	Tx Height (ft)	H-Pol Path Loss (dB)		V-Pol Path Loss (dB)	
		Min	Max	Min	Max
904	20	-156.76	-159.62	-151.85	-158.45
904	30	-152.44	-154.40	-148.98	-151.87
926	20	-153.25	-155.37	N/A	N/A
926	30	-149.11	-150.30	-146.07	-148.85
1296	20	-153.49	-157.48	-162.54	-167.74
1296	30	N/A	N/A	-157.70	-164.98
2303	20	-159.69	-166.09	-160.43	-173.70
2303	30	-162.64	-173.15	-163.28	-179.88

7.3.6   Watering Pond Knob to Jansky Lab

Table 7.13 shows the measurement results from the Watering Pond Knob to Jansky Lab. Measurements were made on the afternoon of August 4, 2010. The weather continued to deteriorate, with strong winds and thunderstorms moving in towards the end of the measurement period. The high winds combined with foliage is the likely cause of the large signal variations present in the results. Of special note are the variations as large as 24 dB in the received signal strength on a one minute measurement trace at 926 MHz in horizontal polarization.

Table 7.13: Experimental path loss measurements for transmission from Watering Pond Knob to Jansky Lab.

Freq. (MHz)	Tx Height (ft)	H-Pol Path Loss (dB)		V-Pol Path Loss (dB)	
		Min	Max	Min	Max
904	20	-151.67	-157.43	-155.39	-168.19
904	30	-151.58	-161.30	-156.48	-164.64
926	20	-162.73	-187.21	-160.60	-184.41
926	30	-160.11	-180.30	-164.54	-181.67
1296	20	-149.38	-154.49	-155.80	-168.33
1296	30	-150.55	-154.61	-155.46	-164.69
2303	20	-158.35	-173.38	-156.98	-164.95
2303	30	-156.35	-163.58	-156.48	-162.85

7.4 Conclusions

This chapter presented the experimental setup and results for propagation measurements made in the vicinity of Green Bank, West Virginia in 2009 and 2010. The measurements were made to provide a means of validating the computation results that will be presented in the following chapter. As stated earlier, measurements were needed because few point-to-point propagation measurement campaigns had been carried out in mountainous environments.

In the process of setting up the experiment, much was learned about the cause for the lack of data at VHF and higher frequencies. The goal of measuring propagation from transmitters located on mountain peaks is made more difficult by the lack of infrastructure at such locations. Finding clear sights near roads for locating a test transmitter is not simple, and roads are sparse in mountainous terrain, making locating observation points along a single line difficult. Furthermore, as born out by the data, transmission over several mountain obstructions can quickly put the signal below the noise floor of the receiver. Additionally, mountains in West Virginia tend to be heavily foliated, which was observed to further degrade the signal strength. Finally, weather concerns cause additional problems with measurement, as the wind interacts with foliage to produce large amounts of fading.

Despite these difficulties, it was possible to take measurements along a set of paths around NRAO Green Bank. In some cases, the measurements were stable, while in others, as mentioned, large time variations in signal strength were present. Although the data presented in this chapter is incomplete in terms of what was hoped to be measured, in terms

of combinations of frequencies, locations, and transmitter heights, it should still be sufficient for model validation.

Chapter 8

Computational Results and

Comparison to Experiment

The primary goal of this work is to develop a technique for propagation modeling that can be used to estimate the impact of topographic data sparsity on propagation prediction. As was previously stated, MOMI was chosen because it is a fast method of solving the MFIE, enabling the accurate solution of the electromagnetic scattering problem. The previous chapters show the past developments on MOMI that are being applied to this propagation modeling. Additionally, the surface generation has been described, and a set of measurements have been collected for use in validating the model. What remains is to show how this initial model works, and describe the improvements that are necessary to use MOMI for propagation modeling.

This chapter begins by showing a comparison of baseline MOMI results, using the techniques of past work, to the measurements shown in the Chapter 7. These results show that MOMI is not completely accurate in computing propagation loss, even when accounting for terrain variation. Following that are the descriptions of several changes that have been made to the technique to improve on the propagation modeling.

Section 6.3.1 describes a simic method for converting the 2-D MOMI results into a 3-D path loss number, based on the free space path loss in two and three dimensions. However, that result does not work as well for diffracting paths. After showing initial results, a new method will be developed that more accurately merges in the power spread in the third dimension. This new method is based on the caustic distance idea from geometric optics, and will be shown to slightly improve the results.

Following those results, antenna patterns will be added to the scattering formulation. The results with the antenna pattern included will then be compared to the pattern-less results for a limited selection of cases. Finally, the results for all paths will be shown with all the improvements in place.

8.1   Initial MOMI Results

Chapters 4 and 6 describe the basis of the techniques for computing the path loss, or propagation loss due to power spread and terrain, that are employed here. First, the spline fit for the two dimensional propagation path is computed based on the terrain data for the

path. Then, that spline fit is added to a randomly rough surface which is forced to zero at the known data points, as described in section 6.2. Assuming that the ground is a PEC, MOMI is then used to compute the total electric and magnetic fields above the surface under the illumination of an electric line source (TE or horizontal polarization) or a magnetic line source (TM or vertical polarization). This process is described in Chapter 4. Finally, the fields located at the receiver location are used to compute the path loss 6.3.1.

One factor which has not been specified previously is the variation that should be present in the randomly rough surfaces used for the computations. It would be ideal to perform the computations with a variety of roughness spectra and see how the results change. However, the MOMI and scattering computations are very time intensive at the scales involved here. As a reference, a single MOMI solution of the MFIE for the Jack Ball to Jansky Lab path (2.8 kilometers long) at 1296 MHz could be computed in approximately one hour on a single Itanium processor. Thus, results for 100 random surfaces, with two polarizations, and three transmitter heights, the results would take 600 processor hours for a relatively short path for one frequency. Because of this, a single value for the root mean square height was chosen and used for the computations. The value of 60 centimeters, or approximately 2 feet, was chosen and used in all computations presented in this chapter.

The Jack Ball to Jansky Lab (JB) and Horse Ridge to Jansky Lab (HR) paths were described in Chapter 7, where the measurements taken at those locations were presented. These paths provide a basic set of comparisons for the results of MOMI to measured data.

8.1.1   The Jack Ball Path

The spline fit to the thirty meter terrain data for the Jack Ball Path is plotted in figure 7.2. This path is approximately 2.8 km long, and contains either a single slight obstruction, or no obstruction, between the beginning and end of the path, based on the potential height above ground level of the transmitter and the receiver. While foliage is ignored for this model, the obstacle, located at approximately 1450 meters from the source, is foliated. At the frequency of interest for the potential experiments, 1296 MHz, the path is approximately 12,000 wavelengths long. While this is not exceptionally long for a propagation path, it is long for a full wave solution technique.

While there is only the single obstruction between the start and end points of the path, varying levels of obstruction are available at different places along the path. Figure 8.1 shows the result of the MOMI propagation prediction technique applied solely to the spline fit for a frequency of 1296 MHz. The plot shows both TE (horizontal polarization or H-pol) and TM (vertical polarization or V-pol) results, with the spline surface below for reference. For this plot, the transmitter is located six meters above the ground, and the receiver is moving along the path two meters above the ground, or at approximately cell-phone height. The solid line is the free space loss line, that is, the loss that would be expected in the absence of any surface, which is presented as a reference. The free space loss is that given in (6.12). Also shown is the loss predicted by the Hata model, which is given by (6.29). As should be expected since the Hata model provides an empirical median loss, the MOMI loss oscillates above and below the Hata line, showing that the more specific prediction which accounts for
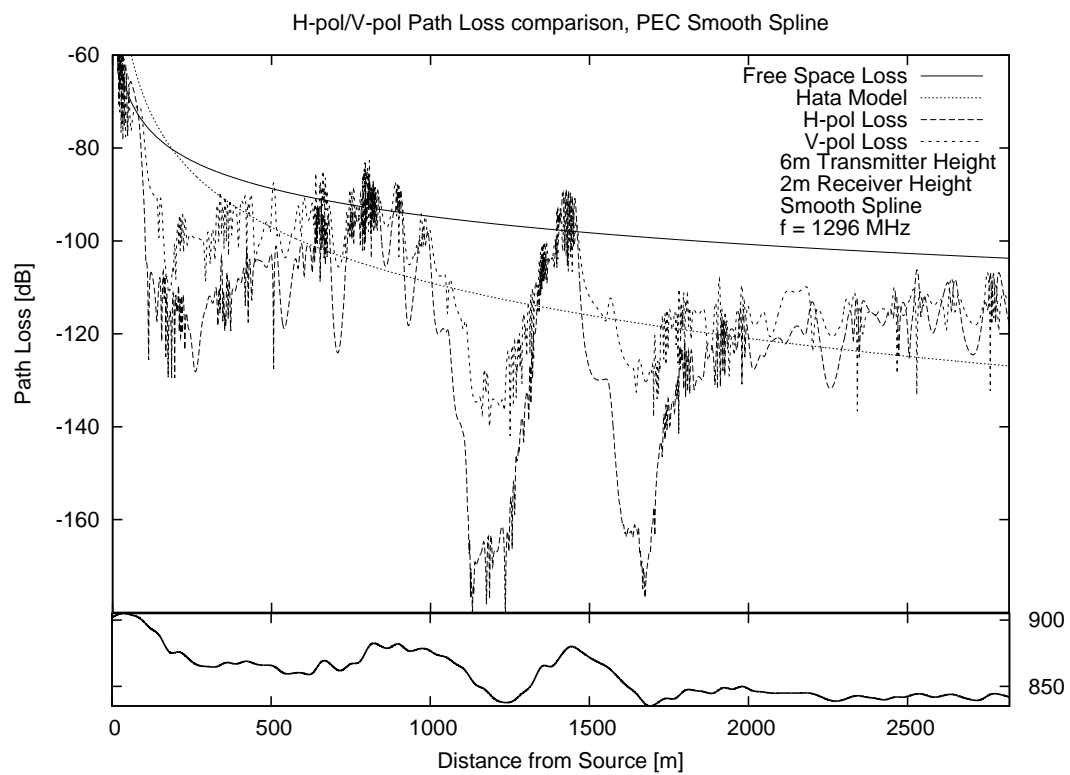
Figure 8.1: Computed loss along the Jack Ball spline path for a transmitter 6 meters above the surface, and a receiver moving along 2 meters above the surface.

terrain losses moves around the Hata median.

Note that in Figure 8.1 the result shows the expected increases and decreases in signal level due to terrain obstructions. Further, it shows an increase in signal level near the tops of hills facing the transmit side which is also noted by Ott [87]. As mentioned by Ott, this effect is not predicted by the typical diffraction-focused propagation techniques.

Comparison to Measurements

While some information may be obtained by looking at a solution to a single smooth surface, the comparison of the technique to measured data is important for validation. Tables 8.1 and 8.2 show the results of the one hundred realizations of the MOMI technique to the measured data for the Jack Ball to Jansky Lab path. Table 8.1 is for horizontal polarization and Table 8.2 is for vertical polarization.

The frequency column is the frequency of the measurement in MHz, while the "Tx. Height" column lists the transmitter height of the measurements in feet. All measurements were taken on the Jansky Lab roof with the receiver at a height of 20 feet above the roof, while the transmitter height was varied. The "Meas." column shows the measured path loss presented in Chapter 7 and the "Meas. σ" column shows the standard deviation of the measurements, with "N/A" used to denote cases where only one measurement was made. The "MOMI" column shows the computed mean path loss for 100 Monte-Carlo realizations as previously described, and the "MOMI σ" column shows the standard deviation in the

Table 8.1: Comparison of measured data to MOMI for Jack Ball to Jansky Lab for horizontal polarization. (All values except frequency and height are in dB.)

Freq. (MHz)	Tx. Height (ft)	Meas.	Meas. σ	MOMI	MOMI σ	Δ
904	10	-116.11	N/A	-97.95	1.31	18.16
904	20	-114.33	1.87	-97.49	1.50	16.84
904	30	-112.59	1.03	-101.70	2.97	10.89
926	10	-116.44	N/A	-98.62	1.62	17.82
926	20	-116.25	1.06	-97.61	1.38	18.64
926	30	-112.69	0.57	-102.98	3.24	9.71
1296	10	-115.13	N/A	-100.18	1.48	14.95
1296	20	-117.52	2.67	-101.57	2.02	15.95
1296	30	-114.67	2.18	-103.83	3.07	10.84
2303	10	-132.72	N/A	-104.56	1.39	28.16
2303	20	-126.47	1.10	-107.73	2.44	18.74
2303	30	-121.36	1.47	-108.05	2.90	13.31
RMS			1.63		2.23	16.85

Table 8.2: Comparison of measured data to MOMI for Jack Ball to Jansky Lab for vertical polarization. (All values except frequency and height are in dB.)

Freq. (MHz)	Tx. Height (ft)	Meas.	Meas. σ	MOMI	MOMI σ	Δ
904	10	-119.51	N/A	-114.28	1.12	5.23
904	20	-115.37	1.82	-104.26	0.58	11.11
904	30	-112.67	0.98	-104.05	0.71	8.62
926	10	-119.54	N/A	-115.01	1.23	4.53
926	20	-116.04	2.45	-104.79	0.56	11.25
926	30	-112.54	0.52	-104.81	0.65	7.73
1296	10	-118.27	N/A	-119.22	1.08	-0.95
1296	20	-118.54	0.23	-107.49	0.54	11.05
1296	30	-115.31	0.57	-107.14	0.57	8.17
2303	10	-130.94	N/A	-126.11	1.02	4.83
2303	20	-127.06	0.19	-112.06	0.53	15.00
2303	30	-121.87	0.59	-111.21	0.55	10.66
RMS			1.19		0.80	9.05

computations resulting from the surface variation. The "Δ" column is the difference, in dB, between the measurement and the MOMI path loss computation. The "RMS" row at the bottom shows the root mean square value of all results in the respective columns, which is most meaningful for the "Δ" column. This RMS Δ value is the RMS error between the MOMI computed path loss prediction and the measured value.

The main values of importance are the results in RMS results, representing the average error for all measurements or computations across the Jack Ball to Jansky Lab path. For horizontal polarization, this 16.9 dB error between measurement and computation is extremely large, and only partially offset by the ±1.6 dB of measurement error and the ±2.2 dB computation variation resulting from terrain randomization. This indicates that in horizontal polarization, the model is very poor. For vertical polarization, the results are somewhat better, with 9.1 dB of error between computation and measurement, and ±1.2 dB of measurement error and ±0.8 dB accounted for by terrain variation. This is still almost an order of magnitude of error, however.

8.1.2   Horse Ridge

Like for the Jack Ball to Jansky Lab results, the following tables, Tables 8.3 and 8.4, show the results of the one hundred realizations of the MOMI technique to the measured data for the Horse Ridge to Jansky Lab path. Table 8.3 is for horizontal polarization and Table 8.4 is for vertical polarization. As in the prior case, all values except for the frequency, in

MHz, and the transmitter height, in feet, are listed in dB. The "Meas." and "Meas. σ" columns show the Horse Ridge to Jansky Lab measurement result and standard deviation as described in Chapter 7. The "MOMI" and "MOMI σ" columns are the mean and standard deviation of the results computed using the MOMI technique. Δ is the difference between the MOMI mean and the measurement mean.

Table 8.3: Comparison of measured data to MOMI for Horse Ridge to Jansky Lab for horizontal polarization. (All values except frequency and height are in dB.)

Freq. (MHz)	Tx. Height (ft)	Meas.	Meas. σ	MOMI	MOMI σ	Δ
904	30	-142.27	1.55	-149.68	1.33	-7.41
926	10	-145.27	N/A	-149.80	1.40	-4.53
926	20	-144.94	N/A	-150.05	1.67	-5.11
926	30	-142.71	1.22	-148.80	1.69	-6.09
1296	10	-160.31	N/A	-156.62	2.10	3.69
1296	20	-154.72	N/A	-154.90	2.04	-0.18
1296	30	-155.32	1.64	-154.97	2.23	0.35
RMS			1.48		1.81	4.67

Table 8.4: Comparison of measured data to MOMI for Horse Ridge to Jansky Lab for vertical polarization. (All values except frequency and height are in dB.)

Freq. (MHz)	Tx. Height (ft)	Meas.	Meas. σ	MOMI	MOMI σ	Δ
904	30	-142.78	0.84	-146.39	2.04	-3.61
926	30	-142.22	1.07	-146.06	2.04	-3.84
1296	20	-156.14	N/A	-150.46	1.81	5.68
1296	30	-156.76	0.54	-151.34	2.30	5.42
RMS			0.85		1.91	4.73

Fewer results are listed for the Horse Ridge to Jansky Lab case because fewer mea-

surements were taken. As mentioned in Chapter 7, 2303 MHz transmission was below the measurable level on the path, and some measurements were not made at 904 MHz because of time constraints. Of note, however, is that the computations and results are much closer on these results than for the Jack Ball path, with the approximately 4.7 dB of error in both polarizations being much better than the 9 to 16 dB present for the Jack Ball computations. One likely reason for this is that the Horse Ridge path is heavily obstructed, and while foliage may have some effect, it is not adding significantly to the path obstruction, while the Jack Ball path would be nearly line-of-sight without foliage, but the foliage may add another 60 to 100 feet to the obstacle height.

8.2   Two Dimensional to Three Dimensional Field Conversion

As mentioned in Chapter 6, the 2D MOMI results are not directly applicable to a 3D propagation loss. It was shown in that chapter that in a real communications link, free space propagation loss is represented by the spreading of the power over a sphere [82]. In 2D, this power is only spread over a circle, and the resulting power loss changes by a factor of $2r$, as can be seen in the following equations [7].

$$L_p^{3D} = \frac{(4\pi r)^2}{\lambda^2} \tag{8.1}$$

$$L_p^{2D} = \frac{8\pi r}{\lambda^2} \tag{8.2}$$
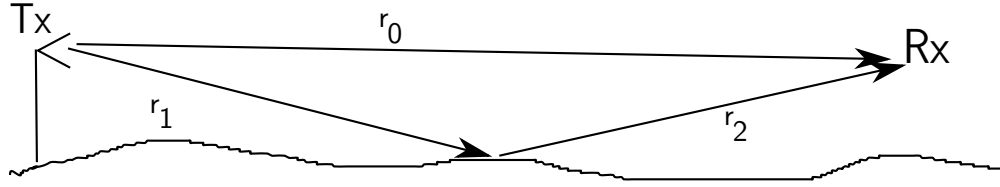
Figure 8.2: Setup of scattering problem

Thus, the initial attempts to convert the results from MOMI to representative 3D path loss just took the approach of normalizing both the direct and scattered power by a factor of $2r_0$, where r_0 is the distance between the transmitter and the observation point, as seen in Figure 8.2. However, these results were not consistent with the measured data. The two dimensional scattered field, ψ_{scat}^{2D}, can be represented by (8.3), and the first attempt at an equivalent three dimensional field is given by (8.4).

$$\psi_{scat}^{2D}(\mathbf{r}) = \int_S \psi(\mathbf{r}')G^{2D}(\mathbf{r}, \mathbf{r}')dl' \tag{8.3}$$

$$\psi_{scat}^{3D}(\mathbf{r}) = \frac{1}{sqrt2r_0}\psi_{scat}^{2D}(\mathbf{r}) \tag{8.4}$$

Here, ψ is a generic reference to the tangential field, that is E_y in TE, and H_y in TM, located at the surface. In the case of MOMI on a PEC, ψ is the current which has been solved for. The point of observation is $\mathbf{r}$, the scattering point from the surface, $\mathbf{r}'$ is the variable of integration, and G^{2D} is the Green's function for the scattering process. The original approximation of the three dimensional equivalent ψ^{2D} is then ψ^{3D}, where r_0 is the distance from the source to the observation point, as shown in Figure 8.2.

An alternate approach to the 2D conversion is to treat MOMI as producing the optics reflection or diffraction currents along the main propagation path. In this case, the goal of

the additional term is to account for the change in the caustic in the 3rd dimension, while MOMI has already accounted for it in the x-z plane. In geometric optics, the caustic is the point of the singularity where multiple ray paths cross, such as the location of a point source [93]. For a single reflection or diffraction from each surface point, $r_1 + r_2$ is the caustic length in the $\hat{\mathbf{y}}$ place, assuming that scattering is from the corrugated surface of the 2-D case [117]. Then a new form of the scattering integral can be obtained by bringing the resulting caustic distance into the integration. This integral produces a three-dimensional result directly from the two-dimensional MOMI solution.

$$\psi_{scat}^{3D}(\mathbf{r}) = \int_S \psi(\mathbf{r}')G^{2D}(\mathbf{r},\mathbf{r}')\frac{1}{\sqrt{2(r_1 + r_2)}}dl' \tag{8.5}$$

The term r_1 is the distance from the source to the scattering point, while r_2 is the distance from the scattering point to the observation point, as seen in Figure 8.2. The other terms are the same as in (8.3).

When the specific scattering integrals for both polarizations, given in (3.36a), (3.36b), (3.37a) and (3.37b), are combined with (8.5), the form for computing the three dimensional scattered fields is from the two-dimensional MOMI surface currents is obtained. For the TE case, the resulting scattering integrals are

$$\mathbf{H}_{TE}^{3D} = \frac{-jk_0}{4}\int_{S_0}\frac{\hat{\boldsymbol{\beta}}}{\sqrt{2(r_1 + r_2)}}J(\mathbf{r}_0)H_1^{(2)}(k_0\alpha)\,\mathrm{d}l_0 \tag{8.6}$$

$$\mathbf{E}_{TE}^{3D} = \hat{\mathbf{y}}\frac{\eta k_0}{4}\int_{S_0}\frac{1}{\sqrt{2(r_1 + r_2)}}J(\mathbf{r}_0)H_0^{(2)}(k_0\alpha)\,\mathrm{d}l_0 \tag{8.7}$$

For the TM case, the scattering integrals are

$$\mathbf{H}_{TM}^{3D} = -\hat{\mathbf{y}}\frac{jk_0}{4}\int_{S_0}\frac{\hat{\boldsymbol{\beta}}\cdot\hat{\mathbf{s}}_0}{\sqrt{2(r_1+r_2)}}J(\mathbf{r}_0)H_1^{(2)}(k_0\alpha)\,\mathrm{d}l_0 \tag{8.8}$$

$$\mathbf{E}_{TM}^{3D} = \frac{\eta k_0}{4}\int_{S_0}\left[\hat{\boldsymbol{\beta}}(\hat{\boldsymbol{\beta}}\cdot\hat{\mathbf{s}}_0)\left(H_0^{(2)}(k_0\alpha) - \frac{H_1^{(2)}(k_0\alpha)}{k_0\alpha}\right)\right.$$
$$\left.+\hat{\boldsymbol{\alpha}}(\hat{\boldsymbol{\alpha}}\cdot\hat{\mathbf{s}}_0)\frac{H_1^{(2)}(k_0\alpha)}{k_0\alpha}\right]J(\mathbf{r}_0)\frac{1}{\sqrt{2(r_1+r_2)}}\mathrm{d}l_0 \tag{8.9}$$

For all of these integrals, $\mathbf{E}^{3D}$ and $\mathbf{H}^{3D}$ are the three dimensional scattered field quantities, $J(\mathbf{r}_0)$ is the scalar value of the equivalent electric current along the surface, r_1 and r_2 are the distances shown in Figure 8.2. The vectors $\boldsymbol{\alpha}$, $\boldsymbol{\beta}$, $\hat{\mathbf{n}}$, and $\hat{\mathbf{s}}$ are as defined in Chapter 3, and shown in Figure 3.2, with $\hat{\mathbf{n}}$ and $\hat{\mathbf{s}}$ as the unit normal and unit tangent vectors for the surface, and $\boldsymbol{\alpha} = \mathbf{r}_2$ and $\boldsymbol{\beta} = \hat{\mathbf{y}}\times\boldsymbol{\alpha}$ the cylindrical coordinates around the scattering location.

To test this result, it was applied to the case of a horizontal dipole over a flat surface, so that it can be compared with image theory. The results are shown in Figure 8.3 which shows the fields produced by each of the three methods. The field magnitude produced by image theory, which is an exact solution, are shown by the black line, with the '+' points representing the original method, and the 'x' points showing the results of the new method. Additionally, the relative error of the two methods compared to the exact result of image theory is shown in Figure 8.4. Note that in the far field, beyond approximately 100 wavelengths, both methods are equivalent, while the integrated $\sqrt{r_1+r_2}$ method performs better close in to the receiver. While there is no testing to validate it, it is proposed that the integrated caustic method should also perform better for large obstructions to the path,
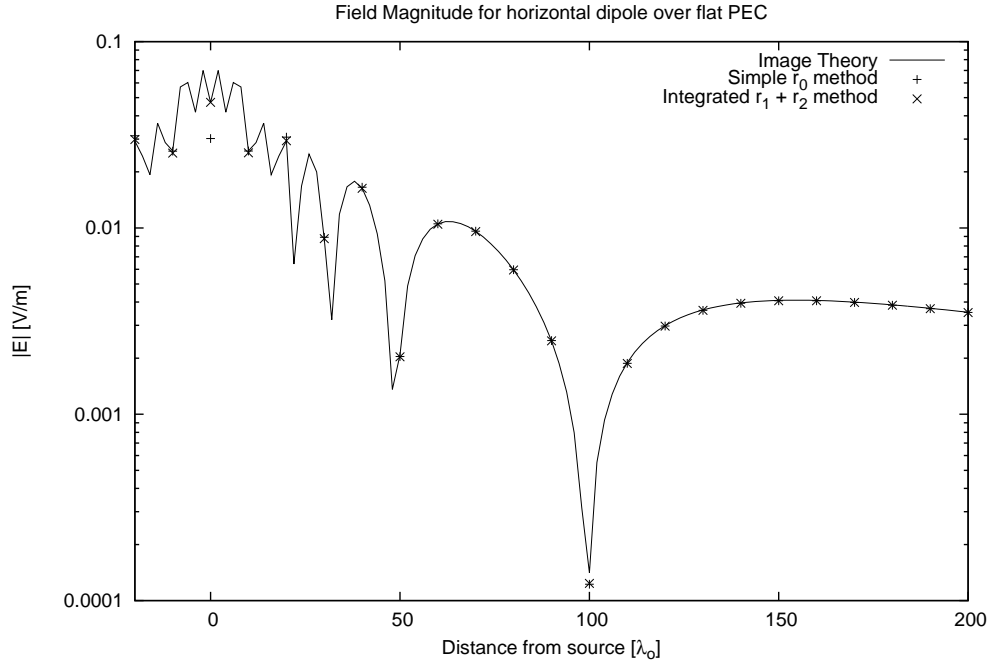
Figure 8.3: Field magnitude for a dipole over a flat surface

where the total distance may vary significantly from the distance directly to the source.

This change to the scattered field necessitates a change to the path loss computation presented in (6.26). As there is no longer a two-dimensional field result, the two dimensional to three dimensional path loss conversion is no longer necessary. Thus, the path loss can be computed directly from the three dimensional power density at the location of interest. For the prior discussion of the conversion of path loss, refer back to section 6.3.1. As such, for values from this point on, the path loss is computed with (6.17) instead of (6.26).

Error in fields for horizontal dipole over flat PEC
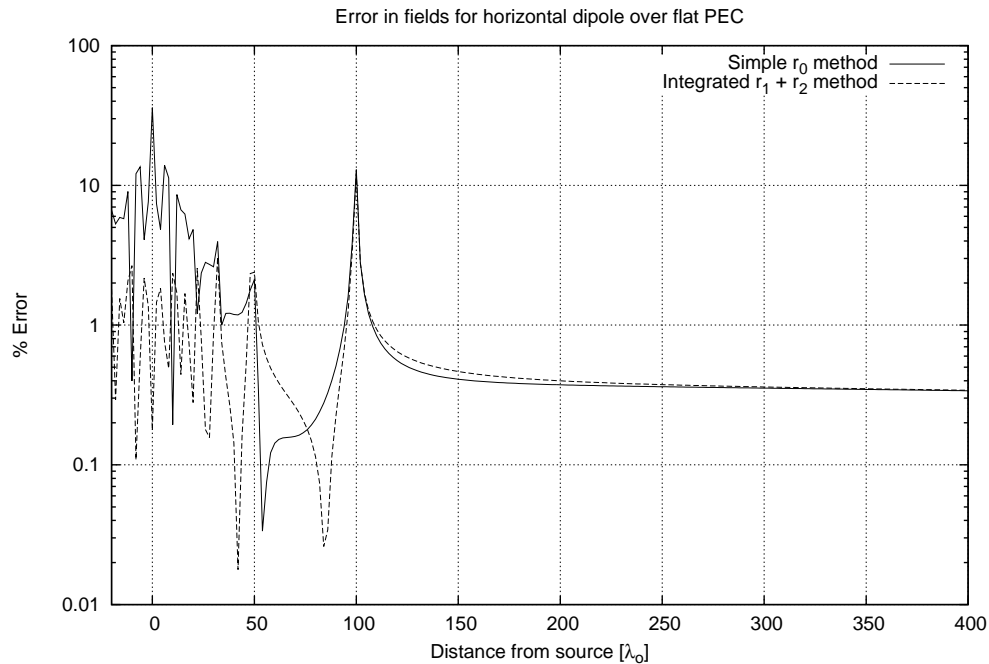
Figure 8.4: Relative error in the field magnitude for a dipole over a flat surface

8.3   Antenna Pattern Inclusion

A secondary problem arises from the analysis presented in Chapter 5. There a bound was shown for the possible error arising from the truncation of the surface in the presence of a line source. That error bound, in equations (5.23) for TM and (5.25) for TE, produces a fairly large error. The bound is predicated on the power radiated beyond the edges of the surface, as well as the power scattered back to the point of observation. Thus, it indicates that by reducing that power level, the error term associated with surface truncation can be reduced.

One approach to this would be to utilize a directional radiator instead of an omni-

directional line source to reduce the power impinging on the edge of the surface closest to the source. Additionally, reducing the effects of the field scattered from beyond the edge could be accomplished by utilizing a directional receiver.

Hufford was the first to do this in the earliest work on using integral equation methods for propagation modeling [84]. In that work, Hufford multiplies the incident field of a point source by the source antenna pattern in the plane of propagation. He also includes the receiving antenna pattern in the scattering integral. The primary difference between Hufford's work and this work is that Hufford did not develop the full integral equation, but assumed only a single forward propagation. Hufford's method was otherwise similar to performing a single $(I - L)$ inversion on the source currents, or a half iteration of MOMI, to obtain the resulting surface currents. Following work by Ott and Berry also utilizes the antenna pattern in the source and scattering, though it also ignores backscatter effects [86, 87, 95].

Therefore, in a further attempt to reduce the error caused by the surface truncation, the source term will be modified with multiplication by the antenna pattern. The patterns which are used are the far field patterns which were measured for the experimental work in Chapter 7. The result is a new source term, which is arrived at by multiplying (B.2a) or (B.3b) by the antenna pattern function $f_s(\phi)$.

$$\mathbf{H}_{TE}(\mathbf{r}) = \hat{\boldsymbol{\phi}}_{\boldsymbol{y}} f_s(\phi_y) \frac{I_e k_0}{4j} H_1^{(2)}(k_0 \rho_y) \tag{8.10}$$

$$\mathbf{H}_{TM}(\mathbf{r}) = -\hat{\mathbf{y}} f_s(\phi_y) \frac{I_m \omega \epsilon}{4} H_0^{(2)}(k_0 \rho_y) \tag{8.11}$$

Equations (8.10) and (8.11) show the source terms used in the TE and TM cases when including an antenna pattern. $\mathbf{H}$ is the magnetic field created by the source, with $H_\nu^{(2)}$ being a Hankel function, ρ_y, ϕ_y, y are the cylindrical coordinate system oriented in the x-z plane, and I_e and I_m the electric and magnetic line current magnitude, respectively.

Additionally, it is necessary to include the receiver antenna pattern in any result, and that pattern should affect the scattering differently accordingly to where it arises. Thus, another term is added to the scattering integral (8.5) for the pattern weighted 3-D scattered field by including the received antenna pattern $f_r(\phi)$.

$$\psi_{scat}^{3D}(\mathbf{r}) = \int_S f_r(\phi)\psi(r')G^{2D}(r,r')\frac{1}{\sqrt{2(r_1+r_2)}}dl' \tag{8.12}$$

This form must be applied to all four of the scattering integrals (8.6 - 8.9). The resulting form of the scattering integrals are shown below for the TE case.

$$\mathbf{H}_{TE}^{3D} = \frac{-jk_0}{4}\int_{S_0}\frac{\hat{\boldsymbol{\beta}}f_r(\beta)}{\sqrt{2(r_1+r_2)}}J(\mathbf{r}_0)H_1^{(2)}(k_0\alpha)\,\mathrm{d}l_0 \tag{8.13}$$

$$\mathbf{E}_{TE}^{3D} = \hat{\mathbf{y}}\frac{\eta k_0}{4}\int_{S_0}\frac{f_r(\beta)}{\sqrt{2(r_1+r_2)}}J(\mathbf{r}_0)H_0^{(2)}(k_0\alpha)\,\mathrm{d}l_0 \tag{8.14}$$

For the TM case, the scattering integrals are:

$$\mathbf{H}_{TM}^{3D} = -\hat{\mathbf{y}}\frac{jk_0}{4}\int_{S_0}\frac{(\hat{\boldsymbol{\beta}}\cdot\hat{\mathbf{s}}_0)f_r(\beta)}{\sqrt{2(r_1+r_2)}}J(\mathbf{r}_0)H_1^{(2)}(k_0\alpha)\,\mathrm{d}l_0 \tag{8.15}$$

$$\begin{aligned}\mathbf{E}_{TM}^{3D} = \frac{\eta k_0}{4}\int_{S_0}&\left[\hat{\boldsymbol{\beta}}(\hat{\boldsymbol{\beta}}\cdot\hat{\mathbf{s}}_0)\left(H_0^{(2)}(k_0\alpha) - \frac{H_1^{(2)}(k_0\alpha)}{k_0\alpha}\right)\right.\\&\left.+\hat{\boldsymbol{\alpha}}(\hat{\boldsymbol{\alpha}}\cdot\hat{\mathbf{s}}_0)\frac{H_1^{(2)}(k_0\alpha)}{k_0\alpha}\right]J(\mathbf{r}_0)\frac{f_r(\beta)}{\sqrt{2(r_1+r_2)}}\mathrm{d}l_0\end{aligned} \tag{8.16}$$

Note that the new scattering integrals above do not produce true electromagnetic fields. The inclusion of the far field antenna pattern in the scattering integral rather produces

a result more akin to what would be observed by an equivalent antenna located at that location. Because of this, the magnitude S resulting from using the above fields in equation (6.14) is no longer a power density in space. It now also includes the received antenna gain, SG_r. Likewise, by including the antenna pattern on the source term, the transmitted power includes the transmitting antenna gain, and is P_tG_t. Therefore, it is not necessary to further alter the path loss function to account for these new terms.

8.3.1   Testing the antenna pattern results

The above assumptions must be tested to assure that they are accurate. The testing proceeded in two stages. First, the flat surface test was repeated with the inclusion of antenna patterns on the transmitter and the receiver. Just as would occur in the case of MOMI for modeling the experiments, the transmitter pattern function is that for the Yagi antenna at 1296 MHz, and the receiver pattern is the log-periodic pattern measured at 1296 MHz. The computations were carried out at 1296 MHz and the results presented in Figure 8.5.

The results show that the pattern multiplication is more significant than the choice of three-dimensional normalizing factor. Both integrated solutions are slightly different from the image theory result. However, the results here are sound enough to continue to testing MOMI with antenna patterns on the actual propagation paths.

Field Magnitude for horizontal patterned dipole over flat PEC
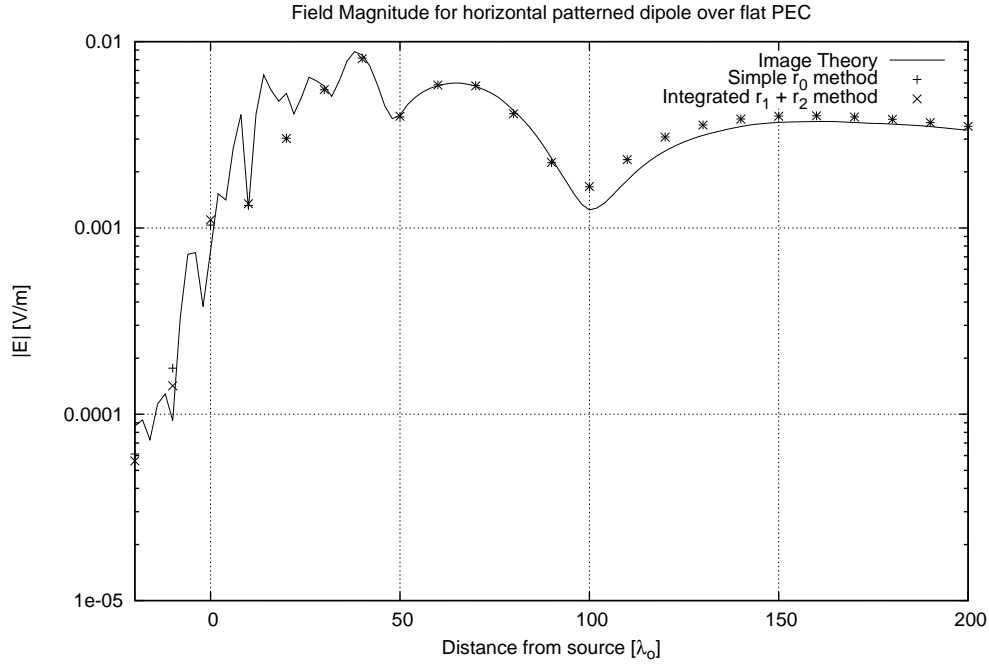
Figure 8.5: Field magnitude for a patterned dipole over a flat surface

8.4 Pattern Multiplied MOMI results

In the previous section, two significant changes were made to the computational method to improve the MOMI results. The first was a change to the scattering integral that resulted in an additional range attenuation factor to better account for the three-dimensional nature of the problem as compared to the two-dimensional nature of MOMI. This change also removed the necessity of the two dimensional to three dimensional path loss adjustment proposed earlier.

The second change was the inclusion of in-plane antenna pattern functions in the incident field as well as the scattering integral. In addition to more closely simulating the experimental

measurements, this method should reduce the impact of the surface truncation. By utilizing a Yagi antenna pattern on the source term, the fields present at the left edge of the surface are reduced by an average of 20 dB as compared to an omni-directional source. The surface truncation error discussion in Chapter 5 implies that this reduction in incident fields should directly reduce any surface truncation error by 20 dB as well.

With these changes made to the methodology, the results of the computations need to be compared to the experimental results. The following sections show the results for the comparisons in all measured cases except for the Horse Ridge to intermediate point paths. These paths are omitted due to the time required to compute the longer paths.

Two factors are highlighted in the results. First is the difference between the measurements and the MOMI computations, the "Δ" column of the data. This is the error between the MOMI prediction and the measured data. The second is the "MOMI σ" column, the standard deviation of the MOMI computations resulting from the topographic data sparsity. In both cases, the analysis focuses on the root mean square of these values across all frequencies and transmitter heights for each polarization and path.

8.4.1   Jack Ball to Jansky Lab

Tables 8.5 and 8.6 show the results for MOMI propagation computations with the new 3D scattering and the use of measured antenna patterns on the source. The results are again compared to the experimental measurements made in the previous chapter. A comparison of

Table 8.5: Comparison of measured data to MOMI with 3D attenuation and antenna patterns for Jack Ball to Jansky Lab for horizontal polarization. (All values except frequency and height are in dB.)

Freq. (MHz)	Tx. Height (ft)	Meas.	Meas. σ	MOMI	MOMI σ	Δ
904	10	-116.11	N/A	-122.07	1.21	-5.96
904	20	-114.33	1.87	-106.51	0.93	7.82
904	30	-112.59	1.03	-106.89	1.25	5.70
926	10	-116.44	N/A	-122.57	1.22	-6.13
926	20	-116.25	1.06	-106.89	1.00	9.36
926	30	-112.69	0.57	-107.66	1.31	5.03
1296	10	-115.13	N/A	-132.16	2.78	-17.03
1296	20	-117.52	2.67	-116.76	2.46	0.76
1296	30	-114.67	2.18	-116.61	2.35	-1.94
2303	10	-132.72	N/A	-134.09	1.75	-1.37
2303	20	-126.47	1.10	-117.12	1.00	9.35
2303	30	-121.36	1.47	-116.08	1.11	5.28
RMS			1.63		1.65	7.59

Table 8.6: Comparison of measured data to MOMI with 3D attenuation and antenna patterns for Jack Ball to Jansky Lab for vertical polarization. (All values except frequency and height are in dB.)

Freq. (MHz)	Tx. Height (ft)	Meas.	Meas. σ	MOMI	MOMI σ	Δ
904	10	-119.51	N/A	-115.97	1.97	3.54
904	20	-115.37	1.82	-108.15	1.12	7.21
904	30	-112.67	0.98	-105.99	0.88	6.68
926	10	-119.54	N/A	-116.35	1.97	3.19
926	20	-116.04	2.45	-108.46	1.14	7.58
926	30	-112.54	0.52	-106.40	0.91	6.14
1296	10	-118.27	N/A	-122.64	1.99	-4.37
1296	20	-118.54	0.23	-113.39	1.08	5.15
1296	30	-115.31	0.57	-112.86	1.04	2.45
2303	10	-130.94	N/A	-130.00	2.54	0.94
2303	20	-127.06	0.19	-117.06	0.95	10.00
2303	30	-121.87	0.59	-116.49	0.90	5.38
RMS			1.19		1.48	5.74

Tables 8.5 and 8.6 with Tables 8.1 and 8.2, shows that the new scattering technique and the inclusion of antenna patterns has a significant positive effect on the prediction. The RMS error improved from 16.8 dB to 7.8 dB for horizontal polarization, and 9.1 dB to 5.7 dB for vertical polarization.

These changes to the technique also result in a reduction in the effect of the randomly rough surface. When the antenna patterns are included, the predicted effect of the 30 meter terrain sampling is an uncertainty of 1.6 dB instead of 2.2 dB for the patternless horizontal polarization results. It is possible that this is because the use of antenna patterns mutes the effect of terrain randomization outside the main beam of the antenna. Without an antenna pattern, randomness in the terrain near the transmitter and receiver could have an effect on the phase of a ground bounce term that may be suppressed by the antenna pattern.

8.4.2   Jack Ball to Intermediate Point 1

The results to the first intermediate point for the Jack Ball transmitter, shown in Tables 8.7 and 8.8, have a similar variability from the terrain randomization as compared to the Jansky Lab receiver results. However, the error with respect to the measurements is higher, 9.1 dB for horizontal polarization and 10.8 dB for vertical polarization. Possible reasons for the error include the use of a broader beam antenna, which may receive more out-of-plane scattering, and heightened foliage obstruction, for which the model does not account.

Table 8.7: Comparison of measured data to MOMI with 3D attenuation and antenna patterns for Jack Ball to intermediate point 1 for horizontal polarization. (All values except frequency and height are in dB.)

Freq. (MHz)	Tx. Height (ft)	Meas.	Meas. σ	MOMI	MOMI σ	Δ
904	20	-121.16	N/A	-116.29	1.57	4.87
904	30	-120.44	0.61	-116.10	1.63	4.34
926	20	-122.09	N/A	-118.23	1.81	3.86
926	30	-120.41	0.53	-116.73	1.71	3.68
1296	20	-130.47	N/A	-118.09	1.40	12.38
1296	30	-127.43	N/A	-116.10	1.39	11.33
2303	20	-138.31	7.61	-125.44	2.68	12.87
2303	30	-133.95	4.82	-122.22	1.91	11.73
RMS			4.52		1.80	9.05

Table 8.8: Comparison of measured data to MOMI with 3D attenuation and antenna patterns for Jack Ball to intermediate point 1 for vertical polarization. (All values except frequency and height are in dB.)

Freq. (MHz)	Tx. Height (ft)	Meas.	Meas. σ	MOMI	MOMI σ	Δ
904	20	-121.56	N/A	-111.71	1.17	9.85
904	30	-120.23	0.06	-111.12	1.18	9.11
926	20	-124.38	N/A	-111.77	1.25	12.61
926	30	-120.46	1.63	-111.70	1.29	8.76
1296	20	-131.13	N/A	-117.41	1.83	13.72
1296	30	-129.13	N/A	-116.81	1.80	12.32
2303	20	-133.23	N/A	-122.50	2.13	10.73
2303	30	-129.55	N/A	-121.96	2.18	7.59
RMS			1.16		1.65	10.77

8.4.3   Jack Ball to Water Tower

Table 8.9: Comparison of measured data to MOMI with 3D attenuation and antenna patterns for Jack Ball to Water Tower for horizontal polarization. (All values except frequency and height are in dB.)

Freq. (MHz)	Tx. Height (ft)	Meas.	Meas. σ	MOMI	MOMI σ	Δ
904	10	-98.41	N/A	-102.25	1.31	-3.84
904	20	-102.30	N/A	-99.48	1.08	2.82
904	30	-101.41	N/A	-98.20	0.78	3.21
926	10	-98.81	N/A	-101.11	1.43	-2.30
926	20	-102.30	N/A	-103.29	1.27	-0.99
926	30	-102.73	N/A	-100.99	1.17	1.74
1296	10	-107.63	N/A	-100.95	1.00	6.68
1296	20	-103.97	N/A	-105.91	2.07	-1.94
1296	30	-105.05	0.17	-103.96	1.39	1.09
2303	10	-106.61	N/A	-107.14	2.60	-0.53
2303	20	-110.23	N/A	-112.02	4.82	-1.79
2303	30	-109.38	N/A	-106.79	1.71	2.59
RMS			0.17		2.01	2.92

The water tower measurements and computations are key for model validation because the line-of-sight path to the Jack Ball transmitter is the only unobstructed set of measurements that were made. The water tower results are shown in Tables 8.9 and 8.10. The error of the computed results to the measurements is only 2.9 dB for horizontal polarization and 2.2 dB for vertical polarization. The MOMI propagation computations do not account for foliage, reflections off the tower structure, or out-of-plane scattering. Considering those limitations, and that the water tower measurements were made with the broader beam log-

Table 8.10: Comparison of measured data to MOMI with 3D attenuation and antenna patterns for Jack Ball to Water Tower for vertical polarization. (All values except frequency and height are in dB.)

Freq. (MHz)	Tx. Height (ft)	Meas.	Meas. σ	MOMI	MOMI σ	Δ
904	10	-100.93	N/A	-100.47	0.95	0.46
904	20	-101.27	N/A	-101.74	1.06	-0.47
904	30	-101.27	0.99	-103.04	1.32	-1.77
926	10	-100.35	N/A	-102.92	1.32	-2.57
926	20	-103.08	N/A	-102.31	1.17	0.77
926	30	-101.68	1.77	-100.76	1.10	0.92
1296	10	-107.03	N/A	-101.72	0.78	5.31
1296	20	-104.50	N/A	-103.00	0.93	1.50
1296	30	-105.57	N/A	-104.62	1.10	0.95
2303	10	-105.41	N/A	-108.17	1.72	-2.76
2303	20	-109.38	N/A	-109.07	1.68	0.31
2303	30	-109.73	N/A	-107.38	1.56	2.35
RMS			1.43		1.26	2.16

periodic antenna, the accuracy of the prediction for a path of nearly three kilometers at gigahertz frequencies is a good sign for the validity of the MOMI computational method. While the line-of-sight data is limited for this work, the TIREM model is only accurate to within 8.9 dB for line-of-sight paths (though it was tested over far more measurements) [97]. This is especially true when the computations estimate that 1 dB to 2 dB of the error can be accounted for by the sparsity of the thirty meter topographic data.

In general, examination of the water tower results shows that the worst predictions occurred for the ten foot transmitter height cases. This trend is less clear in other data sets; however, this path has the fewest complicating factors. The error may be greater for this height because the model does not account for coupling between the antenna and the ground. Such coupling would be more significant as the transmitter approaches the ground.

8.4.4   Horse Ridge to Jansky Lab

The last of the 2009 experimental results are presented in Tables 8.11 and 8.12. These tables show the comparison of computations for the Horse Ridge to Jansky Lab path with the experimental measurements. The limited number of results is due to a reduced number of measuremnt configurations. Generally, experimental measurements were limited to the thirty foot transmitter height because of the low overall signal levels. Considering the length and the heavily obstructed nature of the path, the 4.9 dB error in the computations compared to the measurements is good. This compares to an error level of 4.7 dB in Tables 8.3 and 8.4,

Table 8.11: Comparison of measured data to MOMI with 3D attenuation and antenna patterns for Horse Ridge to Jansky Lab for horizontal polarization. (All values except frequency and height are in dB.)

Freq. (MHz)	Tx. Height (ft)	Meas.	Meas. σ	MOMI	MOMI σ	Δ
904	30	-142.27	1.55	-148.91	1.55	-6.64
926	10	-145.27	N/A	-150.25	1.93	-4.98
926	20	-144.94	N/A	-150.94	2.23	-6.00
926	30	-142.71	1.22	-149.86	1.89	-7.15
1296	10	-160.31	N/A	-156.61	2.19	3.70
1296	20	-154.72	N/A	-154.88	1.61	-0.16
1296	30	-155.32	1.64	-155.40	1.65	-0.08
RMS			1.48		1.88	4.92

Table 8.12: Comparison of measured data to MOMI with 3D attenuation and antenna patterns for Horse Ridge to Jansky Lab for vertical polarization. (All values except frequency and height are in dB.)

Freq. (MHz)	Tx. Height (ft)	Meas.	Meas. σ	MOMI	MOMI σ	Δ
904	30	-142.78	0.84	-145.57	1.72	-2.79
926	30	-142.22	1.07	-146.87	2.03	-4.65
1296	20	-156.14	N/A	-150.95	1.56	5.19
1296	30	-156.76	0.54	-150.59	1.48	6.17
RMS			0.85		1.71	4.86

showing the results without antenna patterns or changes to the scattering computations. At least for the long distance Horse Ridge path, the methodology changes had little effect on the overall accuracy.

Additionally, while this is the longest path, the uncertainty introduced by the randomization of the MOMI paths is not significantly different from that computed for the shorter paths. The small variation in the MOMI computed standard deviations suggest that, at least for the paths computed, the length of the path does not significantly alter the effect the topographic data sparsity.

8.4.5   Short North 2 to Jansky Lab

The path between Short North 2 and Jansky Lab, the shortest path in this study, was chosen because it has a single grazing obstruction. However, the obstruction is heavily foliated. Tables 8.13 and 8.14 show the results for the Short North 2 path. These are striking results, with a large consistent bias of about 22 dB in the horizontal polarization results and 25 dB for vertical polarization. Removing the bias results in an RMS error of 6.3 dB for horizontal and 4.0 dB for vertical polarization. The bias is assumed to be a result of the foliage atop the obstacle. With the foliage present, the obstacle clearly blocks the line-of-sight, while the topographic data suggests the path is just barely obstructed. The other factor with the data is that the MOMI results show only 0.9 dB and 0.8 dB of variation due to the topographic data sparsity. Even the line-of-sight Jack Ball to water tower path had a larger variation.

Table 8.13: Comparison of measured data to MOMI with 3D attenuation and antenna patterns for Short North 2 to Jansky Lab with horizontal polarization. (All values except frequency and height are in dB.)

Freq. (MHz)	Tx. Height (ft)	Meas.	MOMI	MOMI σ	Δ
904	10	-121.30	-101.28	0.88	20.02
904	20	-116.84	-100.29	0.89	16.55
904	30	-116.56	-96.24	0.64	20.32
926	10	-123.81	-101.59	0.92	22.22
926	20	-120.80	-100.75	0.96	20.05
926	30	-121.68	-96.63	0.73	25.05
1296	10	-121.88	-105.71	1.15	16.17
1296	20	-121.72	-104.33	0.96	17.39
1296	30	-121.03	-101.68	0.91	19.35
1296	40	-119.42	-102.24	1.12	17.18
2303	10	-145.84	-113.85	1.24	31.99
2303	20	-140.35	-109.32	0.95	31.03
2303	30	-141.28	-104.78	0.85	36.50
RMS				0.95	23.47

Table 8.14: Comparison of measured data to MOMI with 3D attenuation and antenna patterns for Short North 2 to Jansky Lab with vertical polarization. (All values except frequency and height are in dB.)

Freq. (MHz)	Tx. Height (ft)	Meas.	MOMI	MOMI σ	Δ
904	10	-134.26	-103.72	0.96	30.54
904	20	-122.38	-99.71	0.77	22.67
904	30	-123.02	-98.05	0.74	24.97
904	40	-119.32	-96.09	0.57	23.23
926	10	-131.18	-104.01	0.98	27.17
926	20	-129.37	-100.05	0.78	29.32
926	30	-127.06	-98.19	0.72	28.87
926	40	-119.63	-96.08	0.57	23.55
1296	10	-123.82	-105.87	0.89	17.95
1296	20	-124.23	-103.65	0.92	20.58
1296	30	-127.81	-101.19	0.87	26.62
2303	10	-135.51	-113.82	0.99	21.69
2303	20	-136.96	-108.88	0.79	28.08
2303	30	-137.07	-104.83	0.72	32.24
RMS				0.82	25.84

Further study would be required to understand the reason for the low level of variation caused by the terrain uncertainty in this case.

This demonstrates a significant problem with the use of pure topographic data. In this particular case, information on foliage, which is not contained in the USGS data, would be required to produce an accurate prediction. Additionally, MOMI would need to be modified to account for the foliage, perhaps with the inclusion of a lossy dielectric foliage layer over the ground layer.

8.4.6   Bear Mountain to Jansky Lab

Table 8.15: Comparison of measured data to MOMI with 3D attenuation and antenna patterns for Bear Mountain to Jansky Lab with horizontal polarization. (All values except frequency and height are in dB.)

Freq. (MHz)	Tx. Height (ft)	Meas.	MOMI	MOMI σ	Δ
904	20	-182.78	-163.35	3.69	19.43
904	30	-177.35	-164.10	3.75	13.25
926	20	-172.45	-155.04	2.29	17.41
926	30	-164.46	-167.56	5.70	-3.10
1296	20	-169.31	-158.37	1.53	10.94
1296	30	-175.31	-160.43	2.22	14.88
2303	20	-165.97	-155.23	0.64	10.74
RMS				3.23	13.74

The Bear Mountain to Jansky Lab path had relatively few experimental measurements taken, with measurements focusing on 20 ft. and 30 ft. transmitter heights. The comparison

Table 8.16: Comparison of measured data to MOMI with 3D attenuation and antenna patterns for Bear Mountain to Jansky Lab with vertical polarization. (All values except frequency and height are in dB.)

Freq. (MHz)	Tx. Height (ft)	Meas.	MOMI	MOMI σ	Δ
904	20	-167.66	-144.11	2.06	23.55
904	30	-163.91	-144.57	1.93	19.34
926	20	-163.51	-146.91	2.77	16.60
926	30	-159.43	-147.89	2.14	11.54
1296	20	-171.72	-152.83	4.16	18.89
1296	30	-160.50	-149.60	1.91	10.90
2303	20	-170.00	-155.07	2.28	14.93
RMS				2.57	17.05

of measurements to MOMI results is shown in Tables 8.15 and 8.16. The eleven kilometer path has a single bare ridge-line obstruction on the direct path. However, foliage is present just below the ridge on both sides. This may be the cause of some of the 13.7 dB of error in the horizontal polarization case and the 17.1 dB of error in vertical polarization. There is a bias in the MOMI results of 12 dB for horizontal polarization and 16 dB for vertical polarization compared to the measurements, similar to the Short North 2 results, although smaller in magnitude. Additionally, MOMI computes 2.5 - 3.2 dB of variation due to the topographic data. This is a larger level of uncertainty than for any of the prior paths examined, but is comparable to the level that will be seen in the remaining paths.

Table 8.17: Comparison of measured data to MOMI with 3D attenuation and antenna patterns for Watering Pond Knob to Jansky Lab with horizontal polarization. (All values except frequency and height are in dB.)

Freq. (MHz)	Tx. Height (ft)	Meas.	MOMI	MOMI σ	Δ
904	20	-151.67	-164.54	2.95	-12.87
904	30	-151.58	-168.66	3.93	-17.08
926	20	-162.73	-163.87	3.69	-1.14
926	30	-160.11	-170.72	4.85	-10.61
1296	20	-149.38	-159.28	1.83	-9.90
1296	30	-150.55	-159.17	1.53	-8.62
2303	20	-158.35	-180.58	4.97	-22.23
2303	30	-156.35	-181.38	5.19	-25.03
RMS				3.85	15.27

Table 8.18: Comparison of measured data to MOMI with 3D attenuation and antenna patterns for Watering Pond Knob to Jansky Lab with vertical polarization. (All values except frequency and height are in dB.)

Freq. (MHz)	Tx. Height (ft)	Meas.	MOMI	MOMI σ	Δ
904	20	-155.39	-148.80	3.74	6.59
904	30	-156.48	-144.97	1.90	11.51
926	20	-160.60	-157.54	2.10	3.06
926	30	-164.54	-158.96	2.39	5.58
1296	20	-155.80	-152.81	2.32	2.99
1296	30	-155.46	-151.36	2.16	4.10
2303	20	-156.98	-167.09	2.68	-10.11
2303	30	-156.48	-166.38	2.56	-9.90
RMS				2.54	7.44

8.4.7   Watering Pond Knob to Jansky Lab

The Watering Pond Knob to Jansky Lab path is approximately ten kilometers long and diffracts across two bare ridges. Tables 8.17 and 8.18 compare the MOMI computations to the experimental measurements for horizontal and vertical polarizations. The RMS path loss variation due to the terrain variation is about 2.5 dB for vertical polarization, as with the Bear Mountain path. For horizontal polarization, it is even higher, at about 3.9 dB.

For this path, the MOMI results are not consistently biassed between the polarizations. The vertical polarization MOMI results have a small bias, whereas in horizontal polarization, MOMI consistently overestimates the path loss. This is the only case where MOMI largely computed more loss than was actually measured, although the Horse Ridge horizontal polarization results also showed a small bias in this direction. Additionally, the 15 dB of error at horizontal polarization is the only case that large for paths without significant foliage obstructing the propagation path. It is possible that this path is one with significant out-of-plane scattering, with a non-direct path producing higher power than predicted for the over-ridge diffraction.

8.4.8   Watering Pond North to Jansky Lab

The last set of results is that for the transmission from Watering Pond North to Jansky Lab. The comparison of computations to experimental measurements is shown in Tables 8.19 and 8.20. The WPN path is also approximately 10 kilometers, and diffracts across the same

Table 8.19: Comparison of measured data to MOMI with 3D attenuation and antenna patterns for Watering Pond North to Jansky Lab with horizontal polarization. (All values except frequency and height are in dB.)

Freq. (MHz)	Tx. Height (ft)	Meas.	MOMI	MOMI σ	Δ
904	20	-156.76	-156.45	2.74	0.31
904	30	-152.44	-156.16	3.23	-3.72
926	20	-153.25	-164.69	4.85	-11.45
926	30	-149.11	-158.70	3.07	-9.59
1296	20	-153.49	-149.03	1.62	4.46
2303	20	-159.69	-169.62	5.21	-9.93
2303	30	-162.64	-171.85	4.53	-9.21
RMS				3.80	7.93

Table 8.20: Comparison of measured data to MOMI with 3D attenuation and antenna patterns for Watering Pond North to Jansky Lab with vertical polarization. (All values except frequency and height are in dB.)

Freq. (MHz)	Tx. Height (ft)	Meas.	MOMI	MOMI σ	Δ
904	20	-151.85	-152.09	4.83	-0.24
904	30	-148.98	-141.95	1.68	7.03
926	30	-146.07	-143.95	2.15	2.12
1296	20	-162.54	-147.01	2.43	15.53
1296	30	-157.70	-147.41	3.64	10.29
2303	20	-160.43	-160.42	3.93	0.01
2303	30	-163.28	-156.55	3.34	6.73
RMS				3.31	7.98

double ridgeline as the WPK path. As with the BM and WPK paths, the path loss variation due to the topographic data sparsity, as computed by MOMI, is large relative to the other paths. However, the error between the MOMI computation and the measured data is only about 8.0 dB for both polarizations. This is fairly consistent with other obstructed paths.

8.5   Summary of all results

The initial MOMI results showed a higher error level than was originally expected. Therefore, several changes were made to the method to improve the accuracy. The first change was to alter the method of computing the scattered fields to better account for the discrepancy between the two-dimensional MOMI computation and the three-dimensions of real space. The second change was the inclusion of antenna patterns for both the transmitter and the receiver. The inclusion of antenna patterns makes the computations more closely match the physical problem, while also aiding in reducing the effects of surface truncation.

After describing the changes to the methodology, full results were presented for the comparison of MOMI to the experimental measurements made in Chapter 7. The computational results suggest that the sampling rate of topographic data is more important for the heavily obscured paths than for line-of-sight or near line-of-sight paths. Considering paths from JB and SN2 as near line-of-sight or line-of-sight, the combined standard deviation of computed results produces an estimate of ± 1.5 dB variation resulting from the topographic data being sampled at 30 meters. Classifying the HR, BM, WPK, and WPN paths as heavily obscured,

the composite standard deviation is 2.9 dB of error resulting from the topographic data.

Additionally, the results of the SN2 path suggest that foliage is a concern which cannot be neglected for accurate computation of path loss. The foliated obstacle of SN2 resulted in an additional 10 dB of error as compared to the other computations. The RMS error when comparing all computations to all measurements is 12.9 dB for horizontal polarization and 13.8 dB for vertical polarization. If the outlier SN2 data is excluded, the result is an error of 9.3 dB for horizontal and 8.7 dB for vertical polarization. MOMI had an overall bias of 4 dB for horizontal polarization, and 9 dB for vertical polarization. However, when the outlier Short North 2 path, with heavy foliage, was eliminated, there was no bias for horizontal polarization and 5 dB of bias for vertical polarization.

As a comparison, consider TIREM, a hybrid model utilizing both empirical estimates of loss and analytic approximations of diffraction and atmospheric refraction. TIREM has an error of 8.9 dB for line-of-sight paths and 11.4 dB for diffraction paths [97]. Thus, even with the SN2 measurements included, MOMI, with no method of accounting for foliage, is nearly as accurate as TIREM. The inclusion of a method for dealing with foliage would likely make the MOMI results even better, as foliage is present in all the tested paths. However, MOMI is much more computationally intensive than methods such as TIREM, and would become even more so with the inclusion of other factors.

Chapter 9

Conclusion

As mentioned in the introduction, point-to-point propagation models usually rely on topographic databases to provide a profile of the terrain under the transmission path [2]. Those databases are generally sampled at intervals much larger than the electromagnetic wavelength for typical radio communication systems. Because of this, it is impossible for the propagation models to be completely accurate.

The goal of this thesis is to present a method for estimating the uncertainty introduced into radio transmission propagation models that result from this sparse sampling of topographical data. To that end, the previous chapters present a method for using MOMI to compute path loss over many randomly rough surfaces combined with a spline surface fit to topographic data. The results allow the estimation of the effects of the unknown terrain variation between the sample points of the topographic data.

Chapters 2 to 4 reviewed the previous work done in radio propagation measurement and modelling, the production of electric and magnetic fields from sources, and the development of the MFIE and MOMI. That material covers the techniques used for propagation computations in later chapters.

Using the techniques developed in those chapters, Chapter 5 shows the computation of a loose bound on the error resulting from truncating the surface scattering region for a flat surface. This new bound does not provide strict guidance on surface trunctation, but it does show that the error is limited if the source and observation points are both located over the surface and away from the edges of the surface.

Chapter 6 contains a mix of prior work and new material. While the method for computating path loss is based on previous authors' work, the combination of a randomly rough surface generated from a roughness spectrum with a smooth spline is new. This chapter also lays out the full Monte-Carlo method which is used to compute the propagation loss error due to the topographical data sampling interval. Thus, Chapter 6 presents the methodology that was stated as the goal of the thesis.

Chapter 7 covers the methodology for, and results of, a set of radio propagation measurements made in the vicinty of Green Bank, West Virigia. The measurements, taken in a mountainous environment, provide data at frequencies between 900 MHz and 2.3 GHz, for obstructed paths around mountains. Such measurements are generally lacking in the literature to date. The measurements are then used in Chapter 8 to validate the MOMI computational results and show that the MOMI method is a sound propagation model.

Chapter 8 also shows several minor improvements made to the computational method after the fit to the first set of measurements was not satisfactory, and the final comparison of the MOMI method to experimental measurements.

With the finaly changes made to the methodology, MOMI had a bias of underestimating the loss by 4 dB for horizontal polarization, and 9 dB for vertical polarization. However, when the outlier Short North 2 path, with heavy foliage, was eliminated, there was no bias for horizontal polarization and 5 dB of bias for vertical polarization. For all paths, the standard deviation between MOMI results and measurments is 13 dB. Excluding the Short North 2 path, this drops to 9 dB. This shows that MOMI is as good as other methods at predicting propagation loss [97], though future improvements should address the problem of foliage.

Presented along with the comparison to the measurements is the inclusion of the standard deviation of the MOMI results due to the randomly rough surface components. This result, which is shown for multiple paths individually in Chapter 8, was the reason for using a full wave technique for propagation modelling. While several cases are broken out at the end of the previous chapter, the overall result is that for 30 meter terrain data over all paths studied, computations suggests that 2.3 dB of error accounted for by the topographic sampling interval. However, this number is based on the assumptions made about the roughness of the terrain between the sampled data values. Future work should address this by examining the effects of different roughness spectra on the propagation results.

The area of propagation modeling is ripe for future improvements. Point-to-point model improvements such as the inclusion of out-of-plane scattering and the effects of ground

cover would likely improve many models. Additional areas for future progress also include examinination of the effects of other roughness spectra and topographic dataset spacing intervals. Additionally, the effect of topographic database accuracy has not been evaluated. Future work could also include the study of changes in the dielectric constant of the ground instead of relying on a perfectly conducting ground.

Bibliography

[1] A. B. Carlson, P. B. Crilly, and J. C. Rutledge, *Communication Systems.* Boston: McGraw-Hill, Inc., 2002.

[2] J. Seybold, *Introduction to RF Propagation.* John Wiley & Sons, 2005.

[3] D. Gesch, *Digital Elevation Model Technologies and Applications: The DEM Users Manual*, ch. The National Elevation Dataset, pp. 99–118. Bethesda, Maryland: American Society for Photogrammetry and Remote Sensing, 2nd ed., 2007.

[4] J. A. Ogilvy, *Theory of Wave Scattering from Random Rough Surfaces.* Adam Hilger, 1991.

[5] P. Beckman and A. Spizzichino, *The Scattering of Electromagnetic Waves from Rough Surfaces.* Oxford: Pergamon Press, 1963.

[6] M. Abramowitz and I. A. Stegun, eds., *Handbook of Mathematical Functions with Formulas, Graphs, and Mathematical Tables.* New York: Dover Publications Inc., December 1972.

[7] R. F. Harrington, *Time-Harmonic Electromagnetic Field.* New York: McGraw-Hill, Inc., 1961.

[8] A. Peterson, S. L. Ray, and R. Mittra, *Computational Methods for Electromagnetics.* New York: IEEE Press, 1998.

[9] D. A. Kapp and G. S. Brown, "A new numerical method for rough-surface scattering calculations," *Antennas and Propagation, IEEE Transactions on*, vol. 44, pp. 711–721, May 1996.

[10] J. C. Maxwell, "A dynamical theory of the electromagnetic field," *Philosophical Transactions of the Royal Society of London*, vol. 155, pp. 459–512, 1865.

[11] H. Hertz, *Electric Waves Being Researches on the Propagation of Electric Action with Finite Velocity Through Space.* New York: Dover Publications Inc., 1893. Translated by Jones, D. E.

[12] G. Marconi, "Wireless telegraphy," *Electrical Engineers, Journal of the Institution of*, vol. 28, pp. 273 –290, April 1899.

[13] G. Marconi, "Transatlantic wireless telegraphy," *Nature*, vol. 80, pp. 233–237, April 1909.

[14] G. Marconi, "Radio-telegraphy," *Nature*, vol. 86, pp. 600–605, June 1911.

[15] S. Marconi, "Radio telegraphy," *Proceedings of the Institute of Radio Engineers*, vol. 10, pp. 215 – 238, August 1922.

[16] S. Marconi, "Radio communications," *Engineering*, pp. 543–544, 587, October 1926.

[17] S. Marconi, "Radio communication," *Proceedings of the Institute of Radio Engineers*, vol. 16, pp. 40 – 69, January 1928.

[18] R. Barfield, "The attenuation of wireless waves over land," *Electrical Engineers, Journal of the Institution of*, vol. 66, pp. 204 –214, February 1928.

[19] R. Barfield and G. Munro, "The attenuation of wireless waves over towns," *Electrical Engineers, Journal of the Institution of*, vol. 67, pp. 253 –265, February 1929.

[20] S. Kirby and K. Norton, "Field intensity measurements at frequencies from 285 to 5400 kilocycles per second," *Proceedings of the Institute of Radio Engineers*, vol. 20, pp. 841 – 862, May 1932.

[21] C. Feldman, "The optical behavior of the ground for short radio waves," *Proceedings of the Institute of Radio Engineers*, vol. 21, pp. 764 – 801, June 1933.

[22] B. Trevor and P. Carter, "Notes on propagation of waves below ten meters in length," *Proceedings of the Institute of Radio Engineers*, vol. 21, pp. 387 – 426, March 1933.

[23] C. Englund, A. Crawford, and W. Mumford, "Further results of a study of ultra-short-wave transmission phenomena," *Bell System Technical Journal*, vol. 14, pp. 369–387, July 1935.

[24] C. Burrows, A. Decino, and L. Hunt, "Ultra-short-wave propagation over land," *Proceedings of the Institute of Radio Engineers*, vol. 23, pp. 1507 – 1535, December 1935.

[25] P. Carter and G. Wickizer, "Ultra-high-frequency transmission between the RCA building and the Empire State Building in New York City," *Proceedings of the Institute of Radio Engineers*, vol. 24, pp. 1082 – 1094, August 1936.

[26] K. MacLean and G. Wickizer, "Notes on the random fading of 50-megacycle signals over nonoptical paths," *Proceedings of the IRE*, vol. 27, pp. 501 – 506, August 1939.

[27] G. Wickizer, "Field-strength survey, 52.75 megacycles from Empire State Building," *Proceedings of the IRE*, vol. 28, pp. 291 – 296, July 1940.

[28] J. McPetrie and J. Saxton, "An experimental investigation of the propagation of radiation having wavelengths of 2 and 3 metres," *Electrical Engineers, Journal of the Institution of*, vol. 87, pp. 146 –153, August 1940.

[29] A. Friend, "A summary and interpretation of ultra-high-frequency wave-propagation data collected by the late Ross A. Hull," *Proceedings of the IRE*, vol. 33, pp. 358 – 373, June 1945.

[30] R. Smith-Rose, "Radio-wave propagation research in the department of scientific and industrial research during the years 1937–1946," *Electrical Engineers - Part IIIA: Radiocommunication, Journal of the Institution of*, vol. 94, pp. 879 –892, March-April 1947.

[31] K. Norton, "Radio-wave propagation during World War II," *Proceedings of the IRE*, vol. 50, pp. 698 –704, May 1962.

[32] J. McPetrie and L. Ford, "An experimental investigation on the propagation of radio waves over bare ridges in the wavelength range 10 cm to 10 m," *Electrical Engineers - Part IIIA: Radiolocation, Journal of the Institution of*, vol. 93, no. 3, pp. 527 –530, 1946.

[33] J. McPetrie and L. Ford, "Some experiments on the propagation over land of radiation of 9.2-cm wavelength, especially on the effect of obstacles," *Electrical Engineers - Part IIIA: Radiolocation, Journal of the Institution of*, vol. 93, no. 3, pp. 531 –538, 1946.

[34] G. Mueller, "Propagation of 6-millimeter waves," *Proceedings of the IRE*, vol. 34, pp. 181p – 183p, April 1946.

[35] J. Allen, E.W., "Very-high-frequency and ultra-high-frequency signal ranges as limited by noise and co-channel interference," *Proceedings of the IRE*, vol. 35, pp. 128 – 136, February 1947.

[36] G. Wickizer and A. Braaten, "Propagation studies on 45.1, 474, and 2800 megacycles within and beyond the horizon," *Proceedings of the IRE*, vol. 35, pp. 670 – 680, July 1947.

[37] M. Katzin, R. Bauchman, and W. Binnian, "3- and 9-centimeter propagation in low ocean ducts," *Proceedings of the IRE*, vol. 35, pp. 891 – 905, September 1947.

[38] G. H. Brown, J. J. Epstein, and D. W. Peterson, "Comparative propagation measurements; television transmitters at 67.25, 288, 510, and 910 megacycles," *RCA Review*, vol. 9, pp. 177–201, June 1948.

[39] A. Durkee, "Results of microwave propagation tests on a 40-mile overland path," *Proceedings of the IRE*, vol. 36, pp. 197 – 205, February 1948.

[40] J. Saxton, "The propagation of metre radio waves beyond the normal horizon. part 1: Some theoretical considerations, with particular reference to propagation over land," *Electrical Engineers, Journal of the Institution of*, vol. 1951, p. 272, September 1951.

[41] J. Saxton, G. Luscombe, and G. Bazzard, "The propagation of metre radio waves beyond the normal horizon. part 2: Experimental investigations at frequencies of 90 and 45 Mc/s," *Proceedings of the IEE - Part III: Radio and Communication Engineering*, vol. 98, pp. 370 –378, September 1951.

[42] H. Kirke, R. Rowden, and G. Ross, "A v.h.f. field-strength survey on 90 mc/s," *Proceedings of the IEE - Part III: Radio and Communication Engineering*, vol. 98, pp. 343 –359, September 1951.

[43] W. R. Young, "Comparison of mobile radio transmission at 150, 450, 900, and 3700 Mc," *Bell System Technical Journal*, vol. 31, pp. 1068–1085, November 1952.

[44] A. Crawford and W. Jakes, "Selective fading of microwaves," *Bell System Technical Journal*, vol. 31, pp. 68–90, January 1952.

[45] F. Dickson, J. Egli, J. Herbstreit, and G. Wickizer, "Large reductions of vhf transmission loss and fading by the presence of a mountain obstacle in beyond-line-of-sight paths," *Proceedings of the IRE*, vol. 41, pp. 967 –969, August 1953.

[46] K. Bullington, "Radio propagation variations at vhf and uhf," *Proceedings of the IRE*, vol. 38, pp. 27 – 32, January 1950.

[47] K. Bullington, "Radio transmission beyond the horizon in the 40-to 4,000-mc band," *Proceedings of the IRE*, vol. 41, pp. 132 –135, January 1953.

[48] K. Bullington, "Reflection coefficients of irregular terrain," *Proceedings of the IRE*, vol. 42, pp. 1258 –1262, August 1954.

[49] K. Bullington, W. Inkster, and A. Durkee, "Results of propagation tests at 505 mc and 4,090 mc on beyond-horizon paths," *Proceedings of the IRE*, vol. 43, pp. 1306 –1316, October 1955.

[50] K. Bullington, A. Durkee, and W. Inkster, "Results of propagation test at 505 mc and 4090 mc on beyond horizon paths," *Communications Systems, IRE Transactions on*, vol. 4, pp. 104 –111, March 1956.

[51] L. P. Rice, "Radio transmission into buildings at 35 and 150 mc," *Bell System Technical Journal*, vol. 38, pp. 197–210, January 1959.

[52] E. Hagg and W. Rolfe, "A study of transatlantic radio propagation modes at 41.5 mc/s," *Canadian Journal of Physics*, vol. 41, pp. 220–233, 1963.

[53] J. Ossanna, "A model for mobile radio fading due to building reflections: Theoretical and experimental fading waveform power spectra," *Bell System Technical Journal*, vol. 43, pp. 2935–2971, November 1964.

[54] H. Nylund, "Characteristics of small-area signal fading on mobile circuits in the 150 mhz band," *Vehicular Technology, IEEE Transactions on*, vol. 17, pp. 24 – 30, October 1968.

[55] K. Allsebrook and J. Parsons, "Mobile radio propagation in british cities at frequencies in the vhf and uhf bands," *Proceedings of the IEE*, vol. 124, pp. 95–102, February 1977.

[56] J. Parsons, M. F. Ibrahim, and R. J. Holbech, "Mobile radio propagation in rural areas at 168, 455, and 896 MHz," *Proceedings of the IEE*, vol. 130, pp. 701–706, December 1983.

[57] S. Durden, J. Klein, and H. Zebker, "Measurement and simulation of signal fluctuations caused by propagation through trees," *Radio Science*, vol. 28, pp. 1049–1051, November 1993.

[58] F. Owen and C. Pudney, "Radio propagation for digital cordless telephones at 1700 MHz and 900 MHz," *Electronics Letters*, vol. 25, pp. 52 – 3, January 1989.

[59] Y. Zhang, T. Ng, G. Zheng, J. Sheng, and Y. Wang, "Radio propagation within coal mine longwall faces at 900 MHz," *Microwave and Optical Technology Letters*, vol. 18, pp. 184–187, June 1998.

[60] S.-C. Kim, J. Guarino, B.J., I. Willis, T.M., V. Erceg, S. Fortune, R. Valenzuela, L. Thomas, J. Ling, and J. Moore, "Radio propagation measurements and prediction using three-dimensional ray tracing in urban environments at 908 mhz and 1.9 ghz," *Vehicular Technology, IEEE Transactions on*, vol. 48, pp. 931 –946, May 1999.

[61] J.-V. Rodriguez, S. G. Martinez, C. Garcia-Pardo, J.-M. Molina-Garcia-Pardo, and L. Juan-Llacer, "Comparison of various urban radiowave propagation models with measurements," *IEEE Antennas and Wireless Propagation Letters*, vol. 8, pp. 977 – 980, 2009.

[62] T. Rao, S. Rao, M. Prasad, M. Sain, A. Iqbal, and D. Lakshmi, "Mobile radio propagation path loss studies at vhf/uhf bands in southern India," *Broadcasting, IEEE Transactions on*, vol. 46, pp. 158 –164, June 2000.

[63] N. Savage, D. Ndzi, A. Seville, E. Vilar, and J. Austin, "Radio wave propagation through vegetation: factors influencing signal attenuation," *Radio Science*, vol. 38, pp. 9 – 1, September 2003.

[64] K. Bullington, "Radio propagation fundamentals," *Bell System Technical Journal*, vol. 36, pp. 593–626, May 1957.

[65] H. Beverage, "Some notes on ultra high frequency propagation," *RCA Review*, vol. 1, pp. 76–87, January 1937.

[66] K. Bullington, "Radio propagation at frequencies above 30 megacycles," *Proceedings of the IRE*, vol. 35, pp. 1122 – 1136, October 1947.

[67] J. Epstein and D. W. Peterson, "An experimental study of wave propagation at 850 mc," *Proceedings of the IRE*, vol. 41, no. 5, pp. 595–611, 1953.

[68] J. J. Egli, "Radio propagation above 40 mc over irregular terrain," *Proceedings of the IRE*, vol. 45, no. 10, pp. 1383–1391, 1957.

[69] A. G. Longley and P. L. Rice, "Prediction of tropospheric radio transmission loss over irregular terrain. a computer method," tech. rep., Institute for Telecommunication Sciences, Boulder, CO, 1968.

[70] NTIA, "Irregular terrain model (Longley-Rice)." Web Page, 2010.

[71] M. Hata, "Empirical formula for propagation loss in land mobile radio services," *IEEE Transactions on Vehicular Technology*, vol. 29, no. 3, pp. 317–325, 1980.

[72] Sommerfeld, "Über die Ausbreitung der Wellen in der drahtlosen Telegraphie," *Annalen der Physik*, vol. 333, no. 4, p. 665736, 1909.

[73] G. Watson, "The diffraction of electric waves by the earth," *Proceedings of the Royal Society of London A*, vol. 95, pp. 83–99, 1918.

[74] J. Schelleng, C. Burrows, and E. Ferrell, "Ultra-short-wave propagation," *Proceedings of the Institute of Radio Engineers*, vol. 21, pp. 427 – 463, March 1933.

[75] C. Burrows, "Radio propagation over spherical earth," *Proceedings of the Institute of Radio Engineers*, vol. 23, pp. 470 – 480, May 1935.

[76] K. Norton, "The propagation of radio waves over the surface of the earth and in the upper atmosphere," *Proceedings of the Institute of Radio Engineers*, vol. 24, pp. 1367 – 1387, October 1936.

[77] K. Norton, "The physical reality of space and surface waves in the radiation field of radio antennas," *Proceedings of the Institute of Radio Engineers*, vol. 25, pp. 1192 – 1202, September 1937.

[78] K. Norton, "The calculation of ground-wave field intensity over a finitely conducting spherical earth," *Proceedings of the IRE*, vol. 29, pp. 623 – 639, December 1941.

[79] C. Burrows and M. Gray, "The effect of the earth's curvature on ground-wave propagation," *Proceedings of the IRE*, vol. 29, pp. 16 – 24, January 1941.

[80] S. O. Rice, "Mathematical analysis of random noise," *Bell System Technical Journal*, vol. 23 & 24, pp. 282–332, and 46–156, July 1944, 1945.

[81] S. O. Rice, "Statistical properties of a sine wave plus random noise," *Bell System Technical Journal*, vol. 27, pp. 109–157, January 1948.

[82] H. Friis, "A note on a simple transmission formula," *Proceedings of the IRE*, vol. 34, pp. 254–256, May 1946.

[83] K. Norton, "Transmission loss in radio propagation," *Proceedings of the IRE*, vol. 41, pp. 146 –152, January 1953.

[84] G. Hufford, "An integral equation approach to the problem of wave propagation over an irregular surface," *Quarterly of Applied Mathematics*, vol. 9, pp. 391–404, January 1952.

[85] R. H. Clarke, "A statistical theory of mobile-radio reception," *Bell System Technical Journal*, vol. 47, pp. 957–1000, July 1968.

[86] R. H. Ott and L. A. Berry, "An alternative integral equation for propagation over irregular terrain," *Radio Science*, vol. 5, pp. 767–771, May 1970.

[87] R. H. Ott, "An alternative integral equation for propagation over irregular terrain, 2," *Radio Science*, vol. 6, pp. 429–435, April 1971.

[88] R. Ott, L. Vogler, and G. Hufford, "Ground-wave propagation over irregular inhomogeneous terrain: Comparisons of calculations and measurements," *IEEE Transactions on Antennas and Propagation*, vol. 27, no. 2, pp. 284–286, 1979.

[89] L. E. Vogler, "An attenuation function for multiple knife-edge diffraction," *Radio Science*, vol. 17, pp. 1541–1546, November 1982.

[90] M. Meeks, "Vhf propagation over hilly, forested terrain," *IEEE Transactions on Antennas and Propagation*, vol. 31, no. 3, pp. 483–489, 1983.

[91] K. Chamberlin and R. Luebbers, "An evaluation of Longley-Rice and GTD propagation models," *Antennas and Propagation, IEEE Transactions on*, vol. 30, no. 6, pp. 1093–1098, 1982.

[92] R. Luebbers, "Propagation prediction for hilly terrain using GTD wedge diffraction," *IEEE Transactions on Antennas and Propagation*, vol. 32, no. 9, pp. 951–955, 1984.

[93] G. A. Deschamps, "Ray techniques in electromagnetics," *Proceedings of the IEEE*, vol. 60, no. 9, pp. 1022–1035, 1972.

[94] R. Kouyoumjian and P. Pathak, "A uniform geometrical theory of diffraction for an edge in a perfectly conducting surface," *Proceedings of the IEEE*, vol. 62, pp. 1448–1461, November 1974.

[95] R. H. Ott, "RING: An integral equation algorithm for hf-vhf radio wave propagation over irregular, inhomogeneous terrain," *Radio Science*, vol. 27, pp. 867–882, November 1992.

[96] R. Janaswamy, "A Fredholm integral equation method for propagation predictions over small terrain irregularities," *IEEE Transactions on Antennas and Propagation*, vol. 40, no. 11, pp. 1416–1422, 1992.

[97] D. Eppink and W. Kuebler, "TIREM/SEM handbook," tech. rep., Electromagnetic Compatibility Analysis Center Anapolis MD, Anapolis, 1994.

[98] J. T. Hviid, J. B. Andersen, J. Toftgard, and J. Bojer, "Terrain-based propagation model for rural area-an integral equation approach," *IEEE Transactions on Antennas and Propagation*, vol. 43, no. 1, pp. 41–46, 1995.

[99] J. Fernandez, M. Pino, F. Obelleiro, and J. Rodriguez, "Coverage analysis over terrain profiles using an adaptation of the spectral accelerated forward-backward method," in *Antennas and Propagation Society International Symposium, 2001. IEEE*, vol. 3, pp. 32–35, July 2001.

[100] C. Tunc, A. Altintas, and V. Erturk, "Examination of existent propagation models over large inhomogeneous terrain profiles using fast integral equation solution," *Antennas and Propagation, IEEE Transactions on*, vol. 53, pp. 3080–3083, September 2005.

[101] A. E. H. Love, "The integration of the equations of propagation of electric waves," *Philosophical Transactions of the Royal Society of London A*, vol. 197, pp. 1–45, 1901.

[102] S. Schelkunoff, "Some equivalence theorems of electromagnetics and their application to radiation problems," *Bell System Technical Journal*, vol. 15, pp. 92–112, 1936.

[103] V. H. Rumsey, "Reaction concept in electromagnetic theory," *Phys. Rev.*, vol. 94, pp. 1483–1491, June 1954.

[104] R. F. Harrington, L. F. Chang, A. T. Adams, R. Wallenberg, and T. Bristol, "Matrix methods for solving field problems. volume i. matrix techniques and applications.," tech. rep., Syracuse Univ NY Dept of Electrical Engineering, United States, 1966.

[105] N. Morita, N. Kumagai, and J. Mautz, *Integral Equation Methods for Electromagnetics.* Boston: Artech House, 1990.

[106] D. A. Kapp, *A New Method to Calculate Wave Scattering from Rough Surfaces at Low Grazing Angles.* PhD thesis, Virginia Polytechnic Institute and State University, Blacksburg, VA, 1995.

[107] D. Holliday, L. L. DeRaad, and G. J. St-Cyr, "Forward-backward: a new method for computing low-grazing angle scattering," *Antennas and Propagation, IEEE Transactions on*, vol. 44, p. 722, May 1996.

[108] D. Holliday, L. DeRaad, and G. St-Cyr, "Forward-backward method for scattering from imperfect conductors," *Antennas and Propagation, IEEE Transactions on*, vol. 46, pp. 101–107, January 1998.

[109] R. J. Adams and G. S. Brown, "Use of fast multipole method with method of ordered multiple interactions," *Electronics Letters*, vol. 34, no. 23, pp. 2219–2220, 1998.

[110] H. Chou and J. Johnson, "A novel acceleration algorithm for the computation of scattering from rough surfaces with the forward-backward method," *Radio Science*, vol. 33, pp. 1277–1287, September 1998.

[111] J. Toporkov, R. Marchand, and G. Brown, "On the discretization of the integral equation describing scattering by rough conducting surfaces," *Antennas and Propagation, IEEE Transactions on*, vol. 46, pp. 150–161, January 1998.

[112] A. Iodice, "Forward-backward method for scattering from dielectric rough surfaces," *Antennas and Propagation, IEEE Transactions on*, vol. 50, pp. 901–911, July 2002.

[113] B. A. Westin, *Applications in Remote Sensing Using the Method of Ordered Multiple Interactions*. PhD thesis, Virginia Polytechnic Institute and State University, Blacksburg, VA, 2013.

[114] C. A. Balanis, *Advanced Engineering Electromagnetics.* John Wiley & Sons, 1989.

[115] L. B. Felson and N. Marcuvitz, *Radiation and Scattering of Waves.* New York: IEEE Press, 1994.

[116] A. Ishimaru, *Electromagnetic Wave Propagation, Radiation, and Scattering.* New Jersey: Prentice Hall, 1991.

[117] D. S. Jones, *Methods in Electromagnetic Wave Propagation.* New York: IEEE Press, second edition ed., 1994.

[118] D. W. Trim, *Applied Partial Differential Equations.* Boston: PWS Publishing Co, 1990.

[119] D. A. de Wolf, *Essentials of Electromagnetics for Engineering.* Cambridge University Press, 2001.

[120] J. Van Bladel, *Singular Electromagnetic Fields and Sources.* Oxford: Clarendon Press, 1991.

[121] C. Tai, *Dyadic Green Functions in Electromagnetic Theory.* New York: IEEE Press, second ed., 1994.

[122] T. H. Black, "Radiation of a 2-d current sheet." Private Communication, 2007.

[123] R. F. Harrington, *Field Computation by Moment Methods.* New York: IEEE Press, 1993.

[124] E. Anderson, Z. Bai, C. Bischof, S. Blackford, J. Demmel, J. Dongarra, J. Du Croz, A. Greenbaum, S. Hammarling, A. McKenney, and D. Sorensen, *LAPACK Users' Guide*. Philadelphia, PA: Society for Industrial and Applied Mathematics, third ed., 1999.

[125] R. Harrington, "Matrix methods for field problems," *Proceedings of the IEEE*, vol. 55, no. 2, pp. 136 – 149, 1967.

[126] C. de Boor, *A Practical Guide to Splines*, vol. 27 of *Applied Mathematical Sciences*. New York: Springer-Verlag, 1978.

[127] W. L. Stutzman and G. A. Thiele, *Antenna Theory and Design*. New Jersey: John Wiley & Sons, 2nd ed., 1998.

[128] "The national map." http://www.nationalmap.gov, August 2012. Map services and data available from U.S. Geological Survey, National Geospatial Program.

[129] P. Bernardi, R. Cicchetti, and O. Testa, "A three-dimensional UTD heuristic diffraction coefficient for complex penetrable wedges," *IEEE Transactions on Antennas and Propagation*, vol. 50, no. 2, pp. 217–224, 2002.

[130] A. Iodice, "Computation of scattering from dielectric rough surfaces via the forward-backward method," in *Geoscience and Remote Sensing Symposium, 2001. IGARSS '01. IEEE 2001 International*, vol. 3, pp. 1381–1383vol.3, July 2001.

Appendix A

Derivatives of the Green's Function

The derivatives of the green's function are important for the computation of the scattered fields. The Green's function is

$$G(\mathbf{r} - \mathbf{r}_0) = \frac{1}{4j} H_0^{(2)} \left(k_0 \left| \mathbf{r} - \mathbf{r}_0 \right| \right)$$

$$G(\vec{\alpha}) = \frac{1}{4j} H_0^{(2)} \left(k_0 \alpha \right) \tag{A.1}$$

Here, $\vec{\alpha} = \mathbf{r} - \mathbf{r}_0$, is the vector from a source point to an observation point. The gradient of α is $\hat{\alpha}$, which is the unit vector in the direction of $\vec{\alpha}$. The vector $\hat{\beta} = \hat{\mathbf{y}} \times \hat{\alpha}$ will also be used. Together, $(\hat{\alpha}, \hat{\beta}, \hat{\mathbf{y}})$ form a set of cylindrical coordinates around the source point.

By applying the chain rule, the gradient of the Green's function is

$$\nabla G(\vec{\alpha}) = \frac{1}{4j} H_0^{(2)\prime} \left(k_0 \alpha \right) \nabla \left(k_0 \alpha \right) \tag{A.2}$$

$$\nabla G(\vec{\alpha}) = -\frac{k_0}{4j} H_1^{(2)} \left(k_0 \alpha \right) \hat{\alpha} \tag{A.3}$$

Note that $H_0^{(2)''}(z) = -H_1^{(2)}(z)$ [6].

Another important frame of referrence is that related to the surface. The surface normal is defined as $\hat{\mathbf{n}}$. Currents flow tangentially along the surface, either in the $\hat{\mathbf{y}}$ direction, or in the $\hat{\mathbf{s}} = \hat{\mathbf{y}} \times \hat{\mathbf{n}}$ direction. Because of this, the directional derivatives of the Green's function gradient is required for each of those current directions.

Since there is no y variation in the system,

$$(\hat{\mathbf{y}} \cdot \nabla)\nabla G(\vec{\boldsymbol{\alpha}}) = 0 \tag{A.4}$$

To take the $\hat{\mathbf{s}}$ derivative, one solution is to break the derivative down in to $\hat{\boldsymbol{\alpha}}$ and $\hat{\boldsymbol{\beta}}$ directions.

$$(\hat{\mathbf{s}} \cdot \nabla) = \hat{\mathbf{s}} \cdot \hat{\boldsymbol{\alpha}} \left(\hat{\boldsymbol{\alpha}} \cdot \nabla \right) + \hat{\mathbf{s}} \cdot \hat{\boldsymbol{\beta}} \left(\hat{\boldsymbol{\beta}} \cdot \nabla \right) \tag{A.5}$$

This requires the computation of the two cylindrical derivates $\frac{\partial}{\partial \alpha}\nabla G$ and $\frac{1}{\alpha}\frac{\partial}{\partial \beta}\nabla G$. Note that $H_1^{(2)'}(z) = H_0^{(2)}(z) - \frac{1}{z}H_1^{(2)}(z)$ [6].

The first of these derivatives is simple, as it is the derivative in the primary direction of change in the Green's function.

$$\frac{\partial}{\partial \alpha}\nabla G(\vec{\boldsymbol{\alpha}}) = -\frac{k_0^2}{4j}H_1^{(2)'}(k_0\alpha)\,\hat{\boldsymbol{\alpha}} \tag{A.6}$$

$$\frac{\partial}{\partial \alpha}\nabla G(\vec{\boldsymbol{\alpha}}) = -\hat{\boldsymbol{\alpha}}\frac{k_0^2}{4j}\left[H_0^{(2)}(k_0\alpha) \right.$$
$$\left. -\frac{1}{k_0\alpha}H_1^{(2)}(k_0\alpha) \right] \tag{A.7}$$

The second is more complicated. This derivative requires applying the product rule and taking the derivatives of $\frac{\partial \hat{\alpha}}{\partial \beta} = \hat{\boldsymbol{\beta}}$ and $\frac{\partial \alpha}{\partial \beta} = \hat{\boldsymbol{\beta}} \cdot \nabla \alpha = \hat{\boldsymbol{\beta}} \cdot \hat{\boldsymbol{\alpha}} = 0$.

$$\frac{1}{\alpha} \frac{\partial}{\partial \beta} \nabla G(\vec{\boldsymbol{\alpha}}) = -\frac{k_0}{4j\alpha} H_1^{(2)}(k_0\alpha) \hat{\boldsymbol{\beta}} \tag{A.8}$$

By combining (A.5), (A.7), and (A.8), it is possible to attain the final derivative that is sought,

$$
\begin{aligned}
(\hat{\mathbf{s}} \cdot \nabla) \nabla G(\vec{\boldsymbol{\alpha}}) &= \frac{k_0^2}{4j} (\hat{\mathbf{s}} \cdot \hat{\boldsymbol{\alpha}}) \left(\hat{\boldsymbol{\alpha}} \left[H_0^{(2)}(k_0\alpha) - \frac{1}{k_0\alpha} H_1^{(2)}(k_0\alpha) \right] \right) \\
&\quad + \left(\hat{\mathbf{s}} \cdot \hat{\boldsymbol{\beta}} \right) \hat{\boldsymbol{\beta}} \frac{1}{k_0\alpha} H_1^{(2)}(k_0\alpha)
\end{aligned}
\tag{A.9}
$$

Also important is the Laplacian of the Green's functions, which is easily determined from the defining equation of the Green's function, (3.16).

$$\nabla^2 G(\vec{\boldsymbol{\alpha}}) = -\delta(\alpha) - \frac{k_0^2}{4j} H_0^{(2)}(k_0\alpha) \tag{A.10}$$

These are the derivatives which are necessary for evaluating the fields scattered by two-dimensional sheet currents as seen in chapter 3.

Appendix B

Electric and Magnetic Sources in the

$\hat{\mathbf{y}}$ Direction

The fields of (3.28a) and (3.28b) are easy to generalize to any direction, by generalizing $\hat{\mathbf{z}}$ to $\hat{\boldsymbol{l}}$. First note that the electric field is in the direction of the current, and that ρ is the distance of the point of observation from the line source. Then for a point $\mathbf{r}$ in space, and a point $\mathbf{r}_0$ on the line source, $\boldsymbol{\rho}_l$ is given by:

$$\boldsymbol{\rho}_l = (\mathbf{r} - \mathbf{r}_0) - \hat{\boldsymbol{l}} \left[(\mathbf{r} - \mathbf{r}_0) \cdot \hat{\boldsymbol{l}} \right].$$

Note that $\boldsymbol{\rho}_l \cdot \hat{\boldsymbol{l}} = 0$, indicating that $\boldsymbol{\rho}_l$ is perpendicular to $\hat{\boldsymbol{l}}$. The vector $\hat{\boldsymbol{\phi}}$ in the magnetic field in (3.28a) is given as $\hat{\mathbf{z}} \times \hat{\boldsymbol{\rho}}$. That vector can then be generalized to:

$$\hat{\boldsymbol{\phi}}_l = \hat{\boldsymbol{l}} \times \hat{\boldsymbol{\rho}}_l.$$

Since future work will take place in a 2-dimensional, x-z space, with source currents

extending in the y direction, the vectors of interest are defined as the $\{\boldsymbol{\rho_y}, \hat{\boldsymbol{\phi}}_y, \hat{\mathbf{y}}\}$ triplet.

$$\boldsymbol{\rho_y} = x\hat{\mathbf{x}} + z\hat{\mathbf{z}} \tag{B.1a}$$

$$\hat{\boldsymbol{\phi}}_y = \hat{\mathbf{y}} \times \boldsymbol{\hat{\rho}_y} \tag{B.1b}$$

$$\phi_y = arctan(-z/x) \tag{B.1c}$$

Using these vectors, it is simple to express the electric and magnetic fields for the y-oriented electric line source.

$$\mathbf{H} = \hat{\boldsymbol{\phi}}_y \frac{I_e k_0}{4j} H_1^{(2)}(k_0 \rho_y) \tag{B.2a}$$

$$\mathbf{E} = -\hat{\mathbf{y}} \frac{I_e \omega \mu}{4} H_0^{(2)}(k_0 \rho_y) \tag{B.2b}$$

When a magnetic line source, $I_m \hat{\mathbf{y}}$, is considered, the solution is the dual of the above equations.

$$\mathbf{E} = -\hat{\boldsymbol{\phi}}_y \frac{I_m k_0}{4j} H_1^{(2)}(k_0 \rho_y) \tag{B.3a}$$

$$\mathbf{H} = -\hat{\mathbf{y}} \frac{I_m \omega \epsilon}{4} H_0^{(2)}(k_0 \rho_y) \tag{B.3b}$$

Appendix C

Experimental Measurements

Chapter 7 gave the procedure for a set of propagation measurements made in the vicinity of Green Bank, West Virginia, and summarized the results. This appendix provides the actual data measurements and the calibration values used. Tables are provided for each path on which testing occurred. Columns provided vary by the receiver location and test date, but are amongst the following: "Run #" is a unique identifier for each setup and measurement, postscripted with letters to indicate multiple measurements taken at the intermediate points for a given transmitter setup; "Date" and "Time" are the date and time of the measurements; "Freq. (MHz)" is the frequency of the measurment in megahertz; "Pol." lists either H for horizontal polarization or V for vertical polarization; "Tx. Height (ft.)" is the transmitting antenna height above ground, in feet; "EIRP (dBm)" is the callibrated measured value for the equivalent isotropically radiated power from the transmitter, in decibels relative to one milliwatt; "Cable" lists a unique identifier for the cable used for the measurement on the

receiver; "Test Setup" lists any other unique information relavent to the test setup, such as inclusion of an amplifier at the receiver; "Meas. Type" is either the one minute maximum (MAX), minimum (MIN), or median (MED) that is recorded, all Jack Ball and Horse Ridge measurements were one minute maxima; "Rx. Height (ft.)" is the height of the receiving antenna above the ground (or lab roof for Jansky Lab) in feet; "Rx. Power (dBm)" is the power recorded at the receiver, in decibels relative to one milliwatt; "Antenna Gain (dBi)" is the gain of the receiving antenna, in decibels relative to an isotropic antenna; "Cable Loss (dB)" is the calibrated loss of the cabling and connectors from the antenna to the receiver in decibels; "LNA Gain (dB)" is the gain of the low noise amplifier inserted into the receiver path; "Path Loss (dB)" is the computed value of the path loss in decibels, accounting for all known gains and losses.

Table C.1: Measurements between Jack Ball and Jansky Lab

			Transmit Site					Jansky Lab Receive Site				
Run #	Date	Time	Freq. (MHz)	Pol.	Tx. Height (ft.)	EIRP (dBm)	Cable	Rx. Height (ft.)	Rx. Power (dBm)	Antenna Gain (dBi)	Cable Loss (dB)	Path Loss (dB)
1	08/03/09	16:43	904.15	V	30	74.4	50	17	-24.07	16.67	-2.29	-112.85
2	08/03/09	16:52	926.15	V	30	74.47	50	17	-22.5	17.37	-2.4	-111.94
3	08/03/09	17:04	2303.15	H	30	67.8	75	19	-47.03	14	-8.08	-120.75
4	08/03/09	17:10	2303.15	H	30	66.8	75	19	-47.27	14	-8.08	-119.99
5	08/04/09	09:30	904.15	V	30	74.4	50	17	-24.63	16.67	-2.29	-113.41
6	08/04/09	09:35	926.15	V	30	74.8	50	17	-23.4	17.37	-2.4	-113.17
7	08/04/09	09:47	2303.15	H	30	67.4	75	19	-47.97	14	-8.08	-121.29
8	08/04/09	09:54	2303.15	H	20	67.4	75	19	-53.93	14	-8.08	-127.25
9	08/04/09	10:08	904.15	V	20	74.4	50	17	-25.3	16.67	-2.29	-114.08
10	08/04/09	10:11	926.15	V	20	74.7	50	17	-24.63	17.37	-2.4	-114.3
11	08/04/09	10:47	926.15	H	20	74.7	50	17	-25.83	17.37	-2.4	-115.5
12	08/04/09	10:49	904.15	H	20	74.4	50	17	-24.23	16.67	-2.29	-113.01
13	08/04/09	10:55	904.15	H	30	74.4	50	17	-22.98	16.67	-2.29	-111.76
14	08/04/09	10:57	926.15	H	30	74.6	50	17	-22.5	17.37	-2.4	-112.07
15	08/04/09	11:10	2303.15	V	30	67.4	75	19	-48.13	14	-8.08	-121.45
16	08/04/09	11:17	2303.15	V	20	67.4	75	19	-53.6	14	-8.08	-126.92
17	08/04/09	12:43	1296.91	V	20	77.5	75	19	-30.73	16.13	-5.99	-118.37
18	08/04/09	13:00	1296.91	V	30	77.5	75	19	-28.07	16.13	-5.99	-115.71
19	08/04/09	13:07	904.15	H	30	74.1	50	17	-25.27	16.67	-2.29	-113.75
20	08/04/09	13:10	926.15	H	30	74.3	50	17	-23.53	17.37	-2.4	-112.8
21	08/04/09	13:46	1296.91	H	20	76.8	75	19	-32.47	16.13	-5.99	-119.41
22	08/04/09	13:53	1296.91	H	30	76.8	75	19	-28.4	16.13	-5.99	-115.34
23	08/04/09	15:44	1296.91	H	30	76.3	75	19	-29.67	16.13	-5.99	-116.11
24	08/04/09	15:45	1296.91	H	30	76.3	75	19	-29.37	16.13	-5.99	-115.81
25	08/04/09	15:55	904.15	V	30	74.1	50	17	-24.7	16.67	-2.29	-113.18
26	08/04/09	16:00	926.15	V	30	74.2	50	17	-23.53	17.37	-2.4	-112.7
51	08/06/09	12:44	904.15	V	30	74.4	50	17	-22.47	16.67	-2.29	-111.25
52	08/06/09	12:48	926.15	V	30	74.5	50	17	-22.87	17.37	-2.4	-112.34
53	08/06/09	12:52	926.15	V	20	74.5	50	17	-28.3	17.37	-2.4	-117.77
54	08/06/09	12:55	904.15	V	20	74.4	50	17	-27.87	16.67	-2.29	-116.65
55	08/06/09	13:00	904.15	V	10	74.4	50	17	-30.73	16.67	-2.29	-119.51

Table C.1: Measurements between Jack Ball and Jansky Lab (cont.)

Run #	Date	Time	Freq. (MHz)	Pol.	Tx. Height (ft.)	EIRP (dBm)	Cable	Rx. Height (ft.)	Rx. Power (dBm)	Antenna Gain (dBi)	Cable Loss (dB)	Path Loss (dB)
56	08/06/09	13:02	926.15	V	10	74.7	50	17	-29.87	17.37	-2.4	-119.54
57	08/06/09	13:21	926.15	H	30	74.5	50	17	-23.73	17.37	-2.4	-113.2
58	08/06/09	13:26	904.15	H	30	74.7	50	17	-23.19	16.67	-2.29	-112.27
59	08/06/09	13:32	1296.91	V	30	77.5	75	19	-40.3	16.13	-19.03	-114.9
60	08/06/09	13:36	1296.91	V	20	77.5	75	19	-44.1	16.13	-19.03	-118.7
61	08/06/09	13:40	904.15	H	20	74.7	50	17	-26.57	16.67	-2.29	-115.65
62	08/06/09	13:43	926.15	H	20	74	50	17	-28.03	17.37	-2.4	-117
63	08/06/09	13:48	926.15	H	10	74	50	17	-27.47	17.37	-2.4	-116.44
64	08/06/09	13:53	904.15	H	10	74.4	50	17	-27.33	16.67	-2.29	-116.11
65	08/06/09	13:57	1296.91	V	10	77.3	75	19	-43.87	16.13	-19.03	-118.27
66	08/06/09	14:23	1296.91	H	10	76.8	75	19	-41.23	16.13	-19.03	-115.13
67	08/06/09	14:28	1296.91	H	20	76.8	75	19	-41.73	16.13	-19.03	-115.63
68	08/06/09	14:32	1296.91	H	30	76.8	75	19	-37.53	16.13	-19.03	-111.43
69	08/06/09	14:50	2303.15	V	30	67.1	50	17	-45.3	14	-4.11	-122.29
70	08/06/09	14:55	2303.15	V	20	66.3	50	17	-51	14	-4.11	-127.19
71	08/06/09	15:01	2303.15	V	10	66.3	50	17	-54.75	14	-4.11	-130.94
72	08/06/09	15:23	2303.15	H	10	66.1	50	17	-56.73	14	-4.11	-132.72
73	08/06/09	15:27	2303.15	H	20	66.3	50	17	-49.5	14	-4.11	-125.69
74	08/06/09	15:33	2303.15	H	30	66.1	50	17	-47.43	14	-4.11	-123.42

Table C.2: Measurements between Jack Ball and Intermediate Points

			Transmit Site					Intermediate Point Receive Sites					
Run #	Date	Time	Freq. (MHz)	Pol.	Tx. Height (ft.)	EIRP (dBm)	Site #	Rx. Height (ft.)	Test Setup	Rx. Power (dBm)	Antenna Gain (dBi)	Cable Loss (dB)	Path Loss (dB)
1	08/03/09	16:43	904.15	V	30	74.4	IP1	5	No Amp	-42	4.67	-0.8	-120.27
2	08/03/09	16:52	926.15	V	30	74.47	IP1	5	No Amp	-40.6	5.03	-0.8	-119.3
3	08/03/09	17:04	2303.15	H	30	67.8	IP1	5	No Amp	-64.5	2.83	-1.9	-133.23
3a	08/03/09	17:05	2303.15	H	30	67.8	IP1	5	Amp	-57	12.33	-1.9	-135.23
4	08/03/09	17:10	2303.15	H	30	66.8	IP1	5	No Amp	-63.2	2.83	-1.9	-130.93
4a	08/03/09	17:11	2303.15	H	30	66.8	IP1	5	Amp	-57.08	12.33	-1.9	-134.31
5	08/04/09	09:30	904.15	V	30	74.4	IP1	5	No Amp	-41.92	4.67	-0.8	-120.19
6	08/04/09	09:35	926.15	V	30	74.8	IP1	5	No Amp	-42.58	5.03	-0.8	-121.61
7	08/04/09	09:47	2303.15	H	30	67.4	IP1	5	No Amp	-62.34	2.83	-1.9	-130.67
7a	08/04/09	09:45	2303.15	H	30	67.4	IP1	5	Amp	-63.14	12.33	-1.9	-140.97
8	08/04/09	09:54	2303.15	H	20	67.4	IP1	5	No Amp	-64.6	2.83	-1.9	-132.93
8a	08/04/09	09:53	2303.15	H	20	67.4	IP1	5	Amp	-65.86	12.33	-1.9	-143.69
9	08/04/09	10:08	904.15	V	20	74.4	IP1	5	No Amp	-43.29	4.67	-0.8	-121.56
10	08/04/09	10:11	926.15	V	20	74.7	IP1	5	No Amp	-45.45	5.03	-0.8	-124.38
11	08/04/09	10:47	926.15	H	20	74.7	IP1	5	No Amp	-43.16	5.03	-0.8	-122.09
12	08/04/09	10:49	904.15	H	20	74.4	IP1	5	No Amp	-42.89	4.67	-0.8	-121.16
13	08/04/09	10:55	904.15	H	30	74.4	IP1	5	No Amp	-41.74	4.67	-0.8	-120.01
14	08/04/09	10:57	926.15	H	30	74.6	IP1	5	No Amp	-41.95	5.03	-0.8	-120.78
15	08/04/09	11:10	2303.15	V	30	67.4	IP1	5	No Amp	-61.22	2.83	-1.9	-129.55
16	08/04/09	11:17	2303.15	V	20	67.4	IP1	5	No Amp	-64.9	2.83	-1.9	-133.23
17	08/04/09	12:43	1296.91	V	20	77.5	IP1	5	No Amp	-51	4.13	-1.5	-131.13
18	08/04/09	13:00	1296.91	V	30	77.5	IP1	5	No Amp	-49	4.13	-1.5	-129.13
19	08/04/09	13:07	904.15	H	30	74.1	IP1	5	No Amp	-42.9	4.67	-0.8	-120.87
20	08/04/09	13:10	926.15	H	30	74.3	IP1	5	No Amp	-41.5	5.03	-0.8	-120.03
21	08/04/09	13:46	1296.91	H	20	76.8	IP1	5	No Amp	-51.04	4.13	-1.5	-130.47
22	08/04/09	13:53	1296.91	H	30	76.8	IP1	5	No Amp	-48	4.13	-1.5	-127.43
24	08/04/09	15:45	1296.91	H	30	76.3	WT	113	No Amp	-26	4.13	-1.5	-104.93
25	08/04/09	15:55	904.15	V	30	74.1	WT	113	No Amp	-24	4.67	-0.8	-101.97
26	08/04/09	16:00	926.15	V	30	74.2	WT	113	No Amp	-22	5.03	-0.8	-100.43
51	08/06/09	12:44	904.15	V	30	74.4	WT	113	No Amp	-22.3	4.67	-0.8	-100.57
52	08/06/09	12:48	926.15	V	30	74.5	WT	113	No Amp	-24.2	5.03	-0.8	-102.93

Table C.2: Measurements between Jack Ball and Intermediate Points (cont.)

Run #	Date	Time	Freq. (MHz)	Pol.	Tx. Height (ft.)	EIRP (dBm)	Site #	Rx. Height (ft.)	Test Setup	Rx. Power (dBm)	Antenna Gain (dBi)	Cable Loss (dB)	Path Loss (dB)
53	08/06/09	12:52	926.15	V	20	74.5	WT	113	No Amp	-24.35	5.03	-0.8	-103.08
54	08/06/09	12:55	904.15	V	20	74.4	WT	113	No Amp	-23	4.67	-0.8	-101.27
55	08/06/09	13:00	904.15	V	10	74.4	WT	113	No Amp	-22.66	4.67	-0.8	-100.93
56	08/06/09	13:02	926.15	V	10	74.7	WT	113	No Amp	-21.42	5.03	-0.8	-100.35
57	08/06/09	13:21	926.15	H	30	74.5	WT	113	No Amp	-24	5.03	-0.8	-102.73
58	08/06/09	13:26	904.15	H	30	74.7	WT	113	No Amp	-22.84	4.67	-0.8	-101.41
59	08/06/09	13:32	1296.91	V	30	77.5	WT	113	No Amp	-25.44	4.13	-1.5	-105.57
60	08/06/09	13:36	1296.91	V	20	77.5	WT	113	No Amp	-24.37	4.13	-1.5	-104.5
61	08/06/09	13:40	904.15	H	20	74.7	WT	113	No Amp	-23.73	4.67	-0.8	-102.3
62	08/06/09	13:43	926.15	H	20	74	WT	113	No Amp	-24.07	5.03	-0.8	-102.3
63	08/06/09	13:48	926.15	H	10	74	WT	113	No Amp	-20.58	5.03	-0.8	-98.81
64	08/06/09	13:53	904.15	H	10	74.4	WT	113	No Amp	-20.14	4.67	-0.8	-98.41
65	08/06/09	13:57	1296.91	V	10	77.3	WT	113	No Amp	-27.1	4.13	-1.5	-107.03
66	08/06/09	14:23	1296.91	H	10	76.8	WT	113	No Amp	-28.2	4.13	-1.5	-107.63
67	08/06/09	14:28	1296.91	H	20	76.8	WT	113	No Amp	-24.54	4.13	-1.5	-103.97
68	08/06/09	14:32	1296.91	H	30	76.8	WT	113	No Amp	-25.74	4.13	-1.5	-105.17
69	08/06/09	14:50	2303.15	V	30	67.1	WT	113	No Amp	-41.7	2.83	-1.9	-109.73
70	08/06/09	14:55	2303.15	V	20	66.3	WT	113	No Amp	-42.15	2.83	-1.9	-109.38
71	08/06/09	15:01	2303.15	V	10	66.3	WT	113	No Amp	-38.18	2.83	-1.9	-105.41
72	08/06/09	15:23	2303.15	H	10	66.1	WT	113	No Amp	-39.58	2.83	-1.9	-106.61
73	08/06/09	15:27	2303.15	H	20	66.3	WT	113	No Amp	-43	2.83	-1.9	-110.23
74	08/06/09	15:33	2303.15	H	30	66.1	WT	113	No Amp	-42.35	2.83	-1.9	-109.38

Table C.3: Measurements between Horse Ridge and Jansky Lab, Aug. 5 2009

		Transmit Site				Jansky Lab Receive Site					
Run #	Time	Freq. (MHz)	Pol.	Tx. Height (ft.)	EIRP (dBm)	Cable	Rx. Height (ft.)	Rx. Power (dBm)	Antenna Gain (dBi)	Cable Loss (dB)	Path Loss (dB)
27	09:29	904.15	V	30	74.1	50	17	-53.5	16.67	-2.29	-141.98
28	09:38	926.15	V	30	74.5	50	17	-52.33	17.37	-2.4	-141.8
29	09:46	1296.91	H	30	77.0	75	19	-68.5	16.13	-5.99	-155.64
30	09:52	1296.91	H	20	77.0	75	19	-67.58	16.13	-5.99	-154.72
30-2	10:06	1296.91	H	10	77.0	75	19	-73.17	16.13	-5.99	-160.31
31	10:28	1296.91	V	20	77.3	75	19	-68.7	16.13	-5.99	-156.14
32	10:35	1296.91	V	30	77.3	75	19	-69.13	16.13	-5.99	-156.57
33	10:41	904.15	H	30	74.1	50	17	-51.5	16.67	-2.29	-139.98
34	10:44	926.15	H	30	74.8	50	17	-51.58	17.37	-2.4	-141.35
35	10:48	926.15	H	20	74.8	50	17	-55.17	17.37	-2.4	-144.94
35-2	10:51	926.15	H	10	74.8	50	17	-55.5	17.37	-2.4	-145.27
36	11:52	2303.15	V	30	66.1	75	19	N/A	14	-8.08	N/A
37	12:28	904.15	H	30	74.1	50	17	-54.17	16.67	-2.29	-142.65
38	12:32	926.15	H	30	74.3	50	17	-54.42	17.37	-2.4	-143.69
39	13:04	904.15	V	30	74.2	50	17	-55.08	16.67	-2.29	-143.66
40	13:07	926.15	V	30	74.7	50	17	-53.77	17.37	-2.4	-143.44
41	13:17	2303.15	H	30	69.6	75	19	N/A	14	-8.08	N/A
42	13:55	1296.91	H	30	73.9	75	19	-69.5	16.13	-5.99	-153.54
43	14:24	1296.91	V	30	77.0	75	19	-69.2	16.13	-5.99	-156.34
44	15:06	1296.91	V	30	76.7	75	19	-70.53	16.13	-5.99	-157.37
45	15:45	1296.91	H	30	76.7	75	19	-69.93	16.13	-5.99	-156.77
46	15:55	904.15	V	30	75.0	50	17	-53.33	16.67	-2.29	-142.71
47	16:38	926.15	V	30	74.2	50	17	-52.25	17.37	-2.4	-141.42
48	16:50	926.15	H	30	74.2	50	17	-53.92	17.37	-2.4	-143.09
49	16:59	904.15	H	30	74.1	50	17	-54.83	16.67	-2.29	-143.31
50	16:59	904.15	H	30	74.1	50	17	-54.67	16.67	-2.29	-143.15

Table C.4: Measurements between Horse Ridge and Intermediate Points, Aug. 5, 2009

		Transmit Site					Intermediate Point Receive Sites					
Run #	Time	Freq. (MHz)	Pol.	Tx. Height (ft.)	EIRP (dBm)	Rx. Height (ft.)	Site #	Test Setup	Rx. Power (dBm)	Antenna Gain (dBi)	Cable Loss (dB)	Path Loss (dB)
27	09:29	904.15	V	30	74.1	5	IP3	No Amp	-59.3	4.67	-0.8	-137.27
28	09:38	926.15	V	30	74.5	5	IP3	No Amp	-63.8	5.03	-0.8	-142.53
29	09:46	1296.91	H	30	77.0	5	IP3	No Amp	-71.7	4.13	-1.5	-151.33
30	09:52	1296.91	H	20	77.0	5	IP3	No Amp	-70.1	4.13	-1.5	-149.73
31	10:28	1296.91	V	20	77.3	5	IP3	No Amp	-74	4.13	-1.5	-153.93
31a	10:28	1296.91	V	20	77.3	5	IP3	Amp	-64.44	15.97	-1.5	-156.21
32	10:35	1296.91	V	30	77.3	5	IP3	No Amp	-74.98	4.13	-1.5	-154.91
32a	10:35	1296.91	V	30	77.3	5	IP3	Amp	-65.69	15.97	-1.5	-157.46
33	10:41	904.15	H	30	74.1	5	IP3	No Amp	-62.21	4.67	-0.8	-140.18
34	10:44	926.15	H	30	74.8	5	IP3	No Amp	-58.4	5.03	-0.8	-137.43
35	10:48	926.15	H	20	74.8	5	IP3	No Amp	-61.94	5.03	-0.8	-140.97
35-2	10:51	926.15	H	10	74.8	5	IP3	No Amp	-62.4	5.03	-0.8	-141.43
36	11:52	2303.15	V	30	66.1	5	IP4	No Amp	-70.4	2.83	-1.9	-137.43
36a	11:52	2303.15	V	30	66.1	5	IP4	Amp	-63.6	12.33	-1.9	-140.13
36b	11:52	2303.15	V	30	66.1	5	IP4	No Amp	-68.5	2.83	-1.9	-135.53
36c	11:52	2303.15	V	30	66.1	5	IP4	Amp	-60	12.33	-1.9	-136.53
37	12:28	904.15	H	30	74.1	5	IP4	No Amp	-49.14	4.67	-0.8	-127.11
38	12:32	926.15	H	30	74.3	5	IP4	No Amp	-50.67	5.03	-0.8	-129.2
39	13:04	904.15	V	30	74.2	5	IP4	No Amp	-52.15	4.67	-0.8	-130.22
40	13:07	926.15	V	30	74.7	5	IP4	No Amp	-52.04	5.03	-0.8	-130.97
41	13:17	2303.15	H	30	69.6	5	IP4	No Amp	-70.9	2.83	-1.9	-141.43
41a	13:17	2303.15	H	30	69.6	5	IP4	Amp	-64.03	12.33	-1.9	-144.06
42	13:55	1296.91	H	30	73.9	5	IP4	No Amp	-55.9	4.13	-1.5	-132.43
43	14:24	1296.91	V	30	77.0	5	IP4	No Amp	-58.77	4.13	-1.5	-138.4
44	15:06	1296.91	V	30	76.7	5	IP5	No Amp	-73.2	4.13	-1.5	-152.53
44a	15:06	1296.91	V	30	76.7	5	IP5	Amp	-63.6	15.97	-1.5	-154.77
45	15:45	1296.91	H	30	76.7	5	IP5	No Amp	-72.5	4.13	-1.5	-151.83
46	15:55	904.15	V	30	75.0	5	IP5	No Amp	-69.36	4.67	-0.8	-148.23
47	16:38	926.15	V	30	74.2	5	IP5	No Amp	-70.5	5.03	-0.8	-148.93
47a	16:38	926.15	V	30	74.2	5	IP5	Amp	-60.3	17.53	-0.8	-151.23
48	16:50	926.15	H	30	74.2	5	IP5	No Amp	-70.3	5.03	-0.8	-148.73

Table C.4: Measurements between Horse Ridge and Intermediate Points, Aug. 5, 2009 (cont.)

Run #	Time	Freq. (MHz)	Pol.	Tx. Height (ft.)	EIRP (dBm)	Rx. Height (ft.)	Site #	Test Setup	Rx. Power (dBm)	Antenna Gain (dBi)	Cable Loss (dB)	Path Loss (dB)
48a	16:50	926.15	H	30	74.2	5	IP5	Amp	-59.5	17.53	-0.8	-150.43
49	16:59	904.15	H	30	74.1	5	IP5	Amp	-65.11	17	-0.8	-155.41
50	16:59	904.15	H	30	74.1	5	IP5	No Amp	-73.5	4.67	-0.8	-151.47
50a	16:59	904.15	H	30	74.1	5	IP5	Amp	-63.38	17	-0.8	-153.68

Table C.5: Measurements between Short North 2 and Jansky Lab, Aug. 2 and 3, 2010

		Transmit Site				Jansky Lab Receive Site						
Run #	Time	Freq. (MHz)	Pol.	Tx. Height (ft.)	EIRP (dBm)	Rx. Height (ft.)	Meas. Type	Rx. Power (dBm)	Antenna Gain (dBi)	Cable Loss (dB)	LNA Gain (dB)	Path Loss (dB)
1	1104	904.15	V	10	74.27	18.5	Max	-45.09	16.7	1.8	0.0	-134.26
2	1108	926.15	V	10	75.67	18.5	Max	-40.11	17.4	2.0	0.0	-131.18
3	1114	1296.91	H	10	75.70	20.75	Max	-32.88	15.8	2.5	0.0	-121.88
4	1120	1296.91	H	20	75.70	20.75	Max	-32.26	15.8	2.5	0.0	-121.26
5	1127	904.15	V	20	74.47	18.5	Max	-33.52	16.7	1.8	0.0	-122.89
5	1127	904.15	V	20	74.47	18.5	Min	-34.47	16.7	1.8	0.0	-123.84
6	1130	926.15	V	20	75.67	18.5	Max	-37.00	17.4	2.0	0.0	-128.07
6	1130	926.15	V	20	75.67	18.5	Med	-37.74	17.4	2.0	0.0	-128.81
6	1130	926.15	V	20	75.67	18.5	Min	-38.41	17.4	2.0	0.0	-129.48
7	1137	926.15	V	30	75.97	18.5	Max	-35.69	17.4	2.0	0.0	-127.06
7	1137	926.15	V	30	75.97	18.5	Med	-35.74	17.4	2.0	0.0	-127.11
7	1137	926.15	V	30	75.97	18.5	Min	-36.36	17.4	2.0	0.0	-127.73
8	1141	904.15	V	30	74.57	18.5	Max	-33.55	16.7	1.8	0.0	-123.02
8	1141	904.15	V	30	74.57	18.5	Med	-33.96	16.7	1.8	0.0	-123.43
8	1141	904.15	V	30	74.57	18.5	Min	-33.97	16.7	1.8	0.0	-123.44
9	1148	1296.91	H	30	75.80	20.75	Max	-31.93	15.8	2.5	0.0	-121.03
9	1148	1296.91	H	30	75.80	20.75	Med	-32.40	15.8	2.5	0.0	-121.50
9	1148	1296.91	H	30	75.80	20.75	Min	-32.60	15.8	2.5	0.0	-121.70
10	1229	1296.91	V	30	75.80	20.75	Max	-38.71	15.8	2.5	0.0	-127.81
10	1229	1296.91	V	30	75.80	20.75	Med	-39.74	15.8	2.5	0.0	-128.84
10	1229	1296.91	V	30	75.80	20.75	Min	-40.34	15.8	2.5	0.0	-129.44
11	1245	904.15	H	30	74.77	18.5	Max	-26.89	16.7	1.8	0.0	-116.56
11	1245	904.15	H	30	74.77	18.5	Med	-27.45	16.7	1.8	0.0	-117.12
11	1245	904.15	H	30	74.77	18.5	Min	-27.61	16.7	1.8	0.0	-117.28
12	1251	926.15	H	30	75.67	18.5	Max	-30.61	17.4	2.0	0.0	-121.68
12	1251	926.15	H	30	75.67	18.5	Med	-30.96	17.4	2.0	0.0	-122.03
12	1251	926.15	H	30	75.67	18.5	Min	-31.66	17.4	2.0	0.0	-122.73
13	1258	926.15	H	20	75.77	18.5	Max	-29.63	17.4	2.0	0.0	-120.80
13	1258	926.15	H	20	75.77	18.5	Med	-29.72	17.4	2.0	0.0	-120.89
13	1258	926.15	H	20	75.77	18.5	Min	-29.98	17.4	2.0	0.0	-121.15
14	1301	904.15	H	20	74.77	18.5	Max	-27.17	16.7	1.8	0.0	-116.84

Table C.5: Measurements between Short North 2 and Jansky Lab, Aug. 2 and 3, 2010 (cont.)

Run #	Time	Freq. (MHz)	Pol.	Tx. Height (ft.)	EIRP (dBm)	Rx. Height (ft.)	Meas. Type	Rx. Power (dBm)	Antenna Gain (dBi)	Cable Loss (dB)	LNA Gain (dB)	Path Loss (dB)
14	1301	904.15	H	20	74.77	18.5	Med	-27.31	16.7	1.8	0.0	-116.98
14	1301	904.15	H	20	74.77	18.5	Min	-27.94	16.7	1.8	0.0	-117.61
15	1315	1296.91	V	20	76.00	20.75	Max	-34.93	15.8	2.5	0.0	-124.23
15	1315	1296.91	V	20	76.00	20.75	Med	-36.36	15.8	2.5	0.0	-125.66
15	1315	1296.91	V	20	76.00	20.75	Min	-37.37	15.8	2.5	0.0	-126.67
16	1319	1296.91	V	10	76.00	20.75	Max	-34.52	15.8	2.5	0.0	-123.82
16	1319	1296.91	V	10	76.00	20.75	Med	-34.80	15.8	2.5	0.0	-124.10
16	1319	1296.91	V	10	76.00	20.75	Min	-35.60	15.8	2.5	0.0	-124.90
17	1323	904.15	H	10	74.77	18.5	Max	-31.63	16.7	1.8	0.0	-121.30
17	1323	904.15	H	10	74.77	18.5	Med	-32.20	16.7	1.8	0.0	-121.87
17	1323	904.15	H	10	74.77	18.5	Min	-32.50	16.7	1.8	0.0	-122.17
18	1326	926.15	H	10	75.77	18.5	Max	-32.64	17.4	2.0	0.0	-123.81
18	1326	926.15	H	10	75.77	18.5	Med	-33.83	17.4	2.0	0.0	-125.00
18	1326	926.15	H	10	75.77	18.5	Min	-33.91	17.4	2.0	0.0	-125.08
19	1406	2303.15	V	10	68.50	20.75	Max	-55.46	14.0	3.5	0.0	-134.46
19	1406	2303.15	V	10	68.50	20.75	Med	-58.13	14.0	3.5	0.0	-137.13
19	1406	2303.15	V	10	68.50	20.75	Min	-61.65	14.0	3.5	0.0	-140.65
20	1425	2303.15	V	20	68.40	20.75	Max	-56.96	14.0	3.5	0.0	-135.86
20	1425	2303.15	V	20	68.40	20.75	Med	-63.22	14.0	3.5	0.0	-142.12
20	1425	2303.15	V	20	68.40	20.75	Min	-65.35	14.0	3.5	0.0	-144.25
21	1636	1296.91	H	40	76.60	20.75	Max	-29.52	15.8	2.5	0.0	-119.42
21	1636	1296.91	H	40	76.60	20.75	Med	-31.10	15.8	2.5	0.0	-121.00
21	1636	1296.91	H	40	76.60	20.75	Min	-31.33	15.8	2.5	0.0	-121.23
22	1640	926.15	V	40	74.87	18.5	Max	-29.36	17.4	2.0	0.0	-119.63
22	1640	926.15	V	40	74.87	18.5	Med	-31.01	17.4	2.0	0.0	-121.28
22	1640	926.15	V	40	74.87	18.5	Min	-31.98	17.4	2.0	0.0	-122.25
23	1645	904.15	V	40	74.17	18.5	Max	-30.25	16.7	1.8	0.0	-119.32
23	1645	904.15	V	40	74.17	18.5	Med	-30.84	16.7	1.8	0.0	-119.91
23	1645	904.15	V	40	74.17	18.5	Min	-32.35	16.7	1.8	0.0	-121.42
24	1648	904.15	V	20	74.17	18.5	Max	-32.79	16.7	1.8	0.0	-121.86
24	1648	904.15	V	20	74.17	18.5	Med	-33.48	16.7	1.8	0.0	-122.55
24	1648	904.15	V	20	74.17	18.5	Min	-35.52	16.7	1.8	0.0	-124.59

Table C.5: Measurements between Short North 2 and Jansky Lab, Aug. 2 and 3, 2010 (cont.)

Run #	Time	Freq. (MHz)	Pol.	Tx. Height (ft.)	EIRP (dBm)	Rx. Height (ft.)	Meas. Type	Rx. Power (dBm)	Antenna Gain (dBi)	Cable Loss (dB)	LNA Gain (dB)	Path Loss (dB)
25	1651	926.15	V	20	75.17	18.5	Max	-40.09	17.4	2.0	0.0	-130.66
25	1651	926.15	V	20	75.17	18.5	Med	-43.93	17.4	2.0	0.0	-134.50
25	1651	926.15	V	20	75.17	18.5	Min	-45.14	17.4	2.0	0.0	-135.71
26	1655	1296.91	H	20	75.80	20.75	Max	-33.07	15.8	2.5	0.0	-122.17
26	1655	1296.91	H	20	75.80	20.75	Med	-33.98	15.8	2.5	0.0	-123.08
26	1655	1296.91	H	20	75.80	20.75	Min	-36.18	15.8	2.5	0.0	-125.28
27	906	2303.15	V	10	69.40	20.75	Max	-56.65	14.0	3.5	0.0	-136.55
27	906	2303.15	V	10	69.40	20.75	Min	-62.76	14.0	3.5	0.0	-142.66
28	918	2303.15	V	20	69.40	20.75	Max	-10.01	14.0	3.5	48.2	-138.06
28	918	2303.15	V	20	69.40	20.75	Min	-14.76	14.0	3.5	48.2	-142.81
29	927	2303.15	V	30	69.20	20.75	Max	-9.22	14.0	3.5	48.2	-137.07
29	927	2303.15	V	30	69.20	20.75	Min	-18.21	14.0	3.5	48.2	-146.06
30	945	2303.15	H	30	68.40	20.75	Max	-14.23	14.0	3.5	48.2	-141.28
30	945	2303.15	H	30	68.40	20.75	Min	-27.94	14.0	3.5	48.2	-154.99
31	948	2303.15	H	20	69.40	20.75	Max	-12.30	14.0	3.5	48.2	-140.35
31	948	2303.15	H	20	69.40	20.75	Min	-15.97	14.0	3.5	48.2	-144.02
32	956	2303.15	H	10	68.40	20.75	Max	-18.79	14.0	3.5	48.2	-145.84
32	956	2303.15	H	10	68.40	20.75	Min	-21.63	14.0	3.5	48.2	-148.68

Table C.6: Measurements between Bear Mountain and Jansky Lab, Aug. 3, 2010

	Transmit Site					Jansky Lab Receive Site						
Run #	Time	Freq. (MHz)	Pol.	Tx. Height (ft.)	EIRP (dBm)	Rx. Height (ft.)	Meas. Type	Rx. Power (dBm)	Antenna Gain (dBi)	Cable Loss (dB)	LNA Gain (dB)	Path Loss (dB)
34	1320	904	V	20	75.37	18.5	Max	-26.80	16.70	1.80	50.91	-167.98
34	1320	904	V	20	75.37	18.5	Min	-27.99	16.70	1.80	50.91	-169.17
35	1324	926	V	20	76.57	18.5	Max	-19.97	17.40	2.00	50.85	-162.79
35	1324	926	V	20	76.57	18.5	Min	-20.91	17.40	2.00	50.85	-163.73
36	1330	1297	H	20	76.90	20.75	Max	-28.21	15.80	2.50	50.90	-169.31
36	1330	1297	H	20	76.90	20.75	Min	-29.99	15.80	2.50	50.90	-171.09
37	1354	2303	H	20	70.40	20.75	Max	-36.92	14.00	3.50	48.15	-165.97
37	1354	2303	H	20	70.40	20.75	Min	-37.98	14.00	3.50	48.15	-167.03
38	1409	2303	V	20	69.90	20.75	Max	-41.45	14.00	3.50	48.15	-170.00
38	1409	2303	V	20	69.90	20.75	Min	-43.99	14.00	3.50	48.15	-172.54
39	1428	904	H	20	75.57	18.5	Max	-41.40	16.70	1.80	50.91	-182.78
39	1428	904	H	20	75.57	18.5	Min	-44.24	16.70	1.80	50.91	-185.62
40	1431	926	H	20	76.57	18.5	Max	-29.63	17.40	2.00	50.85	-172.45
40	1431	926	H	20	76.57	18.5	Min	-30.95	17.40	2.00	50.85	-173.77
41	1435	1297	V	20	76.90	20.75	Max	-30.62	15.80	2.50	50.90	-171.72
41	1435	1297	V	20	76.90	20.75	Min	-32.15	15.80	2.50	50.90	-173.25
42	1442	1297	V	30	76.90	20.75	Max	-24.95	14.00	3.50	48.15	-160.50
42	1442	1297	V	30	76.90	20.75	Min	-26.53	14.00	3.50	48.15	-162.08
43	1451	926	H	30	76.57	18.5	Max	-21.64	17.40	2.00	50.85	-164.46
43	1451	926	H	30	76.57	18.5	Min	-22.71	17.40	2.00	50.85	-165.53
44	1454	904	H	30	75.37	18.5	Max	-36.17	16.70	1.80	50.91	-177.35
44	1454	904	H	30	75.37	18.5	Min	-39.13	16.70	1.80	50.91	-180.31
45	1520	904	V	30	75.37	18.5	Max	-22.73	16.70	1.80	50.91	-163.91
45	1520	904	V	30	75.37	18.5	Min	-25.71	16.70	1.80	50.91	-166.89
46	1522	926	V	30	76.57	18.5	Max	-16.61	17.40	2.00	50.85	-159.43
46	1522	926	V	30	76.57	18.5	Min	-18.16	17.40	2.00	50.85	-160.98
47	1527	1297	H	30	76.90	20.75	Max	-34.21	15.80	2.50	50.90	-175.31
47	1527	1297	H	30	76.90	20.75	Min	-36.45	15.80	2.50	50.90	-177.55
48	1537	904	V	20	75.37	18.5	Max	-26.16	16.70	1.80	50.91	-167.34
48	1537	904	V	20	75.37	18.5	Min	-28.33	16.70	1.80	50.91	-169.51

Table C.7: Measurements between Watering Pond North and Jansky Lab, Aug. 4, 2010

	Transmit Site					Jansky Lab Receive Site						
Run #	Time	Freq. (MHz)	Pol.	Tx. Height (ft.)	EIRP (dBm)	Rx. Height (ft.)	Meas. Type	Rx. Power (dBm)	Antenna Gain (dBi)	Cable Loss (dB)	LNA Gain (dB)	Path Loss (dB)
50	1011	904	V	20	75.37	18.5	Max	-10.67	16.70	1.80	50.91	-151.85
50	1011	904	V	20	75.37	18.5	Min	-17.27	16.70	1.80	50.91	-158.45
51	1014	926	V	20	76.57	18.5	Max	-11.15	17.40	2.00	50.85	-153.97
51	1014	926	V	20	76.57	18.5	Min	-14.06	17.40	2.00	50.85	-156.88
52	1018	1297	H	20	76.90	20.75	Max	-12.39	15.80	2.50	50.90	-153.49
52	1018	1297	H	20	76.90	20.75	Min	-16.38	15.80	2.50	50.90	-157.48
53	1025	1297	H	30	76.90	20.75	Max	-11.97	15.80	2.50	50.90	-153.07
53	1025	1297	H	30	76.90	20.75	Min	-18.03	15.80	2.50	50.90	-159.13
54	1030	926	V	30	76.57	18.5	Max	-3.17	17.40	2.00	50.85	-145.99
54	1030	926	V	30	76.57	18.5	Min	-5.96	17.40	2.00	50.85	-148.78
55	1038	904	V	30	75.37	18.5	Max	-7.80	16.70	1.80	50.91	-148.98
55	1038	904	V	30	75.37	18.5	Min	-10.69	16.70	1.80	50.91	-151.87
56	1100	2303	V	20	69.90	20.75	Max	-31.88	14.00	3.50	48.15	-160.43
56	1100	2303	V	20	69.90	20.75	Min	-45.15	14.00	3.50	48.15	-173.70
57	1108	2303	V	30	69.90	20.75	Max	-34.73	14.00	3.50	48.15	-163.28
57	1108	2303	V	30	69.90	20.75	Min	-51.33	14.00	3.50	48.15	-179.88
58	1123	2303	H	30	70.40	20.75	Max	-33.59	14.00	3.50	48.15	-162.64
58	1123	2303	H	30	70.40	20.75	Min	-44.10	14.00	3.50	48.15	-173.15
59	1129	2303	H	20	70.40	20.75	Max	-30.64	14.00	3.50	48.15	-159.69
59	1129	2303	H	20	70.40	20.75	Min	-37.04	14.00	3.50	48.15	-166.09
60	1151	904	H	20	75.37	18.5	Max	-15.58	16.70	1.80	50.91	-156.76
60	1151	904	H	20	75.37	18.5	Min	-18.44	16.70	1.80	50.91	-159.62
61	1155	926	H	20	76.87	18.5	Max	-9.40	17.40	2.00	50.85	-152.52
61	1155	926	H	20	76.87	18.5	Min	-10.73	17.40	2.00	50.85	-153.85
62	1201	1297	V	20	76.50	20.75	Max	-21.84	15.80	2.50	50.90	-162.54
62	1201	1297	V	20	76.50	20.75	Min	-27.04	15.80	2.50	50.90	-167.74
63	1209	1297	V	30	76.50	20.75	Max	-21.62	15.80	2.50	50.90	-162.32
63	1209	1297	V	30	76.50	20.75	Min	-30.12	15.80	2.50	50.90	-170.82

Table C.7: Measurements between Watering Pond North and Jansky Lab, Aug. 4, 2010 (cont.)

Run #	Time	Freq. (MHz)	Pol.	Tx. Height (ft.)	EIRP (dBm)	Rx. Height (ft.)	Meas. Type	Rx. Power (dBm)	Antenna Gain (dBi)	Cable Loss (dB)	LNA Gain (dB)	Path Loss (dB)
64	1217	926	H	30	76.87	18.5	Max	-5.99	17.40	2.00	50.85	-149.11
64	1217	926	H	30	76.87	18.5	Min	-7.18	17.40	2.00	50.85	-150.30
65	1221	904	H	30	75.37	18.5	Max	-11.26	16.70	1.80	50.91	-152.44
65	1221	904	H	30	75.37	18.5	Min	-13.22	16.70	1.80	50.91	-154.40

Table C.8: Measurements between Watering Pond Knob and Jansky Lab, Aug. 4, 2010

			Transmit Site					Jansky Lab Receive Site				
Run #	Time	Freq. (MHz)	Pol.	Tx. Height (ft.)	EIRP (dBm)	Rx. Height (ft.)	Meas. Type	Rx. Power (dBm)	Antenna Gain (dBi)	Cable Loss (dB)	LNA Gain (dB)	Path Loss (dB)
66	1525	904	H	20	75.37	18.5	Max	-10.49	16.70	1.80	50.91	-151.67
66	1525	904	H	20	75.37	18.5	Min	-16.25	16.70	1.80	50.91	-157.43
67	1530	926	H	20	76.87	18.5	Max	-19.61	17.40	2.00	50.85	-162.73
67	1530	926	H	20	76.87	18.5	Min	-44.09	17.40	2.00	50.85	-187.21
68	1537	1297	V	20	76.50	20.75	Max	-15.10	15.80	2.50	50.90	-155.80
68	1537	1297	V	20	76.50	20.75	Min	-27.63	15.80	2.50	50.90	-168.33
69	1555	1297	V	30	76.50	20.75	Max	-14.76	15.80	2.50	50.90	-155.46
69	1555	1297	V	30	76.50	20.75	Min	-23.99	15.80	2.50	50.90	-164.69
70	1603	926	H	30	76.87	18.5	Max	-16.99	17.40	2.00	50.85	-160.11
70	1603	926	H	30	76.87	18.5	Min	-37.18	17.40	2.00	50.85	-180.30
71	1612	904	H	30	75.37	18.5	Max	-10.40	16.70	0.00	0.00	-151.58
71	1612	904	H	30	75.37	18.5	Min	-20.12	16.70	1.80	50.91	-161.30
72	1635	904	V	20	75.37	18.5	Max	-14.21	16.70	0.00	0.00	-155.39
72	1635	904	V	20	75.37	18.5	Min	-27.01	16.70	1.80	50.91	-168.19
73	1642	926	V	20	76.57	18.5	Max	-17.78	17.40	0.00	0.00	-160.60
73	1642	926	V	20	76.57	18.5	Min	-41.59	17.40	2.00	50.85	-184.41
74	1648	1297	H	20	76.90	20.75	Max	-8.28	15.80	0.00	0.00	-149.38
74	1648	1297	H	20	76.90	20.75	Min	-13.39	15.80	2.50	50.90	-154.49
75	1654	1297	H	30	76.90	20.75	Max	-9.68	15.80	0.00	0.00	-150.78
75	1654	1297	H	30	76.90	20.75	Min	-14.34	15.80	2.50	50.90	-155.44
76	1702	926	V	30	76.57	18.5	Max	-25.84	17.40	0.00	0.00	-168.66
76	1702	926	V	30	76.57	18.5	Min	-43.90	17.40	2.00	50.85	-186.72
77	1708	904	V	30	75.37	18.5	Max	-15.30	16.70	0.00	0.00	-156.48
77	1708	904	V	30	75.37	18.5	Min	-23.46	16.70	1.80	50.91	-164.64
78	1713	926	V	30	76.57	18.5	Max	-17.59	17.40	0.00	0.00	-160.41
78	1713	926	V	30	76.57	18.5	Min	-33.80	17.40	2.00	50.85	-176.62
79	1721	1297	V	30	76.90	20.75	Max	-9.22	15.80	0.00	0.00	-150.32
79	1721	1297	V	30	76.90	20.75	Min	-12.67	15.80	2.50	50.90	-153.77
80	1734	2303	H	20	70.40	20.75	Max	-29.30	14.00	0.00	0.00	-158.35
80	1734	2303	H	20	70.40	20.75	Min	-44.33	14.00	3.50	48.15	-173.38
81	1741	2303	H	30	70.40	20.75	Max	-27.30	14.00	0.00	0.00	-156.35

Table C.8: Measurements between Watering Pond Knob and Jansky Lab, Aug. 4, 2010 (cont.)

Run #	Time	Freq. (MHz)	Pol.	Tx. Height (ft.)	EIRP (dBm)	Rx. Height (ft.)	Meas. Type	Rx. Power (dBm)	Antenna Gain (dBi)	Cable Loss (dB)	LNA Gain (dB)	Path Loss (dB)
81	1741	2303	H	30	70.40	20.75	Min	-34.53	14.00	3.50	48.15	-163.58
82	1752	2303	V	30	69.90	20.75	Max	-27.93	14.00	0.00	0.00	-156.48
82	1752	2303	V	30	69.90	20.75	Min	-34.30	14.00	3.50	48.15	-162.85
83	1757	2303	V	20	69.90	20.75	Max	-28.43	14.00	0.00	0.00	-156.98
83	1757	2303	V	20	69.90	20.75	Min	-36.40	14.00	3.50	48.15	-164.95

Appendix D

Foliage Testing and Evaluation

In August 2010, Virginia Tech, NRAO Green Bank, and NSWC conducted a joint radio propagation test at NRAO Green Bank. The last day of testing was devoted to a quickly put together test for the effects of foliage on the propagation loss. The test was conducted by creating by placing the transmitter at a fixed location and moving the receiver location to a series of points with increasing levels of foliage obstruction. The test site, with the transmitter and receiver locations marked, is shown in Figure D.1. The figure was generated with Google Earth using the GPS coordinates of the test locations.

D.1 Experiment Method and Results

The transmitter and receiver were both at fixed heights of 10 ft. above the ground. The ground is mostly flat at the test location. Utilizing Google Earth's distance measuring tools,

Figure D.1: Photo of foliage test location at NRAO Green Bank.

the distances between the transmitter and receiver locations, as well as an estimate of the foliage thickness for each path was measured. Those measurements are provided in Table D.1. The flag number is the receiver location, with 1 being a line-of-site path along the road, and 7 being the most obstructed path. The path length is the distance measured between the transmitter and receiver, while the foliage length is the estimate of the portion of the straight line path that is foliated.

Table D.1: Distances of foliage path measurements.

Rx. Point	Path Length (m)	Foliage Length (m)
1	300.0	0
2	301.1	0
3	303.9	40
4	304.4	88
5	307.5	155
6	309.4	183.5
7	313.6	216

Unlike the other measurements made during the 2010 test, the foliage test data was never properly calibrated. This leads to some challenges in analysis. The lack of calibrated data means that only the relative differences between the receiver locations at any one transmitter frequency have significant meaning. Like the other tests, data was recorded for horizontal and vertical polarizations for 904.15 MHz, 926.15 MHz, 1296.905 MHz, and 2303.15 MHz.

For each polarization, frequency, and receiver location, a maximum and minimum signal value was recorded. From this, a path loss has been generated. Again, it is important to note that this loss number is not properly calibrated. It does not account for the receiving antenna gain or the receiver losses. Actual loss values are probably 3 to 5 dB away from those listed in subsequent tables. The results of the experimental analysis are presented in Tables D.2 and D.3.

Table D.2: H-Pol experimental measurements.

Freq. (MHz)	Rx point	Foliage Length (m)	Min Loss (dB)	Δ to Rx 1 (dB)	Max Loss (dB)	Δ to Rx 1	Variation (dB)	α (Np/m)
	1	0	-85.62	–	-85.62	–	0	
	2	0	-87.35	-1.73	-87.35	-1.73	0	
	3	25	-102.8	-17.18	-102.8	-17.18	0	$1.47x10^{-2}$
904.15	4	100	-114.48	-28.86	-114.48	-28.86	0	$6.18x10^{-3}$
	5	150	-115.64	-30.02	-115.64	-30.02	0	$4.27x10^{-3}$
	6	200	-120.82	-35.2	-120.82	-35.2	0	$3.75x10^{-3}$
	7	235	-125.17	-39.55	-125.17	-39.55	0	$3.57x10^{-3}$
	1	0	-86.29	–	-86.29	–	0	
	2	0	-87.62	-1.33	-87.62	-1.33	0	
	3	25	-106.26	-19.97	-106.26	-19.97	0	$1.71x10^{-2}$
926.15	4	100	-113.33	-27.04	-113.33	-27.04	0	$5.79x10^{-3}$
	5	150	-119.59	-33.3	-119.59	-33.3	0	$4.75x10^{-3}$
	6	200	-121.18	-34.89	-139.01	-52.72	17.83	$3.71x10^{-3}$
	7	235	-128.28	-41.99	-128.28	-41.99	0	$3.79x10^{-3}$
	1	0	-84.55	–	-84.55	–	0	
	2	0	-86.56	-2.01	-86.93	-2.38	0.37	
	3	25	-106.61	-22.06	-106.61	-22.06	0	$1.90x10^{-2}$
1296.905	4	100	-118.9	-34.35	-138.2	-53.65	19.3	$7.38x10^{-3}$
	5	150	-117.95	-33.4	-125.1	-40.55	7.15	$4.76x10^{-3}$
	6	200	-123.49	-38.94	-134.68	-50.13	11.19	$4.15x10^{-3}$
	7	235	-126.87	-42.32	-136.51	-51.96	9.64	$3.82x10^{-3}$
	1	0	-93.68	–	-93.68	–	0	
	2	0	-91.64	2.04	-91.64	2.04	0	
	3	25	-110.43	-16.75	-110.43	-16.75	0	$1.43x10^{-2}$
2303.15	4	100	-119.06	-25.38	-119.06	-25.38	0	$5.43x10^{-3}$
	5	150	-127.88	-34.2	-127.88	-34.2	0	$4.88x10^{-3}$
	6	200	-127.2	-33.52	-154.46	-60.78	27.26	$3.56x10^{-3}$
	7	235	-132.56	-38.88	-158	-64.32	25.44	$3.51x10^{-3}$

Table D.3: V-Pol experimental measurements.

Freq. (MHz)	Rx point	Foliage Length (m)	Min Loss (dB)	Δ to Rx 1 (dB)	Max Loss (dB)	Δ to Rx 1	Variation (dB)	α (Np/m)
	1	0	-86.57	–	-86.57	–	0	
	2	0	-88.73	-2.16	-88.73	-2.16	0	
	3	25	-105.17	-18.6	-105.17	-18.6	0	$1.60x10^{-2}$
904.15	4	100	-117.57	-31	-126.24	-39.67	8.67	$6.65x10^{-3}$
	5	150	-115.69	-29.12	-115.69	-29.12	0	$4.14x10^{-3}$
	6	200	-113.96	-27.39	-123.58	-37.01	9.62	$2.90x10^{-3}$
	7	235	-123.72	-37.15	-123.72	-37.15	0	$3.35x10^{-3}$
	1	0	-88.58	–	-88.58		0	–
	2	0	-89.21	-0.63	-89.21	-0.63	0	
	3	25	-105.4	-16.82	-105.4	-16.82	0	$1.44x10^{-2}$
926.15	4	100	-112.54	-23.96	-116.15	-27.57	3.61	$5.12x10^{-3}$
	5	150	-118.12	-29.54	-130.44	-41.86	12.32	$4.20x10^{-3}$
	6	200	-119.65	-31.07	-135.21	-46.63	15.56	$3.30x10^{-3}$
	7	235	-118.27	-29.69	-131.75	-43.17	13.48	$2.66x10^{-3}$
	1	0	-88.22	–	-88.22	–	0	
	2	0	-87.9	0.32	-87.9	0.32	0	
	3	25	-111.97	-23.75	-115.62	-27.4	3.65	$2.04x10^{-2}$
1296.905	4	100	-112.48	-24.26	-118.33	-30.11	5.85	$5.19x10^{-3}$
	5	150	-114.84	-26.62	-123.23	-35.01	8.39	$3.78x10^{-3}$
	6	200	-115.76	-27.54	-121.52	-33.3	5.76	$2.92x10^{-3}$
	7	235	-120.46	-32.24	-136.03	-47.81	15.57	$2.89x10^{-3}$
	1	0	-94.52	–	-94.52	–	0	
	2	0	-92.08	2.44	-92.08	2.44	0	
	3	25	-107.06	-12.54	-107.06	-12.54	0	$1.07x10^{-2}$
2303.15	4	100	-124.76	-30.24	-141.43	-46.91	16.67	$6.48x10^{-3}$
	5	150	-123.02	-28.5	-132.99	-38.47	9.97	$4.05x10^{-3}$
	6	200	-127.4	-32.88	-148.48	-53.96	21.08	$3.50x10^{-3}$
	7	235	-126.32	-31.8	-147.9	-53.38	21.58	$2.85x10^{-3}$

Horizontal polarization results are in Table D.2, and vertical polarization results are in Table D.3. The flag number and foliage length have the same meaning as in Table D.1. The minimum loss and maximum loss are the measured minimum and maximum terrain loss in dB, while the "Δ to flag 1" column lists the difference in dB between the loss at that receiver location and the loss at the line-of-site location number one. The variation column lists the difference, in dB, between the maximum and minimum measurements. The final column shows a simplistic estimate of the loss factor due to the foliage.

The loss factor is defined such that the power loss due to the foliage is given by the exponential form below, where d is the foliage depth.

$$L_{fol} = e^{-2\alpha d}$$

The simple estimate of the loss factor is computed by first removing the effects of the free space loss from the D measurements, then dividing by the foliage distance and converting from dB/m to Np/m.

$$\alpha = -\Delta \left(\frac{\log_{10} e}{20d} \right)$$

As previously stated, this is a simplistic estimate, since it does not account for reflections from the initial foliage interface, the geometry of the situation, or the diffraction around the foliage edge. A more detailed model is necessary to account for that large variety of effects.

Such a model is presented below along with its results.

D.2   UTD Model for the Foliage Experiment

To account for those factors mentioned above, a more complete model was needed. Radiation transport theory is often used to model foliage. However, here, since the measurements were performed near ground level, and the foliage penetration was primarily occurring through the trunks of the trees, it was decided to develop a simple geometric optics (GO) and uniform theory of diffraction (UTD) model of the experiment and see if it could be used to generate estimates of an effective material that could replace the foliage. The UTD/GO model consists of a dielectric ground plane and a dielectric foliage wedge, as illustrated below in Figure D.2. The transmitter and receivers were located as in the experiment. In the model, the foliage extends up to infinite height, and the ground plane extends out to infinite distances.

The diffraction coefficients used were those for penetrable wedges, as developed by Bernardi, et. al [129]. The model used the antenna patterns as furnished by NRAO prior to the 2009 experiments, and for each case assumed that the transmitter and receiver antennas were pointed directly at each other. Furthermore, the model account was limited to rays interacting with no more than two surfaces. This means that nine ray paths were considered for each receiver point. The paths are:
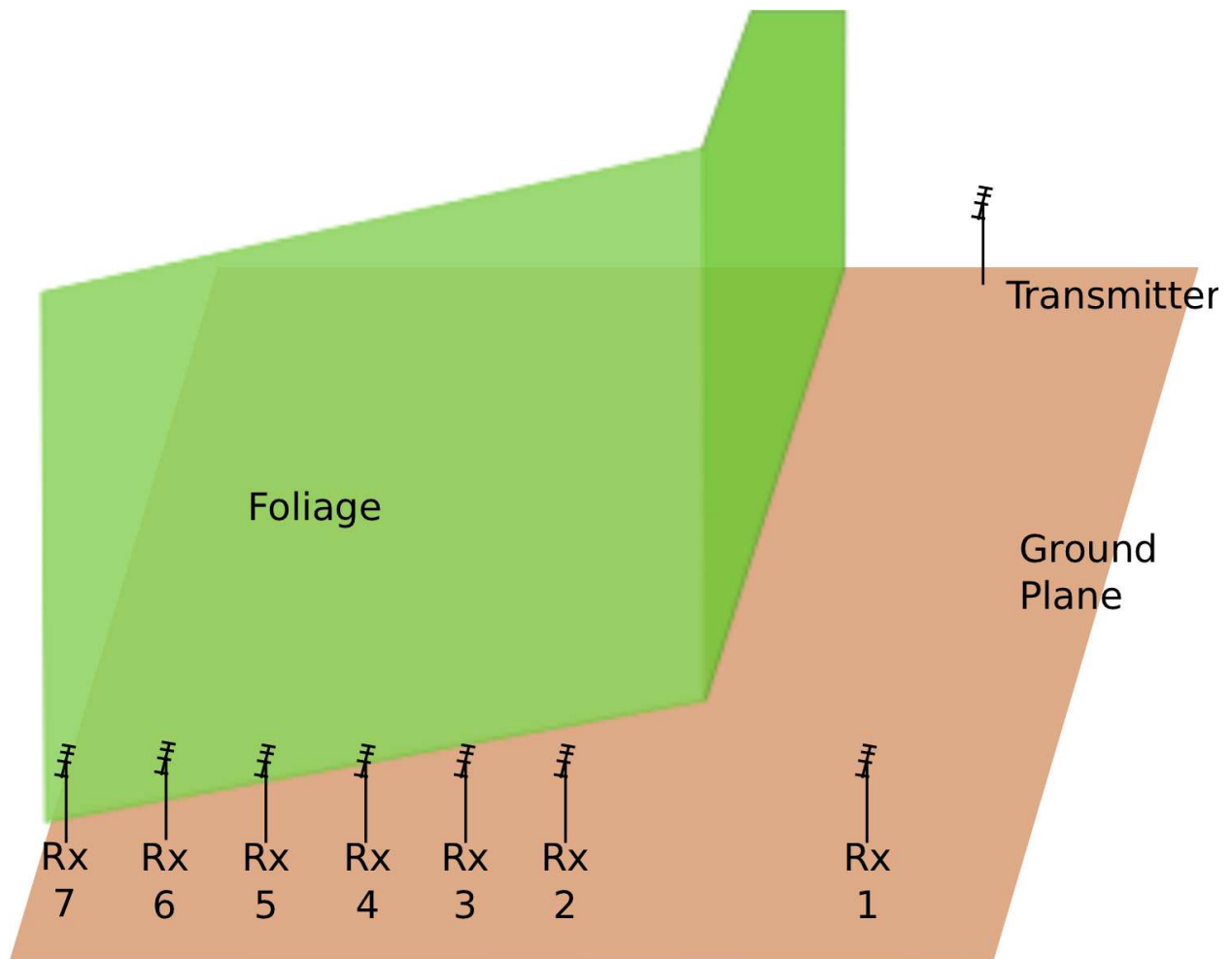
- Direct path

Figure D.2: Setup of UTD/GO model.

- Single ground reflection

- Single reflection off the foliage

- Single diffraction off the foliage corner

- Single diffraction off the foliage/ground corner

- Double reflection from ground then foliage

- Double reflection from foliage then ground

- Penetration through the foliage (refraction through 2 foliage/air interfaces)

- Reflection from the ground and diffraction from the foliage corner

Lastly, the ground has an assumed relative dielectric constant of 5. This was not altered during the process of finding the foliage parameters, though it can easily be altered in the model.

D.2.1   UTD model results

For each frequency, the UTD model was exercised for a range of dielectric permittivities (er) and conductivities (s) for the foliage. Each run was compared to the experimental measurements for that frequency and the search was narrowed to focus around areas with the best fit. This process was repeated until the best fit was found for a three significant figure result.

Table D.4 provides the best fit as compared to the minimum loss results presented in Tables D.2 and D.3. Table D.5 shows the results for the maximum loss. The RMS error column shows the root mean square error between the UTD/GO model with the given parameters and the experimental results. Thus, the parameters shown are those which minimized the RMS error. The fit is significantly better for horizontal polarization than for vertical polarization, as seen in the error term. It is also significantly better for the minimum loss than the maximum loss.

Table D.4: UTD model best fit to experimental minimum loss.

Freq.	H-Pol		V-Pol	
(MHz)	ϵ_r	RMS Error (dB)	ϵ_r	RMS Error (dB)
904	1.013 - j 0.0030	1.54	0.967 - j 0.0015	2.53
926	1.0032 -j 0.0029	1.62	0.967 - j 0.0015	2.18
1296	1.0004 - j 0.0030	1.42	0.967 - j 0.00091	2.90
2303	1.0005 - j 0.0021	2.22	0.987 - j 0.00059	3.37

Table D.5: UTD model best fit to experimental maximum loss.

Freq.	H-Pol		V-Pol	
(MHz)	ϵ_r	RMS Error (dB)	ϵ_r	RMS Error (dB)
904	1.013 - j 0.0030	1.54	0.967 - j 0.0015	2.53
926	1.0014 - j 0.0022	2.26	1.001 - j 0.0026	3.53
1296	1.0052 - j 0.0028	3.54	0.974 - j 0.0014	3.96
2303	1.0004 - j 0.0013	6.71	1.013 - j 0.0087	6.12

This is sensible since the maximum loss is caused mainly by multipath in the foliage, and there is no mechanism in the model to account for this type of scattering. For the most part, the model suggests that the real part of the relative dielectric constant should be close to 1.0 for simulating foliage, with relatively little refractive effect, and suggests that the foliage primarily acts as a conductive (lossy) version of free space.

D.3   Layered MOMI and Results

After obtaining the UTD fit to the measured data, MOMI, as applied to dielectrics, was adapted to run on layered media. The MOMI model was then run with a foliage layer over the ground layer. The foliage layer used a dielectric constant that matched the values obtained in the previous section.

Incorporation of a foliage layer requires the use of MOMI for penetrable dielectrics. The adaptation of MOMI for penetrable dielectrics is described by both Iodice and Westin [113, 130]. Additionally, when multiple layers are present, the interactions must be appropriately ordered. For this work, the solution was ordered by the x-position of the center of each patch, either increasing x, for $(D-L)^{-1}$, or decreasing x, for $(D-U)^{-1}$ operations. Figure D.3 shows this ordered for a foliage layer. Additionally, because MOMI does not work well on closed bodies, the layer is left open, extending above the entire length of the surface, though made very thin (40 cm) where foliage is not present.
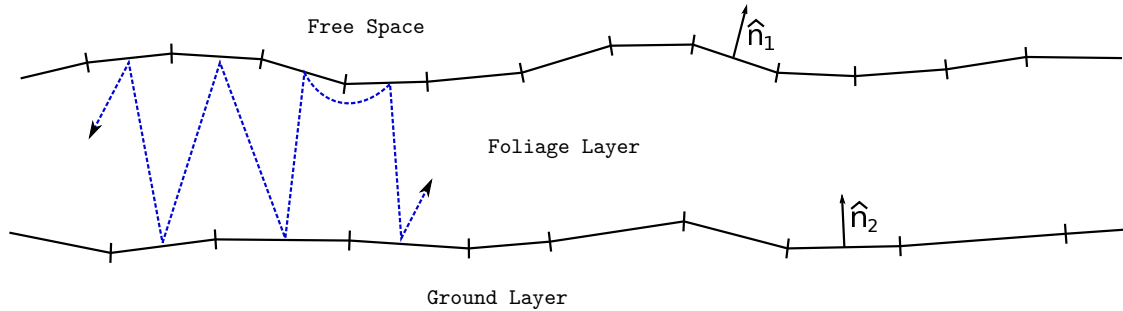

Figure D.3: Solution ordering of layered MOMI

Testing of the foliage layer was performed on the Jack Ball and Short North 2 paths. Approximate locations for the foliage were determined from the overhead photography, while

the height of the foliage was estimated at 60 feet. Figure D.4 shows the two paths with the assumed foliage layer over the ground.

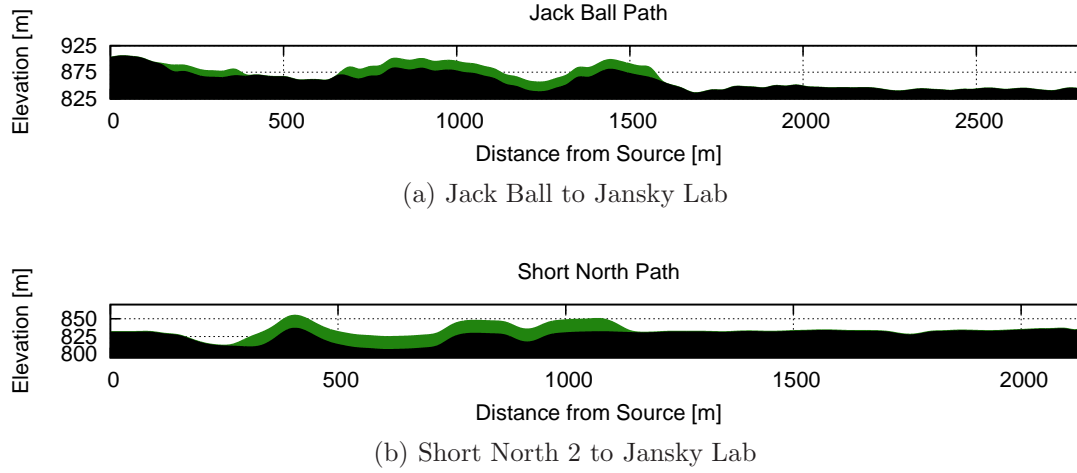(a) Jack Ball to Jansky Lab

(b) Short North 2 to Jansky Lab

Figure D.4: Paths with foliage layer

Results of the layered MOMI computations are presented in Tables D.6 to D.9. All tables present the difference between the randomly rough PEC mean and measurements, as reported in chapter 8, in the "Randomly Rough PEC" columns. Also presented is the difference between a single smooth dielectric with the foliage layer and the experimental measurements, in the "Smooth Foliated Dielectric" columns. All results are presented in dB, and summaries of the bias (mean) and error (RMS error) are provided for each polarization and method for each path.

Two cases are presented for the Jack Ball transmitter, beginning with Table D.6. This table compares the measurements along the Jack Ball to Jansky Lab path, which contained a foliated ridge, with the bare PEC and foliated dielectric MOMI results. In this case, the dielectric foliage layer vastly overcompensates for the real foliage attenuation. Adding the

Table D.6: Foliage layer MOMI results for Jack Ball to Jansky Lab compared to measurements. Δ values in dB.

Freq.	Tx Height	Randomly Rough PEC		Smooth Foliated Dielectric	
(MHz)	(ft)	H-Pol Δ	V-Pol Δ	H-Pol Δ	V-Pol Δ
904	20	4.87	9.85	-5.87	-7.38
904	30	4.34	9.11	-4.80	-7.49
926	20	3.86	12.61	-17.23	-11.13
926	30	3.68	8.76	-27.37	-30.32
1296	20	12.38	13.72	-13.99	-15.55
1296	30	11.33	12.32	-6.65	-6.77
2303	20	12.87	10.73	-11.23	-16.57
2303	30	11.73	7.59	-14.61	-17.75
Mean Error		8.13	10.59	-12.72	-14.12
RMS Error		9.05	10.77	14.50	15.93

foliage layer increased the loss much more than by the original error amount. However, as

will be seen, this was the worst case performance for the foliage layer.

Table D.7: Foliage layer MOMI results for Jack Ball to Water Tower compared to measurements. Δ values in dB.

Freq.	Tx Height	Randomly Rough PEC		Smooth Foliated Dielectric	
(MHz)	(ft)	H-Pol Δ	V-Pol Δ	H-Pol Δ	V-Pol Δ
904	10	-3.84	0.46	2.71	4.38
904	20	2.82	-0.47	2.37	0.59
904	30	3.21	-1.77	2.13	2.17
926	10	-2.30	-2.57	3.49	4.00
926	20	-0.99	0.77	4.08	4.21
926	30	1.74	0.92	1.97	0.45
1296	10	6.68	5.31	4.28	2.80
1296	20	-1.94	1.50	0.48	0.70
1296	30	1.09	0.95	0.58	0.74
2303	10	-0.53	-2.76	2.01	-0.61
2303	20	-1.79	0.31	1.48	0.48
2303	30	2.59	2.35	-0.25	-0.64
Mean Error		0.56	0.42	2.11	1.61
RMS Error		2.92	2.16	2.51	2.38

Table D.7 shows the comparison of the results for the line-of-sight Jack Ball to Water

Tower path. In this case, the addition of the foliage layer does not add any additional

obstruction, and merely changes the effects of any ground reflections. The result is a slight

increase in the bias, with minimal change to the overall error.

The Short North 2 to Jansky Lab path is the last case for which the foliage method was tested. Results are shown in Table D.8. For this path, the foliage produces a significant increase in the height of the obstructing hill, going from a path which grazes the top of the foliage to one in which the foliage provides an opaque obstruction. Here, for the problem that the foliage layer was designed to solve, the error is drastically reduced and the results fall more in line with the other levels of error.

Finally, Table D.9 provides the overall levels of error when considering all three of the above paths. In this case, the bias and error are drastically reduced, by the addition of the foliage layer, with the improvement in the worst case Short North 2 path offsetting the reduced accuracy in the better Jack Ball cases. However, the foliage method is slow to compute, and applying it to the longer paths is not presently feasible. Additionally, the added complexity makes parallelizing the software in that case more difficult to accomplish.

Table D.8: Foliage layer MOMI results for Short North 2 to Jansky Lab compared to measurements. Δ values in dB.

Freq. (MHz)	Tx Height (ft)	Randomly Rough PEC		Smooth Foliated Dielectric	
		H-Pol Δ	V-Pol Δ	H-Pol Δ	V-Pol Δ
904	10	20.02	30.54	9.92	22.14
904	20	16.55	22.67	4.68	10.33
904	30	20.32	24.97	4.42	10.66
904	40	N/A	23.23	N/A	6.11
926	10	22.22	27.17	-7.50	2.44
926	20	20.05	29.32	-8.39	1.04
926	30	25.05	28.87	2.41	7.70
926	40	N/A	23.55	N/A	3.86
1296	10	16.17	17.95	-6.21	-5.54
1296	20	17.39	20.58	-6.11	-2.33
1296	30	19.35	26.62	-3.97	2.46
1296	40	17.18	N/A	-0.43	N/A
2303	10	31.99	21.69	5.53	-4.34
2303	20	31.03	28.08	1.44	-1.11
2303	30	36.50	32.24	5.37	-0.44
Mean Error		22.60	25.53	0.09	3.78
RMS Error		23.47	25.84	5.72	7.98

Table D.9: Foliage layer MOMI results for all three paths compared to measurements. Δ values in dB.

	Randomly Rough PEC		Smooth Foliated Dielectric	
	H-Pol Δ	V-Pol Δ	H-Pol Δ	V-Pol Δ
Mean Error	14.01	16.18	1.05	2.96
RMS Error	18.22	20.30	4.54	6.22